The physical and magnetic properties of electrodeposited iron foil

Ian Bruce MacCormack

THE PHYSICAL AND MAGNETIC PROPERTIES OF ELECTRODEPOSITED IRON FOIL

by

IAN BRUCE MacCORMACK B.Sc.

A thesis submitted to the University of Durham in candidature for the degree of Master of Science.

March 1979

ABSTRACT

This work is concerned predominantly with the properties of iron foil produced by an industrial process of electrodeposition. The structural, mechanical, electrical and magnetic characteristics of the foil have been investigated but are found to compare very poorly with those of commercial soft magnetic sheet materials. Some improvement in the foil magnetic properties can be effected by high temperature heat treatments, and a strain-anneal technique for producing a large grain structure has been developed. The physical as well as magnetic properties of the heat treated foil have been investigated, and magnetic domain structures on the large grained foil have been studied using both wet and dry colloid techniques. In the heat treated state the foil has shown some potential value as a magnetic shielding material and comparisons with commercial mumetal shields have been made.

In work conducted at the Synchrotron Radiation Facility at Daresbury Laboratory the value of synchrotron radiation as a tool for the rapid assessment of the grain size, orientation and perfection of a polycrystalline metal sheet material has been demonstrated and the recrystallization of silicon-iron at 1000^{o}C has been studied. The latter experiment represents the first in-situ X-ray topographic study of crystal growth under normal growth conditions.

ACKNOWLEDGEMENTS

Thanks are due to the following:

Professor A.W. Wolfendale and Professor B.H. Bransden for the use of the facilities of the Physics Department.

Dr W.D. Corner and Dr. B.K. Tanner for help and guidance throughout the project.

Members of the Solid State Research Group, in particular Mr R.L. Smith, for assistance and ideas, and Mr K.G. Moulson for technical advice.

The Science Research Council for financial support during the project and for permitting access to the Synchrotron Radiation Facility at Daresbury Laboratory.

Hall and Pickles Limited for co-operating with a CASE award and for supplying the electrodeposited iron foil studied in the project.

Miss E.V. Gathercole, Harrogate, for typing the text.

CONTENTS

CHAPTER ONE

SOFT MAGNETIC MATERIALS

1.1 Introduction

The importance of the major portion of soft magnetic materials used in the world today relates to the production and use of electrical power. Within this field soft magnetic materials find a great diversity of applications, the most common being their use in rotors of generators and motors and in transformer laminations. The term "soft" came into general use around the turn of the century, when it was observed that the more easily magnetized materials were physically softer than permanent magnet or "hard" materials.

This work is concerned with a study of the physical and magnetic properties of iron foil produced by electrodeposition and of its possible use as a soft magnetic material.

1.2 Ferromagnetism

A ferromagnetic material is one which exhibits a magnetic moment even in the absence of an applied magnetic field; this spontaneous magnetization is the result of the tendency of the strongly coupled atomic dipole moments to be aligned parallel. Above a transition temperature, known as the ferromagnetic Curie temperature (T_c) the spontaneous magnetization disappears. Below T_c, under certain conditions, a ferromagnetic material may exhibit no net magnetic moment under zero applied field, though the application of a small field results in a large magnetization. This phenomenon can be

explained by the existence of domains, postulated by Weiss (1907), which are small regions of the ferromagnetic material, each spontaneously magnetized but not necessarily in the same direction. Certain domain configurations can lead to a net magnetic moment of zero over the whole body of the ferromagnet. The importance of domains in explaining the magnetization process of a ferromagnet will be dealt with in a later section.

The majority of ferromagnetic materials are metals or alloys; of particular relevance to this work are the metals iron, cobalt, and nickel, their alloys with one another and with other elements.

It is not proposed to discuss the theory of the existence of the spontaneous magnetization of a ferromagnetic material; this is covered in many works, including Morrish (1965).

1.3 Essential Parameters

1.3.1 Magnetization Curve and Hysteresis Loop

The principal bulk property of a ferromagnetic material is the existence of a large magnetization per unit volume (M) with the application of a small magnetic field (H). It is also found that the M-H magnetization curve displays an irreversibility or hysteresis. Similar effects are observed in the B-H magnetization curve, where B is the magnetic induction or flux density defined as

$$B = H + 4\pi M \qquad (1.1)$$

In the c.g.s electromagnetic units to be used here, B is measured in gauss (G), H in oersteds (Oe) and M in erg Oe^{-1} cm^{-3}. It should be noted that the values of B and M for a bulk specimen are not the same as those in the finer units of structure called domains, the

former being an average over the latter.

Figure 1.1 shows a typical B-H magnetization curve and hysteresis loop for a ferromagnetic polycrystalline material. The reference state for the magnetization curve is the demagnetized state (0) for which B = 0 when H = 0. If a field H is now applied to the sample, the induction B increases until a saturation value B_s is reached. By performing a cycle of operations consisting of decreasing the field to zero, increasing it in the reverse direction, reducing it again to zero and then increasing it in the original direction, a hysteresis loop is obtained. The important numerical parameters of the loop are the residual or remanent induction (B_r) when the field is reduced to zero, the coercive force (H_c) which is the field required to reduce the induction to zero and the area of the loop, which is a measure of the energy expended in taking the sample through the magnetization cycle. This energy expenditure is known as the hysteresis loss. The ratio B/H is known as the relative permeability (μ) where

$$\mu = 1 + 4\pi K \qquad (1.2)$$

K is the susceptibility per unit volume given by the ratio M/H and is measured in erg Oe^{-2} cm^{-3}. Because the ratio B/H varies with applied field, several permeabilities can be defined for the magnetization curve, the most important being the initial permeability (μ_o) corresponding to the slope of the line Ox in figure 1.1 and the maximum permeability (μ_{max}) corresponding to the slope of Oy. If the maximum field in the cycle of operations producing a hysteresis loop is insufficient to saturate the sample, a minor hysteresis loop is obtained. A series of such loops for increasing maximum field is shown in figure 1.2. The tips of the loops in the first quadrant

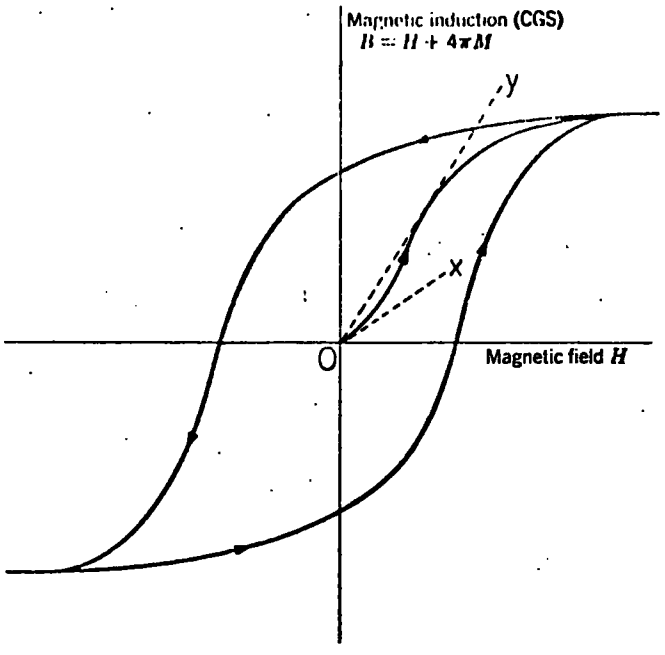

Figure 1.1 Typical magnetization curve and hysteresis loop for a ferromagnetic material

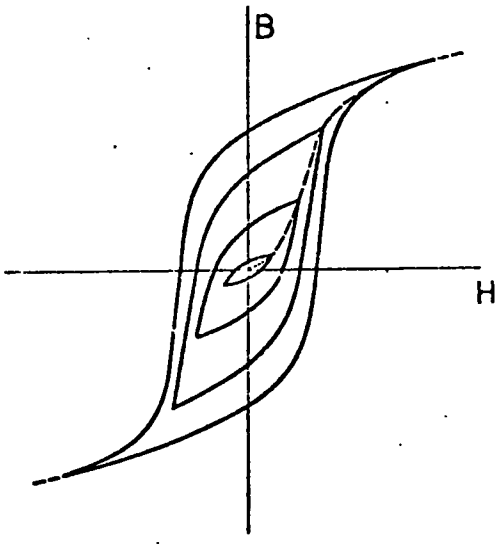

Figure 1.2 Major and three minor hysteresis loops for a typical ferromagnetic material (after Morrish, 1965).

describe the magnetization curve of the sample.

Two important effects associated with ferromagnetic materials will be mentioned briefly here.

1.3.2 Magnetocrystalline Anisotropy

It is found that the magnetization curves for single crystals of ferromagnetic materials generally show pronounced anisotropic properties. Much smaller fields are required to magnetize to saturation along certain directions than along others. The crystallographic axes along which the magnetization tends to lie are called easy directions; those along which it is most difficult to produce saturation are known as hard directions. In iron, which has a body centred cubic structure at room temperature. the $\langle 100 \rangle$ crystallographic directions or cube edges are easy. The magneto-crystalline anisotropy energy F_k is the energy required to make the magnetization lie along a certain direction compared to an easy direction. F_k can be specified in terms of anisotropy constants K_i and the angles between the magnetization and the crystallographic axes.

1.3.3 Magnetostriction

Joule in 1842 first observed the phenomenon of magnetostriction, the property of a ferromagnetic material to change its dimensions upon application of a magnetic field. Hence there is an interaction between magnetization and strain. The linear magnetostriction (λ) is defined as the change of length per unit length measured in a particular direction. It is apparent that this effect can lead to stress in a ferromagnetic material, particularly a polycrystalline

one in which the individual grains impose constraints upon one another.

1.4 Magnetic Domains

As mentioned in section 1.2 elementary theory predicts that a ferromagnetic material below its Curie temperature should always exhibit a spontaneous magnetization irrespective of the applied field. The observation that this need not be so in practice was explained by Weiss by the existence of small regions of material called domains. Each domain is spontaneously magnetized, but in a bulk material domains of opposite magnetization can lead to a net demagnetized state. In 1932 Bitter obtained visual evidence for domains.

The existence of domains can be explained in terms of energy considerations by reference to the idealized representation of figure 1.3. In the absence of domains, the magnetostatic energy due to the free magnetic poles is large. By splitting into domains the magnetostatic energy can be considerably reduced. However in the region of the boundary between adjacent domains, known as the domain wall, the elementary magnetic moments are no longer parallel and in their preferred directions, so that an energy can be ascribed to the boundary. The more boundaries which are present the greater the total boundary energy. Hence the equilibrium domain configuration is decided by the competition between the decrease in the magnetostatic energy and the increase in the domain wall energy.

1.5 The Magnetization Process

A full discussion of the magnetization process requires consideration of inhomogeneities in the crystal and stray demagnetizing fields in the material. We shall limit the discussion here to a few qualitative

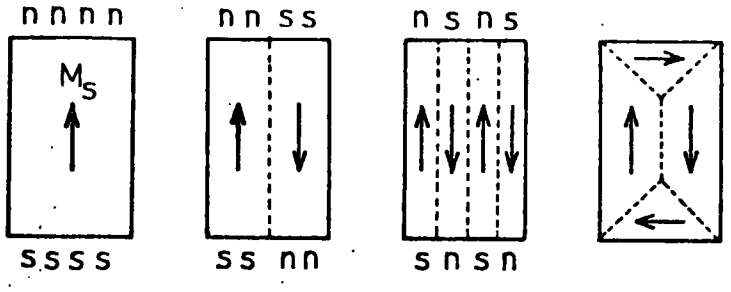

Figure 1.3 Hypothetical domain configurations in a bulk ferromagnet

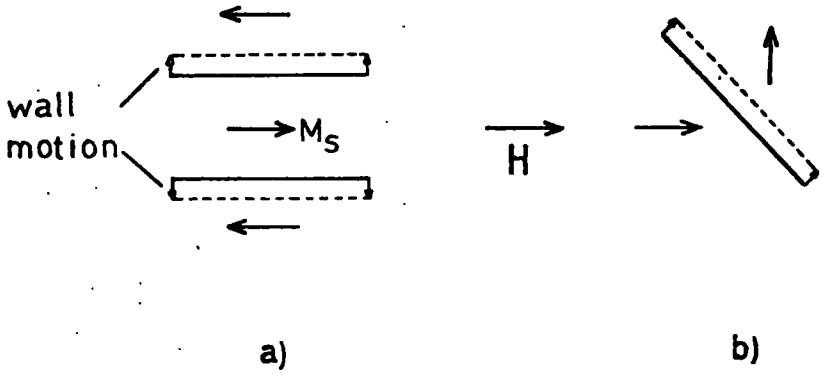

Figure 1.4 Motion of a) 180° and b) 90° domain walls under the influence of a magnetic field H.

features.

In the demagnetized state we consider a ferromagnetic material as consisting of domains of saturated magnetization (M_s) lying along preferred crystallographic directions with the net magnetization of the sample over all the domains vanishing. The application of a magnetic field causes a force to be exerted on the domain walls which move so that those domains whose directions of magnetization are oriented favourably with respect to the applied field grow at the expense of those which are not. The field does not appreciably affect the magnetization within the domains. Figure 1.4 illustrates schematically the direction of motion of 180° and 90° domain walls under the influence of a field. The distribution of defects and imperfections within a sample leads to a variation in the potential energy of each wall which is schematically represented in figure 1.5. As long as each wall remains within a potential trough its movement is reversible. This corresponds to the initial shallow gradient portion of the magnetization curve. The application of a larger field causes walls to be pushed over potential peaks and their motion is no longer reversible upon removal of the field. For a sufficiently large field most of the walls will have been swept out of the material and domains whose magnetization directions are most nearly parallel to the field occupy most of the volume of the material. This process is complete by the knee of the magnetization curve. At this stage the sample is not saturated in the field direction because the magnetization in each crystal is lying along the easy direction most nearly parallel to the field. To completely saturate the sample in the field direction the magnetization in the crystals must be rotated into the field direction. Because of the magnetocrystalline

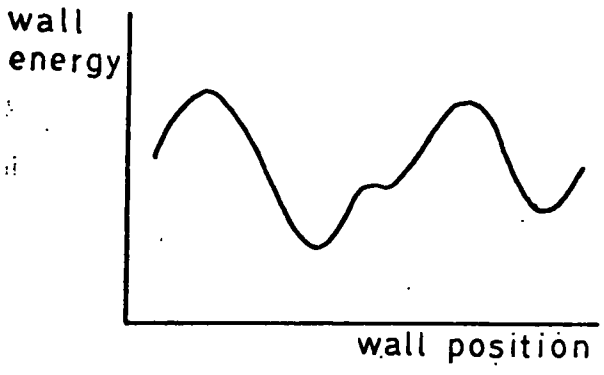

Figure 1.5 Variation of domain wall energy with position.

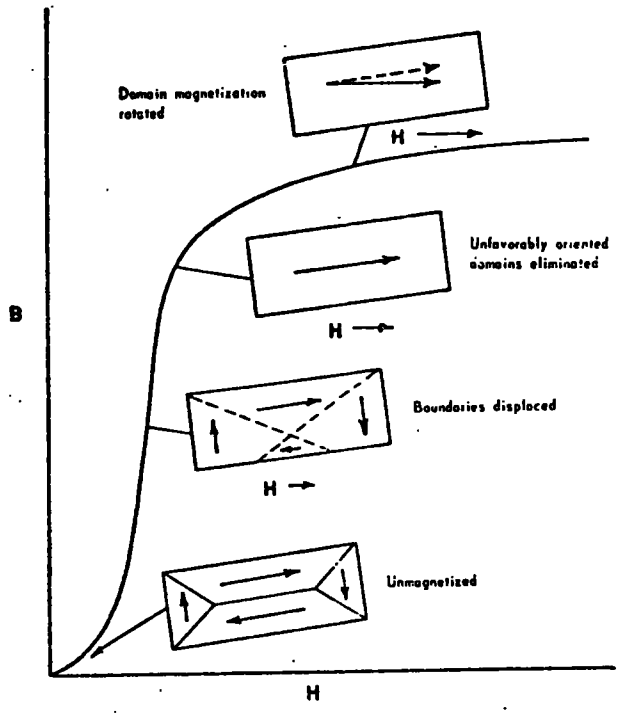

Figure 1.6 Changes in domain structure during magnetization (after Littmann, 1971).

anisotropy energy this requires a large field. Magnetization rotation is clearly a reversible process and corresponds to the flatter portion of the magnetization curve beyond the knee. The whole process is illustrated schematically in figure 1.6.

1.6 Soft Magnetic Materials

1.6.1 Introduction

The distinction between soft and hard magnetic materials is largely arbitrary and is based primarily on the technical application to which a material is to be put. Properties which are usually required in a soft magnetic material include a large saturation magnetization or induction, small coercive force and remanence, large initial and maximum permeabilities and small hysteresis loss. A coercive force of less than 2 Oe is generally considered a requirement for a material to be classified as magnetically soft. A large saturation magnetization is achieved by choosing a metal or alloy with a large atomic magnetic moment. The other properties are improved by increasing the freedom of movement of the domain walls. Inclusions, cavities, grain boundaries and internal stresses all impede the mobility of the domain walls and their effects must be minimized in order to achieve good soft magnetic characteristics. A low impurity concentration is necessary to reduce the effect of inclusions, whilst stresses of a mechanical origin can be relieved by annealing. The effect of inclusions on wall motion is also reduced by choosing a material of low anisotropy constant, whilst stress effects are minimized if the magnetostriction is small. The subject of soft magnetic materials is reviewed by Lee and Lynch (1959).

It should be noted that as soft magnetic materials are frequently employed under conditions of alternating magnetization, their electrical properties also assume considerable importance; eddy currents are drastically reduced by choosing an alloy with a large electrical resistivity. Indeed Littmann (1971) gives the eddy current loss (P_e) in sheets of ferromagnetic material, on the assumption of uniform flux density throughout the thickness as

$$P_e \propto \frac{\pi^2 t^2 B^2 f^2}{\rho} \qquad (1.3)$$

measured in erg cm^{-3} s^{-1}, where B is the maximum induction, t the thickness, f the frequency and ρ the volume resistivity. A large magnetostriction is a particularly great problem in alternating current applications because it contributes to noise in transformers.

1.6.2 Preparation of Soft Magnetic Materials

A few general methods of manufacturing soft magnetic materials will be mentioned briefly at this point.

Metallic materials are normally made by melting and casting. In the molten state the metal must be protected from oxidation; this may be achieved either by melting in a vacuum or inert atmosphere or by covering the melt with a flux. The second alternative suffers from the disadvantage that it may lead to the introduction of impurities into the melt. This problem and that of preferential evaporation and segregation during solidification limit the precision of composition of the alloy.

Several metals may be alloyed using a technique known as powder metallurgy in which powders of the separate constituents are mixed,

pressed into a block and sintered at a temperature of about 1300°C. The metals then alloy by diffusion but without melting. Iron, nickel, cobalt, copper and molybdenum but not aluminium may be alloyed in this way. Problems of oxidation, contamination and composition imprecision are eliminated by this technique.

Thin films of certain soft magnetic materials, in the thickness range 30-10,000 Å can be prepared by deposition from the vapour phase onto a heated base plate at about 300°C in the presence of a magnetic field. Films produced in this way exhibit certain interesting properties which will be mentioned in a later section.

1.6.3 Improvement of Soft Magnetic Qualities

Several techniques exist for the improvement of the properties of a soft magnetic material once it has been shaped as required.

Annealing or heating for a time, often only a few minutes, in an inert atmosphere causes recrystallization of the worked material and relieves the stress introduced during the shaping process. More prolonged annealing sometimes further improves the properties by removing certain impurities such as carbon and nitrogen. Coercive force can usually be considerably reduced by annealing.

In some polycrystalline materials properties similar to those of a single crystal can be achieved by systematically aligning the axes of the individual grains; this process is known as grain orientation. A deformation texture is introduced by heavy cold working, usually rolling, and subsequent recrystallization produces a grain-oriented state. This subject will be treated more fully in Chapter 3. For

fields applied parallel to the rolling direction the hysteresis loop is found to be roughly rectangular, increasing the maximum permeability and reducing the coercive force and hysteresis loss.

A similar effect can be achieved for some alloys by magnetic annealing, that is applying a magnetic field to the material as it cools through a certain temperature range.

1.6.4 Common Soft Magnetic Materials

In this section a few of the more common soft magnetic materials will be mentioned and compared.

Iron:

Because of its abundance and excellent magnetic properties iron was the first soft magnetic material to be exploited. Commercially pure iron is melted under conditions which remove carbon and manganese but leave the metal in a highly oxidised condition. The oxide inclusions are large however and do not appreciably affect magnetic properties. Iron has a large saturation induction of 21,500 G and commercially pure iron has a coercive force of about 0.9 Oe which is not particularly small compared with other soft materials. Reduction of this figure by purification is prohibitively expensive and the low electrical resistivity of 10 $\mu\Omega$ cm restricts the use of iron to D.C. applications where eddy current losses are not present. Iron, however, remains an important soft magnetic material.

If commercial grade iron is not good enough for an application, an alloy is usually used instead. Iron is most commonly alloyed with

silicon, nickel or cobalt, depending on the required properties. Aluminium has a similar effect to silicon but is more expensive and consequently finds little commercial application in this field.

Silicon-Iron Alloys:

Alloys of silicon with iron have been widespread since 1900. The addition of silicon to iron does not greatly reduce the saturation induction, but does dramatically reduce the anisotropy and magnetostriction and also increases the electrical resistivity sufficiently for A.C. applications to become feasible. Figure 1.7 shows the variation of the important properties of silicon-iron alloys with composition. The presence of silicon also apparently makes it easier to reduce the effect of inclusions and to increase the grain size by metallurgical treatment, both of which improve the soft magnetic characteristics. A limit of about 6% silicon is imposed by the decrease in ductility of the alloy which makes it increasingly difficult to roll.

Very frequently silicon-iron sheet alloys are produced in a grain-oriented state. The two usual configurations are the cube oriented (100) [001] and the cube-on-edge or Goss (110) [001] textures. The former has two cube edges or easy directions in the plane of the sheet and one perpendicular to it, while the latter has one easy direction in the plane of the sheet in the rolling direction and two at 45° to the plane of the sheet. Cube oriented silicon-iron has similar magnetic properties in the plane of the sheet both parallel and perpendicular to the rolling direction, while Goss textured material

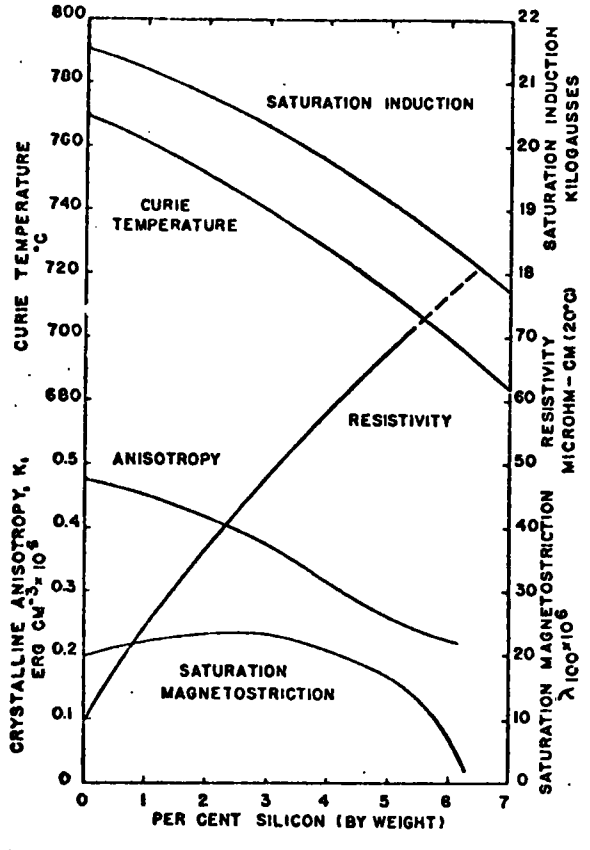

Figure 1.7 Variation of important properties of silicon-iron with composition (after Littmann, 1971).

has its best soft magnetic characteristics only along the rolling direction. The particular application determines the choice of material to be used.

Nickel-Iron Alloys:

Nickel-iron alloys of many different compositions are employed as soft magnetic materials. These are generally known as permalloys. The 50 Ni 50 Fe composition has the largest saturation induction in the range, is easily purified and has a fairly large electrical resistivity. In addition it is ductile and can be grain-oriented and magnetically annealed. Another interesting composition is 78 Ni 22 Fe which possesses small magnetostriction and magneto-crystalline anisotropy constants. Supermalloy which consists of 79 Ni 15 Fe 5 Mo 0.5 Mn exhibits the largest maximum permeability of commercially available materials, and has a very small coercive force. The elements present in small quantities have the effect of increasing the ductility and electrical resistivity, as for example in mumetal (75 Ni 18 Fe 2 Cr 5 Cu).

Cobalt-Iron Alloys:

Cobalt-iron alloys are also of interest despite the relatively high cost of cobalt and the difficulty of working the alloy. The 50 Co 50 Fe composition has a very high saturation induction and although the coercive force is not particularly low, it can be improved by magnetic annealing and the inclusion of 2% vanadium which also increases the ductility and electrical resistivity.

Evaporated-on Films:

Thin films of soft magnetic alloys in the thickness range 30-10,000 Å produced by deposition from the vapour have exhibited some interesting properties. Coercivities range from 1 to 300 Oe though obviously only the low values are of interest here. The composition 80 Ni 20 Fe when deposited in a magnetic field possesses an almost perfectly rectangular hysteresis loop of interest for storage and logical devices in computers.

Ferrites:

Certain ferrimagnetic materials, known as ferrites, have a very high electrical resistivity of the order of 10^6 to 10^9 times that of iron so that eddy current losses are effectively eliminated even at very high frequencies. The saturation magnetization of these materials is rather low however.

Table 1.1 compares typical figures for magnetic and electrical properties of commercial soft magnetic materials. As this thesis is concerned with the properties of iron foil the figures quoted are only for materials that can be prepared in the form of sheets.

1.7 Electrodeposition of Iron Foil

A great quantity of commercial soft magnetic materials are produced in sheet form for use in forming laminated cores in electrical applications. The production of sheet material from a cast metal or alloy is quite expensive, requiring several stages of rolling reduction with intermediate stress relieving anneals. The Sheffield firm of Hall and Pickles, operating on a license from the Central Electricity Generating

Table 1.1 Typical Magnetic and Electrical Properties of Commercial Soft Magnetic Sheet Materials

Material	Composition	Saturation Induction (G)	Coercive Force (Oe)	Maximum Permeability	Electrical Resistivity ($\mu\Omega$cm)
Fe (commercial)	99 Fe	21,500	0.9	5,000	10
Fe (purified)	99.95 Fe	21,500	0.05	180,000	10
Si-Fe (non oriented)	96 Fe 4 Si	19,700	0.5	7,000	60
Si-Fe* (grain oriented)	97 Fe 3 Si	20,000	0.15	30,000	47
50 Permalloy	50 Fe 50 Ni	16,000	0.05	100,000	45
78 Permalloy	22 Fe 78 Ni	10,700	0.05	100,000	16
Supermalloy	15 Fe 79 Ni 5 Mo 0.5 Mn	8,000	0.004	1,000,000	60
Mumetal	18 Fe 75 Ni 2 Cr 5 Cu	6,500	0.05	100,000	62
Permendur	50 Fe 50 Co	24,600	0.2	6,000	7
2V Permendur	49 Fe 49 Co 2 V	23,000	0.2	100,000	26

* Properties in rolling direction

Taken from Morrish (1965) and Weast (1975-6)

Board, have investigated the possibility of producing thin iron sheet or foil by a process of electrodeposition which potentially has several advantages over standard sheet production techniques. The process for the production of iron foil by electrodeposition will be outlined in this section; the discussion is limited to information supplied by the firm.

The electrolyte is an acid aqueous solution of ferrous chloride at high temperature which is fed continuously to the plating cell. The cell incorporates a horizontal slowly rotating titanium drum which acts as a cathode. This is partially wrapped with a concentric graphite anode which serves, in conjunction with seals at either end, to contain the electrolyte between the graphite and the drum. The spacing between the two electrodes is kept to a minimum to reduce ohmic dissipation in the cell.

When a current is passed through the cell, typically at 0.5 A cm^{-2}, ferrous ions are reduced to iron at the cathode drum

$$Fe^{2+} + 2e \longrightarrow Fe \downarrow \qquad (1.4)$$

Ferrous ions are oxidised at the anode to ferric ions

$$2\,Fe^{2+} \longrightarrow 2\,Fe^{3+} + 2e \qquad (1.5)$$

Overall

$$3\,Fe^{2+} \longrightarrow Fe \downarrow + 2\,Fe^{3+} \qquad (1.6)$$

The ferric rich electrolyte leaving the cell is contacted with scrap iron in the regeneration tanks

$$2\,Fe^{3+} + Fe \longrightarrow 3\,Fe^{2+} \qquad (1.7)$$

Equation 1.7 is the reverse of 1.6. Since a current is required to drive the deposition reaction 1.6, the dissolution reaction 1.7 must

be spontaneous. The reaction energy appears as a slight warming of the electrolyte in the regeneration tanks.

As with all electrochemical systems there are competing reactions. The most important one in this process is the reduction of hydrogen ions at the cathode

$$2\,H^{+} + 2e \rightarrow H_2 \uparrow \qquad (1.8)$$

Under normal operating conditions, the efficiency of iron deposition is better than 90% utilization of current, with the rest producing mainly hydrogen. Hydrogen production, apart from being hazardous, causes hydrogen embrittlement and lattice defects in the deposited iron which can have a serious effect on the mechanical properties.

The deposit of iron is easily peeled from the drum when it emerges from the electrolyte because of the presence of a thin electrically conducting layer of titanium oxide on the drum. The thickness of the foil is controlled by one or both of the current density and the speed of rotation of the drum, and is typically in the range 10 to 200 microns.

One of the major advantages of this process is that for thinner foils production costs decrease, in contrast to the economics of producing thin foils by rolling. Another large benefit is the conservation aspect as the foil can be produced from scrap iron.

Whether or not iron foil produced in this manner has any commercial value depends entirely on its properties, and it is an investigation of some of these which forms the major part of this thesis.

CHAPTER TWO

PROPERTIES OF AS-PRODUCED ELECTRODEPOSITED IRON FOIL

2.1 Introduction

The properties of the electrodeposited iron foil, particularly in relation to its possible use as a soft magnetic material, are of great interest in assessing its potential commercial value. In this chapter we will deal with various relevant properties of the foil in its as-produced form; later chapters will discuss various ways of improving these characteristics.

During the course of the project, 17 samples of the foil have been supplied; these vary in thickness from 12 to 155 microns. Most properties have been determined for all the samples and, where appropriate, measurements were made in directions both parallel and perpendicular to the direction of foil production in order to determine whether any anisotropic features are introduced by the manufacturing process.

2.2 Chemical Analysis of Foil

The chemical purity of the foil is obviously a very important consideration, particularly as magnetic properties are considerably affected by the presence of impurities. It is to be expected that a process of electrodeposition should yield a material of high purity and a chemical analysis, supplied by Messrs Hall and Pickles, of a typical foil sample supports this view. The analysis is as follows:-

Mn	< 0.001% by weight
Cu	0.034%
Co	0.008%
Ni	0.016%
Ti	< 0.01%
Si	< 0.002%
P	< 0.0005%
S	Probably 0.005%
C	About 0.002%

Thus the foil is better than 99.9% pure, a level attainable after standard casting production techniques only by purification, which entails considerable additional expenditure.

2.3 Structural Properties

2.3.1 Macrostructure of Electrodeposited Iron Foil

An interesting feature of the foil is the disparity between its thickness as measured using a micrometer screw gauge and that determined indirectly for a sheet of known area and mass using the value of density of iron of 7.86 g cm^{-3} quoted by Weast (1975-6). Figure 2.1 plots this "calculated" thickness against measured thickness for a considerable number of foil samples of all the thicknesses supplied. The "calculated" thickness is systematically about 15% less than the measured thickness. This feature occurs because although the face of the foil which was in contact with the titanium drum during deposition is quite smooth and lustrous, the other side is rather rough and dull, this asperity being included in the measured thickness. Except in the evaluation of the mechanical properties of the foil, the "calculated" thickness of the foil will be quoted; the reason for the exception will be explained in the

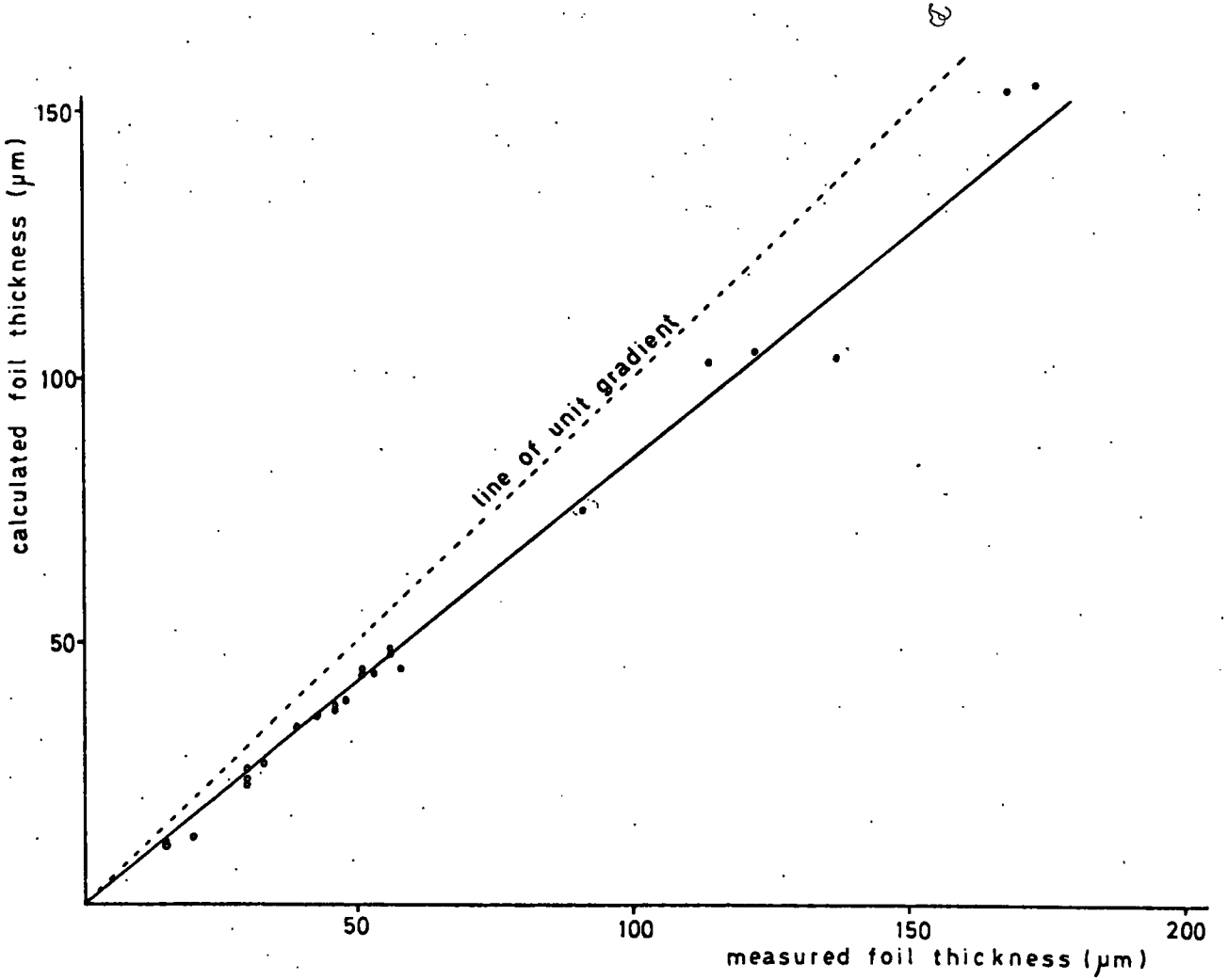

Figure 2.1 Calculated against measured foil thickness.

appropriate section.

2.3.2 Optical Study of Microstructure of Electrodeposited Iron Foil

All pure metals, except those produced in single crystal form by special techniques, are structurally similar, consisting of small, roughly polyhedral grains. Each grain is a crystal in its own right, despite the lack of a regular geometrical outline. This feature is a result of the fact that none of the crystals has had the opportunity for free growth, the grain boundaries being the "accidental" meeting lines of adjacent growing grains of different orientation.

The grain structure of a metal may be studied using an optical microscope. A flat metal surface gives a sectional view of the grains which appear, after suitable etching, as polygonal areas separated by dark lines. Etching is necessary to reveal the grain structure; it has the effect of chemically attacking the differently oriented grains at slightly differing rates, leaving steeply sloping surfaces at the grain boundaries which reflect incident light sideways and consequently appear as dark lines. The optical microscope has an ultimate resolution of about 0.25 micron and a similar depth of field (Bowen and Hall, 1975).

Optical microscopy has been used to study the grain structure of the as-produced electrodeposited iron foil. A flat, strain-free metal surface was first produced by mechanical and electrolytic polishing. The mechanical polishing was performed on a Metals Research Multipol polishing machine using successively finer diamond pastes down to diamond particles in the size range $\frac{1}{4}$ to 1 micron, and was continued until the iron surface appeared scratch free to the naked eye. The

surface strain introduced by the mechanical polishing was then relieved by a short period of electropolishing using the technique of Koves and Pesch (1963). The electrolyte consisted of 133 ml glacial acetic acid, 7 ml distilled water, and 25 g CrO_3. Polished samples typically 1 cm square were produced in this way and the grain structure was then revealed by chemically etching for between 5 and 10 minutes with a solution of $FeCl_3$ in 30% hydrochloric acid. The grain structure was observed using a Vickers M17 Industrial Microscope and a typical picture obtained from a foil sample of thickness 155 microns is shown in figure 2.2.

It can be seen from the figure that the grain size of the foil is rather small and irregular, with details of a size which is approaching the resolution limit of the microscope. It is not possible to make more than a few semi-quantitative observations on the grain structure as revealed optically. The grain size, though rather irregular, appears to be of the order of a few microns on average. The grain structure appears similar when studied from either the rough or smooth sides of the foil, and is similar for foil samples of different thicknesses.

Clearly it may be advantageous to study the grain structure of the as-produced foil using a technique of superior resolution to optical microscopy and with this aim in mind, the use of the scanning electron microscope will be discussed in the next section.

2.3.3 Scanning Electron Microscopy of As-Produced Iron Foil

The scanning electron microscope (S.E.M.) is an instrument designed primarily for studying the surfaces of solids at high magnification.

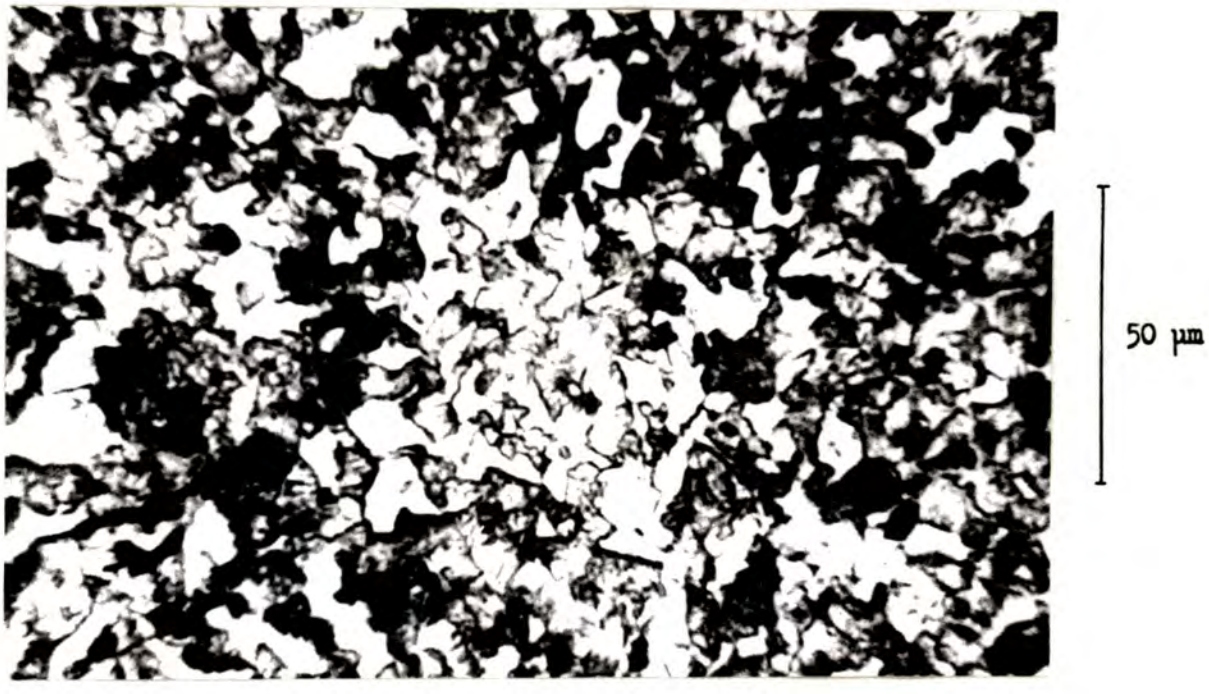

Figure 2.2 Optical photograph of as-produced grain structure.

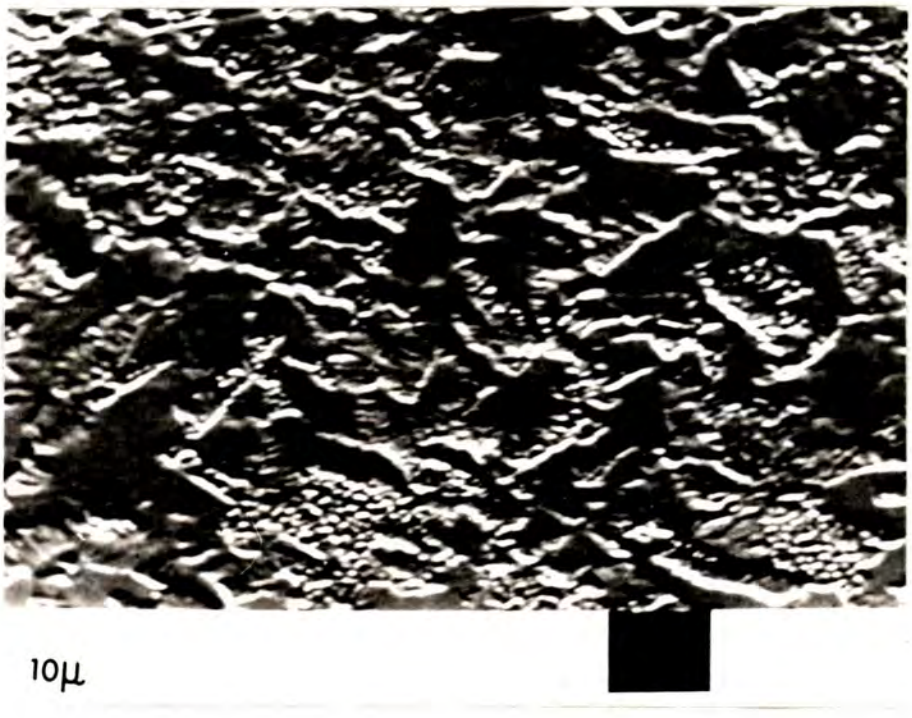

Figure 2.3 Scanning electron micrograph of as-produced grain structure.

It is superior to the optical microscope in both resolution (typically 0.015 micron) and depth of field (up to several millimetres). In the S.E.M. a fine, high energy beam of electrons is focused to a point on the specimen, causing the emission of secondary electrons with a wide spread of energies from that point. Either these electrons, or the straightforward back reflected primary electrons are collected and amplified to give an electrical signal which is used to modulate the intensity of the beam of electrons in a cathode ray tube display. Each point on the cathode ray tube display corresponds to a point on the specimen surface. To build up a complete image the electron beam in the microscope is scanned over an area of the specimen surface, while the beam in the cathode ray tube is scanned over a geometrically similar area.

The surface relief of the specimen under examination gives rise to what is known as topographic contrast. The yield of primary and secondary electrons is strongly dependent upon both the angle of incidence of the electron beam and the angle of collection of emitted electrons, so that variations in the local angle of inclination of the surface cause variations in the intensity of collected electrons. The image obtained appears to be shadowed and exhibits a strikingly three dimensional form. For further details of scanning electron microscopy, reference is made to Bowen and Hall (1975) and Booker (1969).

In the study of the grain structure of as-produced electrodeposited iron foil, a Cambridge scanning electron microscope was used in the emissive mode. Topographic contrast of the surface relief produced by the polishing and etching technique discussed in section 2.3.2 was employed

to reveal the grain structure. Figure 2.3 shows a typical picture obtained from a sample of foil of thickness 155 microns. The electron beam accelerating voltage was 15 kV, and a 20 second scan was used to produce the picture which was recorded on standard 35 mm film. As in the case of optical microscopy of the foil, an irregular grain structure is observed with some large grains up to 10 microns across separated by similar regions displaying considerable substructure of the order of a micron or less in size. Evidently the average grain size is of the order of a micron, confirming the data obtained with the optical microscope.

2.3.4 X-Ray Diffraction Studies of Iron Foil

The technique of taking x-ray diffraction or Laue patterns of a single crystal for orientation purposes is well known; it can also be used to yield information on the grain size and orientation of a polycrystalline material.

The Kα line of the chosen target element is used as an effectively monochromatic source, the Kβ line and continuum radiation being considerably reduced in intensity by the insertion of a suitable x-ray filter whose K absorption edge lies at a wavelength just below the Kα line of the target element. The beam is collimated with a fine metal tube.

When this effectively monochromatic x-ray beam is incident upon a polycrystalline material, diffraction occurs from all grains which are suitably oriented to satisfy the Bragg equation:

$$2d \sin \theta = n \lambda \qquad (2.1)$$

Here λ is the wavelength of the x-radiation, d is the lattice spacing of the particular set of diffracting crystallographic planes in the grain, n is the order of diffraction, and θ is the diffraction angle as illustrated in figure 2.4 for both back reflected and transmitted diffracted beams. In both cases, as λ and n (normally unity) are fixed and d has only discrete values, given for the body centred cubic structure of iron by;

$$d = a\,(h^2 + k^2 + l^2)^{-\frac{1}{2}} \qquad (2.2)$$

where a is the lattice parameter and (h, k, l) the Miller indices of the diffracting planes, it follows that the diffraction angle θ can only have discrete values. It should be noted in passing that diffraction theory imposes the restriction that the sum of h, k and l be an even integer. Each set of diffracting planes can therefore give rise to a diffracted spot on the recording film which can lie anywhere on a circle whose radius is determined geometrically by the diffraction angle θ and the specimen to film distance.

For a polycrystalline sample, the incident x-ray beam may impinge upon very many grains so that each diffraction condition is satisfied a number of times and each circle on the film exhibits many diffracted spots. If the grain size is very much less than the beam area, the spots can overlap to form continuous rings and Adam (1960) gives guidelines for estimating grain size from a study of the diffraction pattern for a beam of diameter about 1 mm, a very typical figure. The rings may be classed as:-

(a) Discontinuous or spotty; here a relatively small number of grains are irradiated by the beam and the average grain size is greater than 10^{-2} mm.

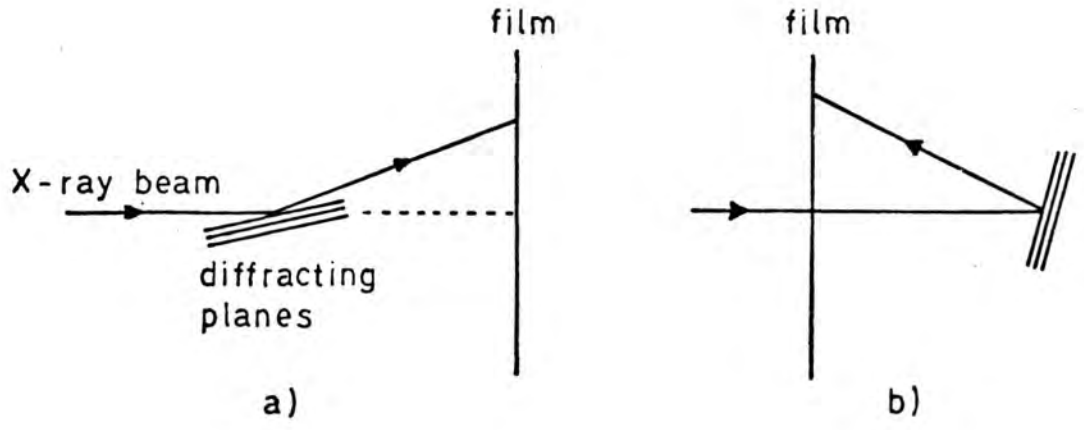

Figure 2.4 Experimental arrangement for producing a) transmission and b) back reflection Laue photographs.

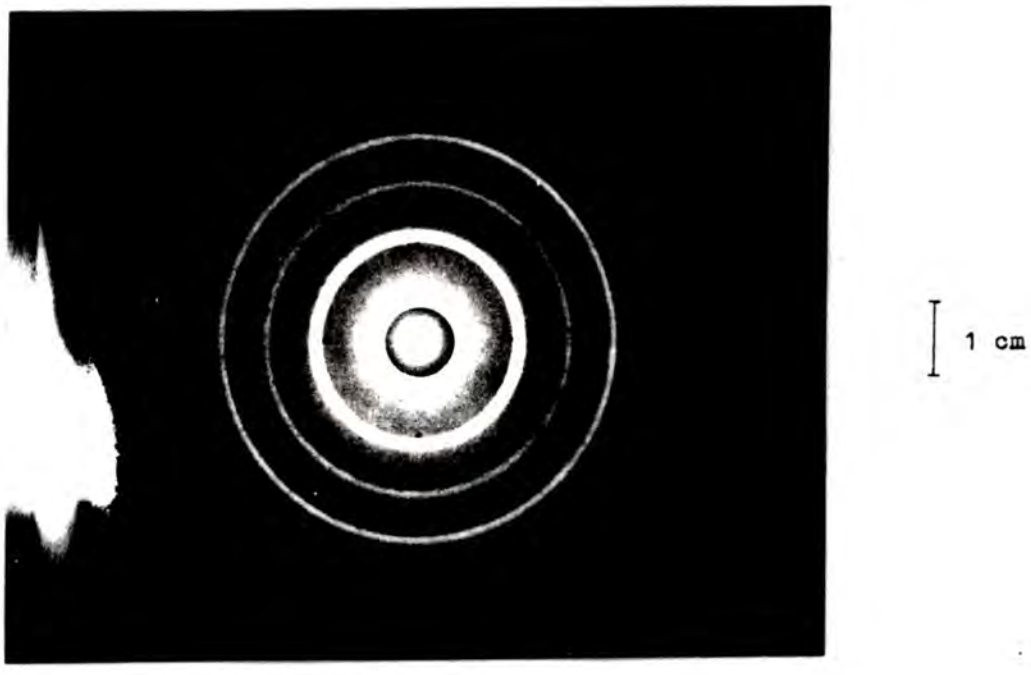

Figure 2.5 Transmission Laue photograph of as-produced iron foil.

(b) Sharp continuous; grain size of the order of 10^{-3} mm.

(c) Broadened continuous; appreciable broadening of the rings becomes apparent with grains smaller than 10^{-4} mm.

Any preferred orientation of the grains should lead to a concentration of the diffracted spots at particular points on the rings, a subject covered by Hargreaves (1960).

In the study of the as-produced iron foil, both transmission and back reflection Laue patterns have been produced. Molybdenum Kα radiation (λ = 0.711 Å) was used with a zirconium filter (absorption edge λ = 0.687 Å). The tube voltage employed was 50 kV at a current of 20 mA. The patterns were recorded on Polaroid 4 x 5 Land Film Type 57, exposures of 20 minutes being suitable. The specimen to film separation was the standard 3 cm. Figure 2.5 shows a typical transmission pattern obtained when the x-ray beam passes normally through a foil sample of thickness 45 microns. The rings are identified, working outwards, as the diffracted beams from the (110), (200), (211), (220) and (310), lattice planes. Following the categorisation of Adam the continuous nature of the rings suggests a maximum grain size of about 10^{-3} mm or 1 micron, in good agreement with optical and S E.M. data. There is no indication of any preferred orientation in the plane of the foil. In order to determine whether any preferred orientation exists normal to the plane of the foil, several sheets of foil of thickness 155 microns were glued together and a back reflection pattern of the sheet edges taken. Again no preferred orientation was observed.

2.4 Mechanical Properties

2.4.1 Introduction

The mechanical properties of the iron foil are of interest both from an academic point of view and in determining whether the material could withstand the rigours of any technical application. The data is also valuable in a later chapter in assessing the feasibility of strain-anneal techniques for inducing recrystallization in the foil.

2.4.2 The Stress-Strain Curve

The required information is determined in a tensile test in which the foil is strained at a constant rate and the load on the specimen measured simultaneously with the extension. In order to take into account the physical dimensions of the specimen, the terms tensile stress, defined as load per unit cross sectional area and linear strain, defined as extension per unit length are normally employed.

A typical stress-strain curve for a metal specimen is shown in figure 2.6. The initial linear portion of the curve corresponds to reversible elastic elongation of the specimen as the atoms are displaced slightly from their equilibrium positions. Above the yield stress (σ_y) the curve departs from linearity and the deformation becomes plastic. If unloaded now the specimen would show a permanent extension. Plastic deformation takes place by slip, that is the movement of favourably orientated crystal planes over one another. This in turn occurs by the movement of dislocations across the slip planes. The stress required to move the dislocations determines the yield stress of a crystal. Polycrystalline materials are more difficult to deform than single crystals because the grain boundaries act as "strengthening ribs" inhibiting dislocation

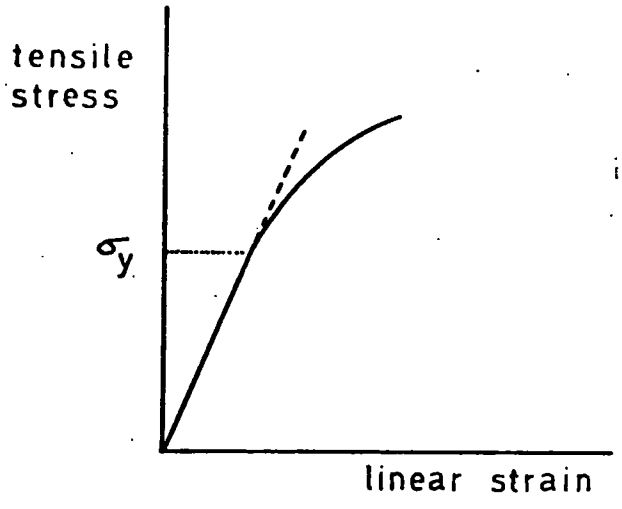

Figure 2.6 Typical stress-strain curve for a polycrystalline metal.

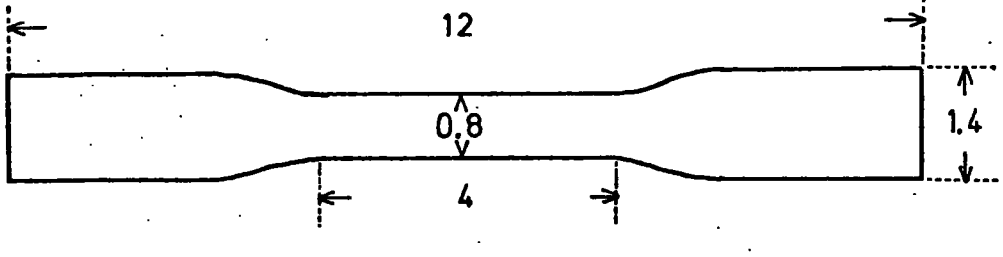

Figure 2.7 Tensile test piece dimensions (figures in cm).

movement and preventing the formation of large slip planes. As plastic deformation proceeds, more dislocations are generated; those moving on intersecting slip planes tend to interact and become entangled so that a greater force is required to move them. Thus the stress continues to increase with strain in the phenomenon known as work-hardening. A point is reached where the applied load reaches a maximum as the decrease in cross sectional area of the test piece is sufficient to account for the increase in stress. Eventually the strain becomes localized and a constriction or "neck" forms in the test piece, the load drops and fracture follows. The subject of dislocations and the stress-strain curve is covered by Hull (1975) and Martin (1969).

The yield stress of a metal is dependent on many factors; it increases with decreasing temperature, with increasing strain rate and with increasing impurity content. However all these factors are held constant in the present experiment. The dependence of yield stress on grain size will be covered in a later chapter.

2.4.3 Experimental Technique

The properties which have been measured are the yield stress, ultimate tensile stress and percentage elongation at fracture defined respectively as:-

$$\text{Yield Stress} = \frac{\text{Load at Yield Point}}{\text{Original Cross Sectional Area}} \quad (2.3)$$

$$\text{Ultimate Tensile Stress} = \frac{\text{Maximum Load}}{\text{Original Cross Sectional Area}} \quad (2.4)$$

$$\text{Percentage Elongation at Fracture} = \frac{\text{Extension at Fracture} \times 100}{\text{Original Length}} \quad (2.5)$$

The tensile testing was carried out on a Hounsfield Tensometer. The test piece dimensions are shown in figure 2.7. The foil is sufficiently thin to allow the test pieces to be cut out with scissors. The width and length of the gauge portion of the test pieces were measured with a rule and the thickness with a micrometer screw gauge. The shape of the test pieces made it impossible to calculate the true foil thickness as detailed in section 2.3.1, so the measured thickness was used in calculating the cross sectional area of the test piece gauge portion. A suitable correction could be applied if desired using figure 2.1.

A sample load against extension curve for a foil sample of thickness 101 microns is shown in figure 2.8. The curve was used in conjunction with the measured test piece width and thickness and equations 2.3 and 2.4 to calculate the yield stress and ultimate tensile stress of the test piece. The percentage elongation at fracture was calculated by placing together the fractured portions of the test piece and measuring the extended gauge length.

Each foil sample was tested three times in directions both parallel and perpendicular to the direction of foil production. The average of the three measurements for each case is presented in table 2.1. An estimated measuring error is quoted. All tensile tests were performed at room temperature and at a straining rate of 1.6 mm min^{-1}.

Six of the seventeen foil samples do not appear in table 2.1; of these samples 7, 11 and 12 are very thin and tore at the grips of the tensometer, sample 2 is very brittle and does not yield reproducible results, and samples 16 and 17 were supplied without information on the

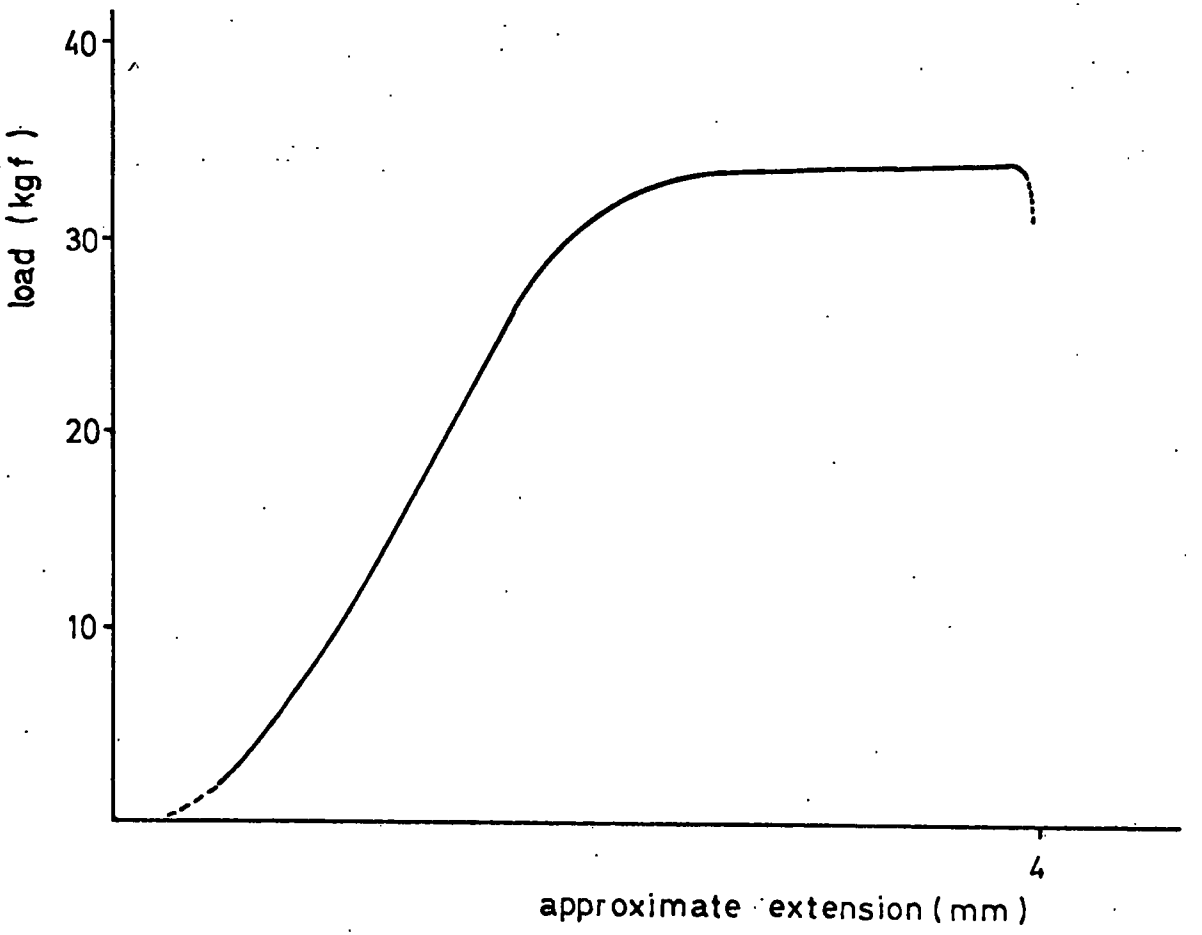

Figure 2.8 Sample load against extension curve for as-produced iron foil.

TABLE 2.1 MECHANICAL PROPERTIES OF AS-PRODUCED FOIL

Sample Number	Nominal Thickness (μm)	Yield Stress ($kg\ mm^{-2}$) Parallel (± 5%)	Yield Stress ($kg\ mm^{-2}$) Perpendicular (± 5%)	Ultimate Tensile Stress ($kg\ mm^{-2}$) Parallel (± 5%)	Ultimate Tensile Stress ($kg\ mm^{-2}$) Perpendicular (± 5%)	Percentage Elongation at Fracture Parallel (± 0.5)	Percentage Elongation at Fracture Perpendicular (± 0.5)
1	45	31.4	35.0	39.8	46.1	5.4	5.3
3	44	40.2	35.6	51.2	45.5	1.1	1.0
4	26	31.3	27.2	42.3	36.2	2.1	1.1
5	35	28.4	27.9	37.6	38.0	3.9	4.2
6	155	30.1	31.4	37.9	37.9	6.5	6.5
8	49	26.0	30.4	34.3	38.3	3.9	*
9	39	25.6	27.5	33.5	34.2	3.0	*
10	101	29.3	27.3	37.2	34.6	8.9	8.8
13	24	27.2	28.2	34.3	34.7	1.3	1.4
14	35	28.5	31.0	37.8	39.3	3.6	2.9
15	48	27.1	29.4	36.3	37.8	4.8	4.0

* Individual results very erratic

direction of production. The other eleven samples produce fairly consistent yield stress and ultimate tensile stress results, though the percentage elongation figures are rather erratic. Uncharted variations in deposition conditions and impurity levels may well account for the differences. There is no apparent anisotropy in the properties, the average yield stress and ultimate tensile stress over all samples being as follows:-

Parallel	- Yield Stress	=	29.6 ± 1.2 kg mm^{-2}
	Ultimate Tensile Stress	=	38.4 ± 1.5 kg mm^{-2}
Perpendicular	- Yield Stress	=	30.1 ± 0.9 kg mm^{-2}
	Ultimate Tensile Stress	=	38.4 ± 1.2 kg mm^{-2}

2.5 Magnetic Properties

2.5.1 Introduction

The 50 Hz magnetic properties of the electrodeposited iron foil are of particular interest in assessing whether the foil may have any alternating current applications. A hysteresis loop plotter has been constructed to measure the coercive force of single strip samples of the foil. Minor hysteresis loops have been used to construct the magnetization curve from which the maximum permeability can be estimated. The design of the loop plotter evolved from a study of the general review of Oguey (1969) and the single sheet tester of Yamamoto and Ohya (1974). Figure 2.9 shows in block form the general components of any hysteresis loop plotter.

The primary coil, which is fed by the 50 Hz A.C. power supply, supplies the alternating magnetic field which magnetizes the sample. The field (H) in this coil is proportional to the current (I) flowing through it;

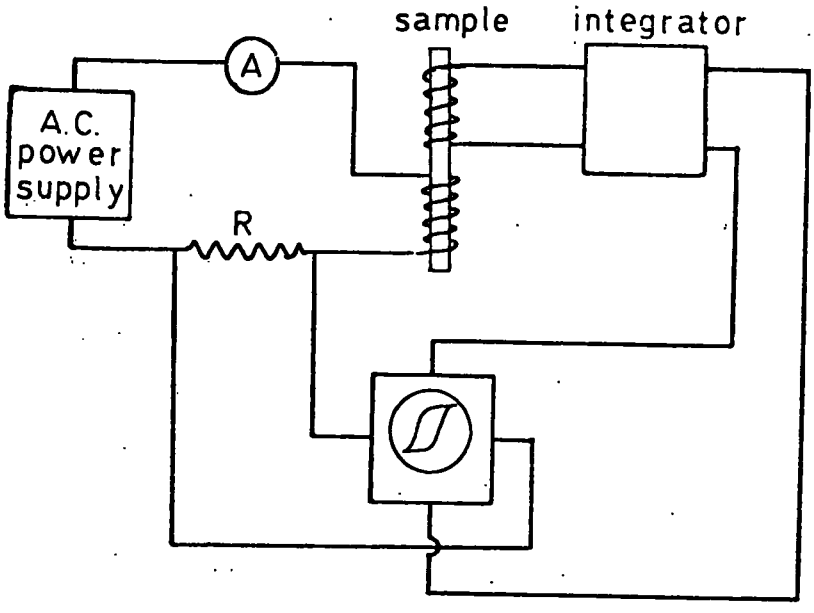

Figure 2.9 Block diagram of hysteresis loop plotter.

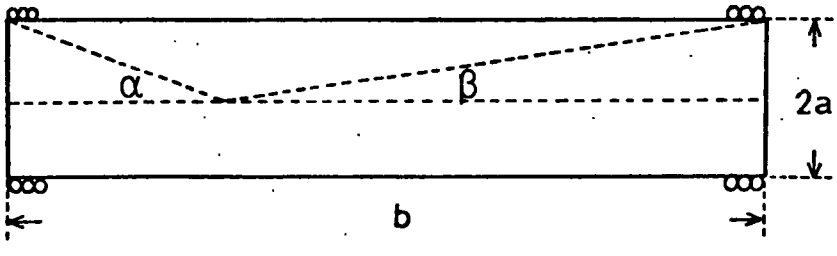

2a = 4.15 cm
b = 20.05 cm

Figure 2.10 Solenoid dimensions.

a signal proportional to H is displayed on the X-plates of the oscilloscope by means of the voltage dropped across the series resistor (R).

The signal induced in the secondary coil is proportional to the rate of change of induction $\frac{dB}{dt}$ of the sample; this is integrated and fed to the Y-plates of the oscilloscope, so that the Y deflection is proportional to the induction (B).

2.5.2 Details of Hysteresis Loop Plotter

The design of the heart of the loop plotter, the coil system, revolves around the choice of sample geometry. In the case of the electro-deposited iron foil, a simple rectangular strip is clearly most convenient.

It is necessary at this stage to consider the effects of the demagnetizing field due to the free magnetic poles at the ends of a magnetized strip. Because of the demagnetizing effect, the field (H) inside the specimen is smaller than the applied field (H_{app}) by an amount given by NM where N is a demagnetizing factor dependent on the sample geometry and M is the magnetization per unit volume of the sample.

$$H = H_{app} - NM \qquad (2.6)$$

N can only be calculated explicitly for ellipsoidal specimens; the solutions in the case of rod and strip samples require approximations and are very tedious. The effect of the demagnetizing field is to shear the hysteresis loop and magnetization curve in a clockwise manner,

decreasing the measured values of the remanent induction and permeabilities. The coercive force should not be affected as this is the field corresponding to zero magnetization.

The problem can be eliminated by providing a flux closing yoke linking the two ends of the specimen in which case no free magnetic poles are involved. Unfortunately it proved impossible to obtain a suitable yoke, so an open flux arrangement was adopted and corrections made to the measured value of the maximum permeability. These will be described in due course.

The pick up and magnetizing coils were designed to accommodate strip samples 5 cm long and 1 cm wide. It was decided that a solenoid represented the simplest way of supplying the magnetizing field. It is necessary to ensure that the field in the solenoid is constant over the length of the sample. Pugh and Pugh (1960) give the field in oersteds at a point on the axis of a solenoid as

$$H = 0.2\pi NI (\cos\alpha + \cos\beta) \qquad (2.7)$$

where N is the number of turns per centimetre, I the current in amps and the angles and are defined in figure 2.10. The solenoid was designed so that the field over the 5 cm length of the specimen varied by less than 1% and the final dimensions were as follows: solenoid length = 20.05 cm, mean diameter of windings = 4.15 cm and number of turns = 479. From equation 2.6 the field at the centre of the solenoid is given by

$$H = 29.4 \quad \text{Oe A}^{-1} \qquad (2.8)$$

The pick up coil to measure the rate of change of induction of the sample was wound on a hollow perspex former 5 cm long, 1.8 cm wide and 0.25 cm

deep, up the centre of which the iron foil samples could easily be slotted. A coil of 500 turns was found to provide adequate sensitivity; sufficient in fact to detect the air flux in the gaps around the iron sample and in the perspex former. This contribution to the output signal was removed by the inclusion in series of an identical pick up coil wound so that in the absence of an iron sample the output from the two coils was always zero. The arrangement of the coils is illustrated in figure 2.11. The pick up coil system, after integration, now strictly measures (B-H) or $4\pi M$ (equation 1.1) for the iron foil but since B is always of the order of 3 orders of magnitude greater than H, the vertical axis of the hysteresis loops can effectively be labelled induction (B). The whole pick up coil assembly could readily be inserted up the middle of the solenoid to a reproducible central position determined by the location of a suitable stop.

The electronic integrator which operated on the output from the coil system was based closely on that used by Mundell (1976). A circuit diagram is shown in figure 2.12. All other loop plotter components were quite standard and will not be detailed here.

2.5.3 Results

Fifteen of the foil samples were tested 3 times both in directions parallel and perpendicular to the direction of foil production. The foil strips were magnetized to saturation and the coercive force (H_c) measured from the oscilloscope display of the hysteresis loop. Each figure in table 2.2 is the average of the values obtained from the 3 test pieces. An estimated measuring error is quoted. A sample hysteresis loop for a foil sample of thickness 101 microns is displayed in figure 2.13.

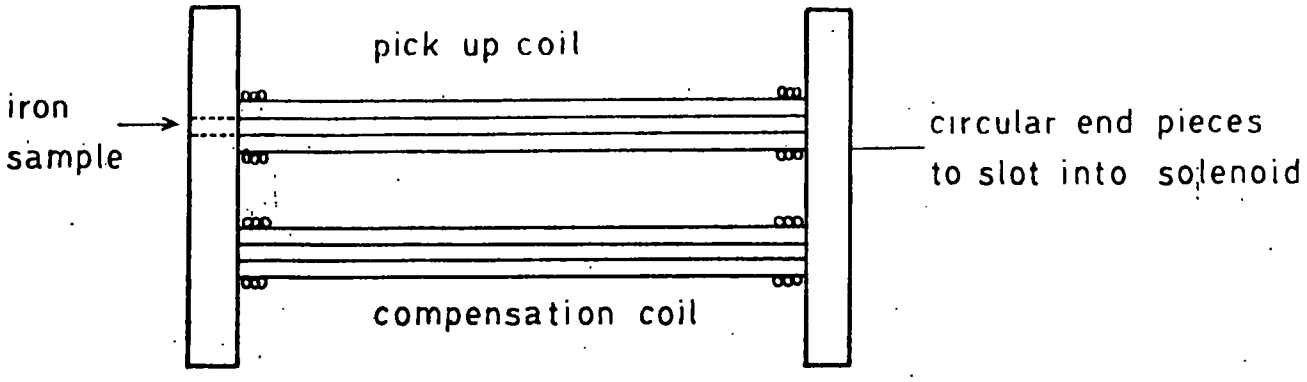

Figure 2.11 Arrangement of pick-up and compensation coils.

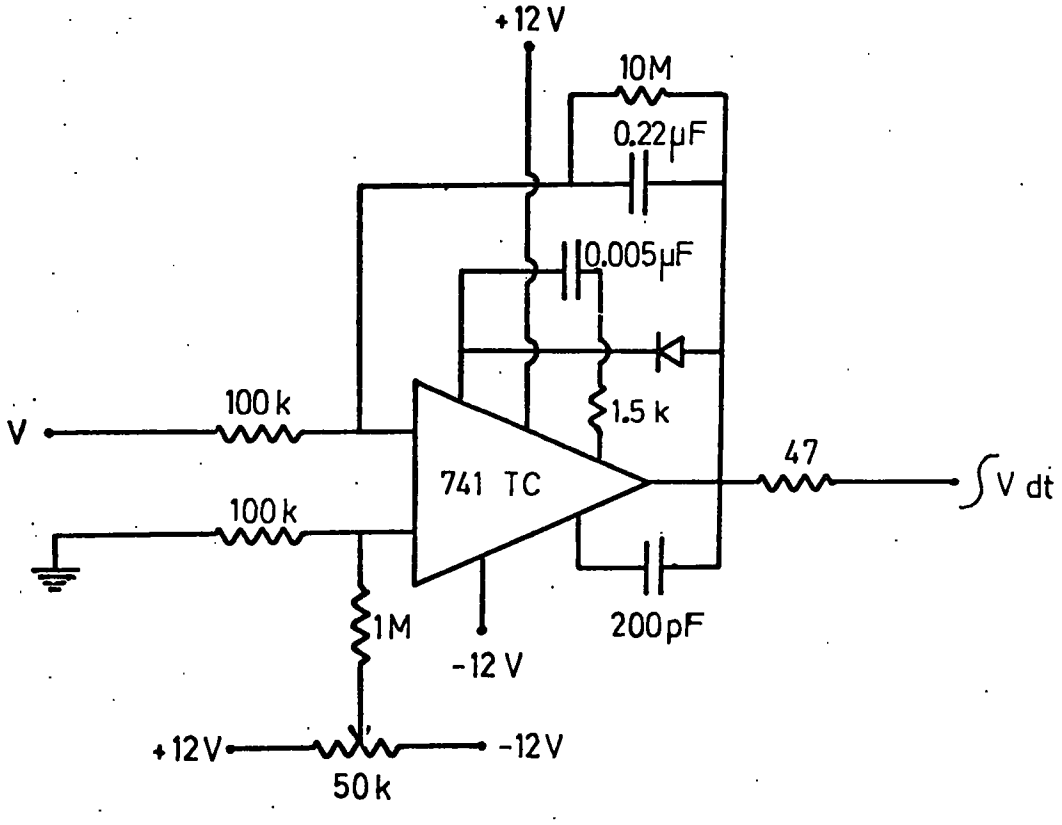

Figure 2.12 Circuit diagram for hysteresis loop plotter integrator.

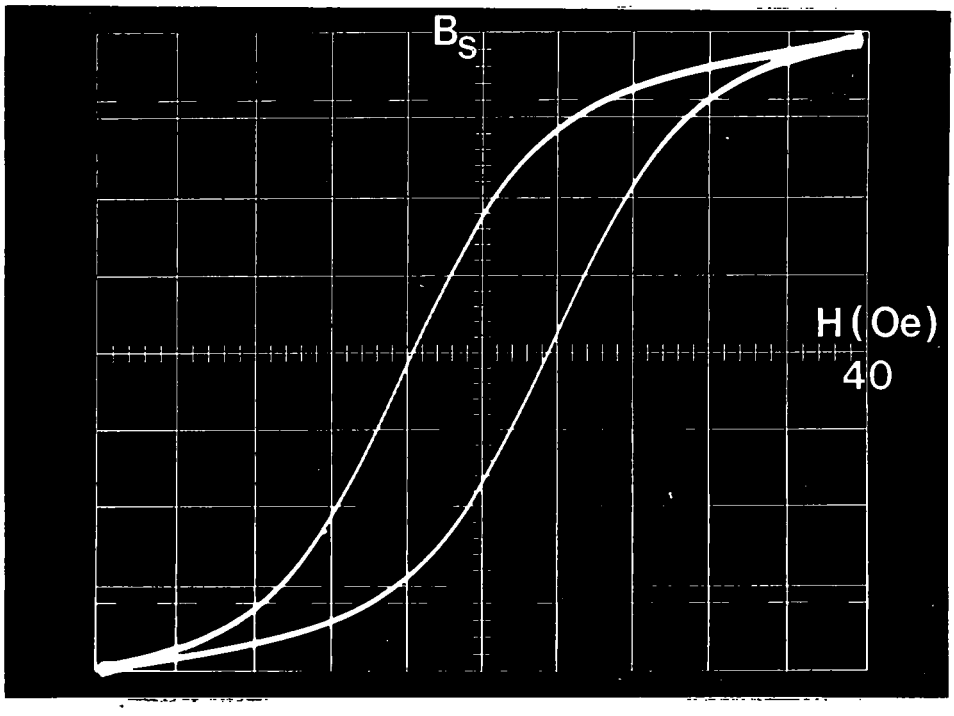

Figure 2.13 Sample hysteresis loop for as-produced iron foil.

TABLE 2.2 COERCIVE FORCE OF AS-PRODUCED FOIL

Sample Number	Nominal Thickness (μm)	Coercive Force (Oe) (± 5%)	
		Parallel	Perpendicular
1	45	7.9	7.8
2	44	9.9	9.2
3	44	8.2	7.8
4	26	7.5	8.1
5	35	7.3	7.6
6	155	7.6	7.5
7	12	8.7	8.5
8	49	6.6	6.6
9	39	6.8	6.7
10	101	7.3	7.0
11	12	8.8	8.8
12	13	7.2	6.9
13	24	7.0	7.2
14	35	7.6	7.5
15	48	6.8	6.9

From table 2.2 it can be seen that the coercive force is fairly consistent for all the foil samples and is not systematically directionally dependent. The average values of H_c over all the foil samples are as follows:-

Parallel - Coercive Force = 7.66 ± 0.23 Oe

Perpendicular - Coercive Force = 7.61 ± 0.20 Oe

As explained in section 1.3.1 the minor hysteresis loops can be used to construct the magnetization curve of the foil. The maximum value of the sinusoidal magnetic field in the solenoid was raised stepwise from zero to saturation, and at each stage the minor hysteresis loop was photographed. The (B, H) co-ordinates of the loop tips in both first and third quadrants was noted and averaged in case the loop was not accurately centred on the oscilloscope graticule. The average values of B and H were then plotted to yield the magnetization curve of the foil from which the maximum permeability can be estimated. Because of the effect of the demagnetizing field the measured value of the maximum permeability is less than the true value. The effect increases with increasing foil thickness because the regions of free poles at the ends of the samples and hence the demagnetizing factor (N) increase. An infinitely thin sample would be expected to have no demagnetizing factor, so the true maximum permeability has been estimated by plotting the measured value against foil thickness and extrapolating to zero thickness. Data was obtained for three foil samples, the thickness being varied by gluing together various numbers of strips. A set of magnetization curves obtained in this way for one of the foil samples is shown in figure 2.14. The measured maximum permeability for all the samples is plotted as a function of foil thickness in figure 2.15 and linear

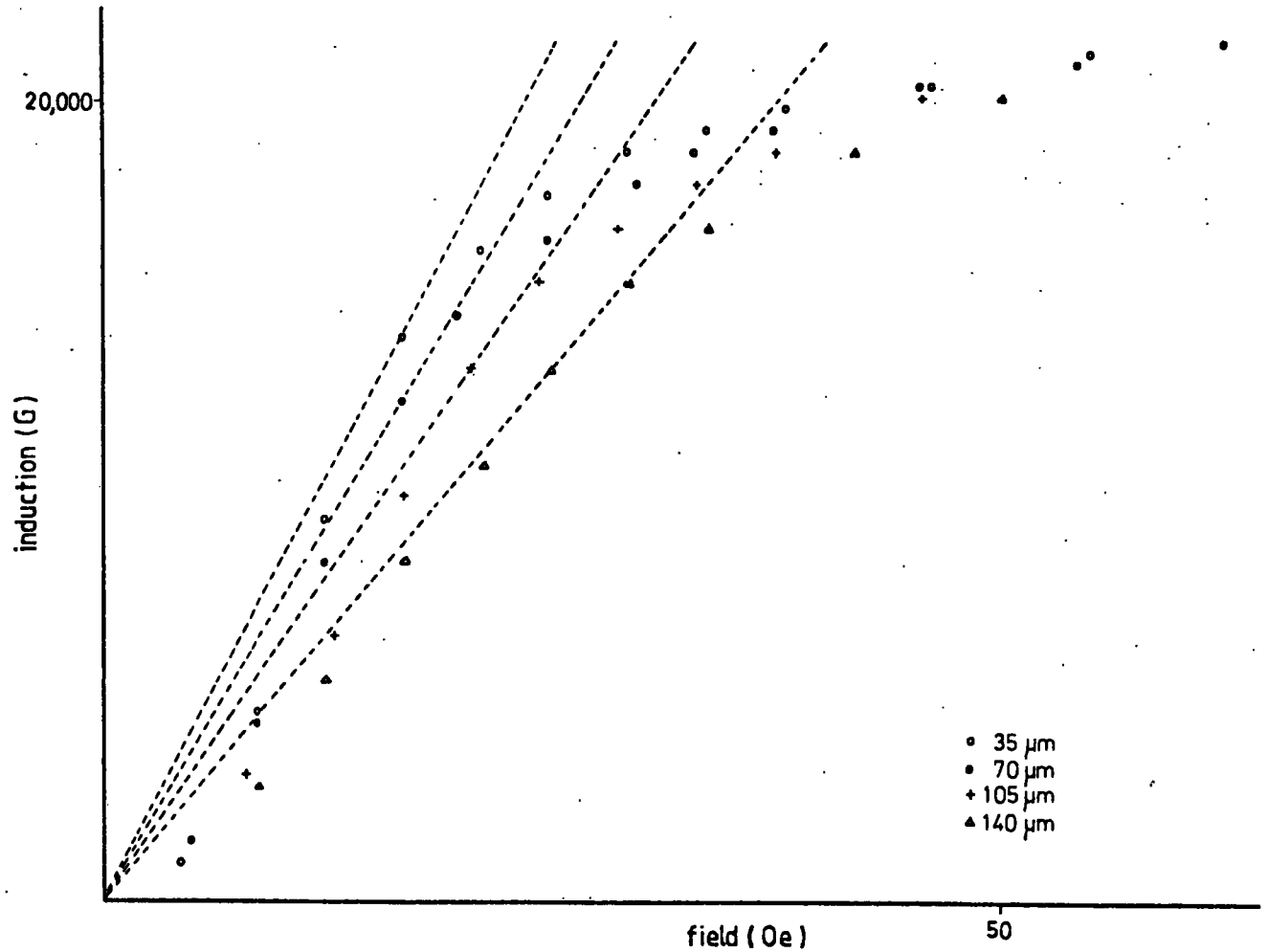

Figure 2.14 Derivation of maximum permeability from magnetization curves for four thicknesses of as-produced sample 14 foil.

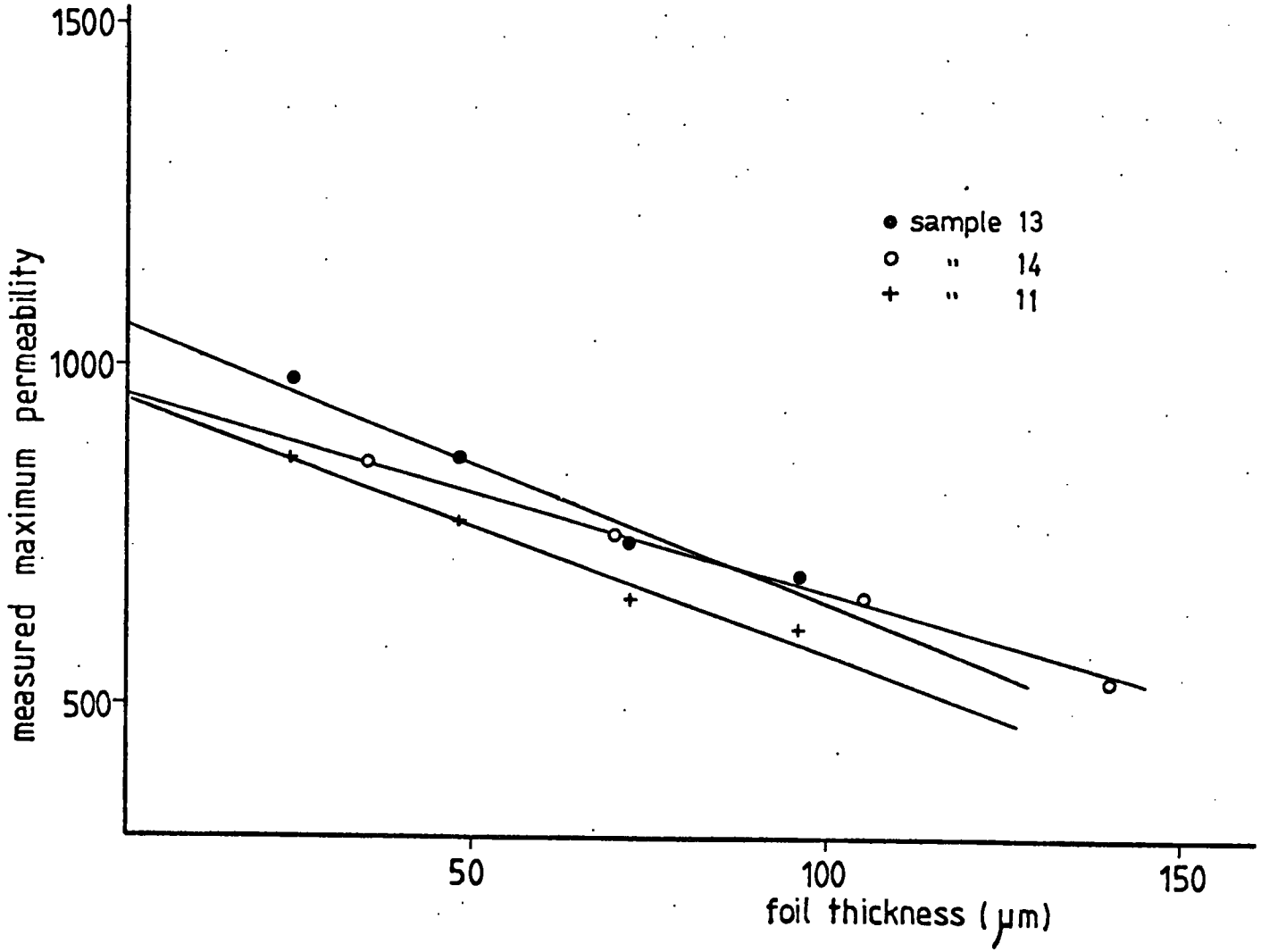

Figure 2.15 Measured maximum permeability against foil thickness for three as-produced foil samples.

extrapolations were used to obtain values of maximum permeability corresponding to zero foil thickness. The three values obtained are fairly consistent and yield an average figure for the maximum permeability of 990 ± 50.

2.6 Electrical Resistivity

2.6.1 Introduction and Apparatus

Because of the inverse dependence of eddy current losses on electrical resistivity mentioned in section 1.6.1 this property is of great importance in deciding whether the iron foil is likely to have any alternating current applications.

A simple apparatus for measuring the resistivity of strip samples of foil 5 cm long and 1 cm wide was constructed. The circuit is shown in figure 2.16 and the sample holder in figure 2.17. A known current (I), measured with a milliammeter, was passed through the strips which were clamped at each end between brass blocks supported on a perspex base. The voltage (V) between two spot-welded terminals up the centre of the foil strip was measured with a digital voltmeter (D.V.M.). The reversing switch was used to pass the current through the foil in both directions; the average value of V was taken. The separation (d) in cm of the spot-welded terminals was measured with a rule. The cross sectional area (A) in cm^2 of the foil was calculated from the measured mass and length and known density of the foil strip. The resistivity (R) in $\mu\Omega$cm of the foil is then given by

$$R = \frac{VA}{Id} \qquad (2.9)$$

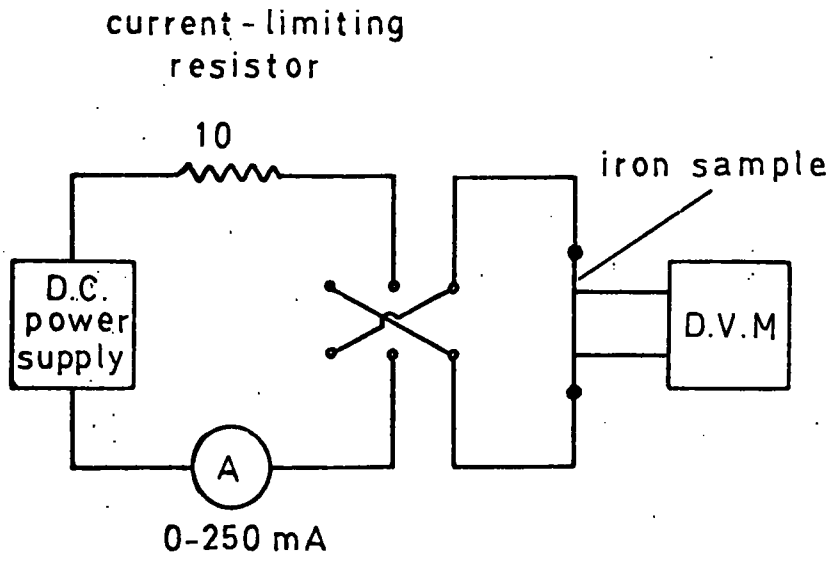

Figure 2.16 Block diagram of resistivity measuring apparatus.

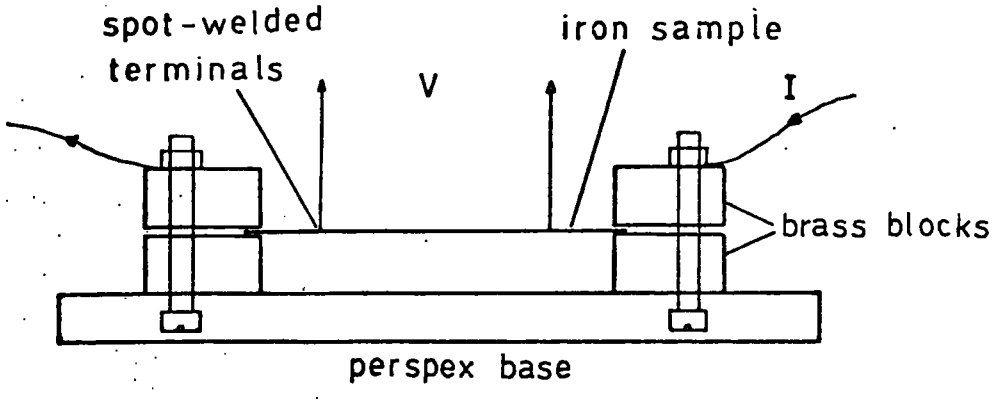

Figure 2.17 Diagram of sample holder used in resistivity measuring apparatus.

2.6.2 Results

Ideally the resistivity of each test piece should have been calculated using the gradient of a voltage-current graph. However this would have entailed the plotting of a very large number of graphs, so for each test strip the voltage was measured for a single current value of 100 mA. A sample V-I graph for a test piece of thickness 26 microns (figure 2.18) passes accurately through the origin and justifies the simplified means of calculating R.

Foil samples 7, 11 and 12 proved too thin to allow spot welding but 12 other foil samples were tested 3 times both in directions parallel and perpendicular to the direction of foil production. The average values of resistivity are quoted in table 2.3 along with an estimated measuring error. Resistivity is expected to be an isotropic property and this is confirmed by the lack of systematic variation between parallel and perpendicular directions. The average values for the two directions are as follows:-

Parallel - Resistivity = 10.36 ± 0.04 $\mu\Omega$cm

Perpendicular - Resistivity = 10.39 ± 0.05 $\mu\Omega$cm

These values are in good agreement with the resistivity of pure iron quoted in table 1.1.

2.7 Summary and Conclusions

The properties of the as-produced electrodeposited iron foil will be summarized briefly here. Chemically the foil is better than 99.9% pure by weight. Macroscopically the foil possesses one smooth, lustrous

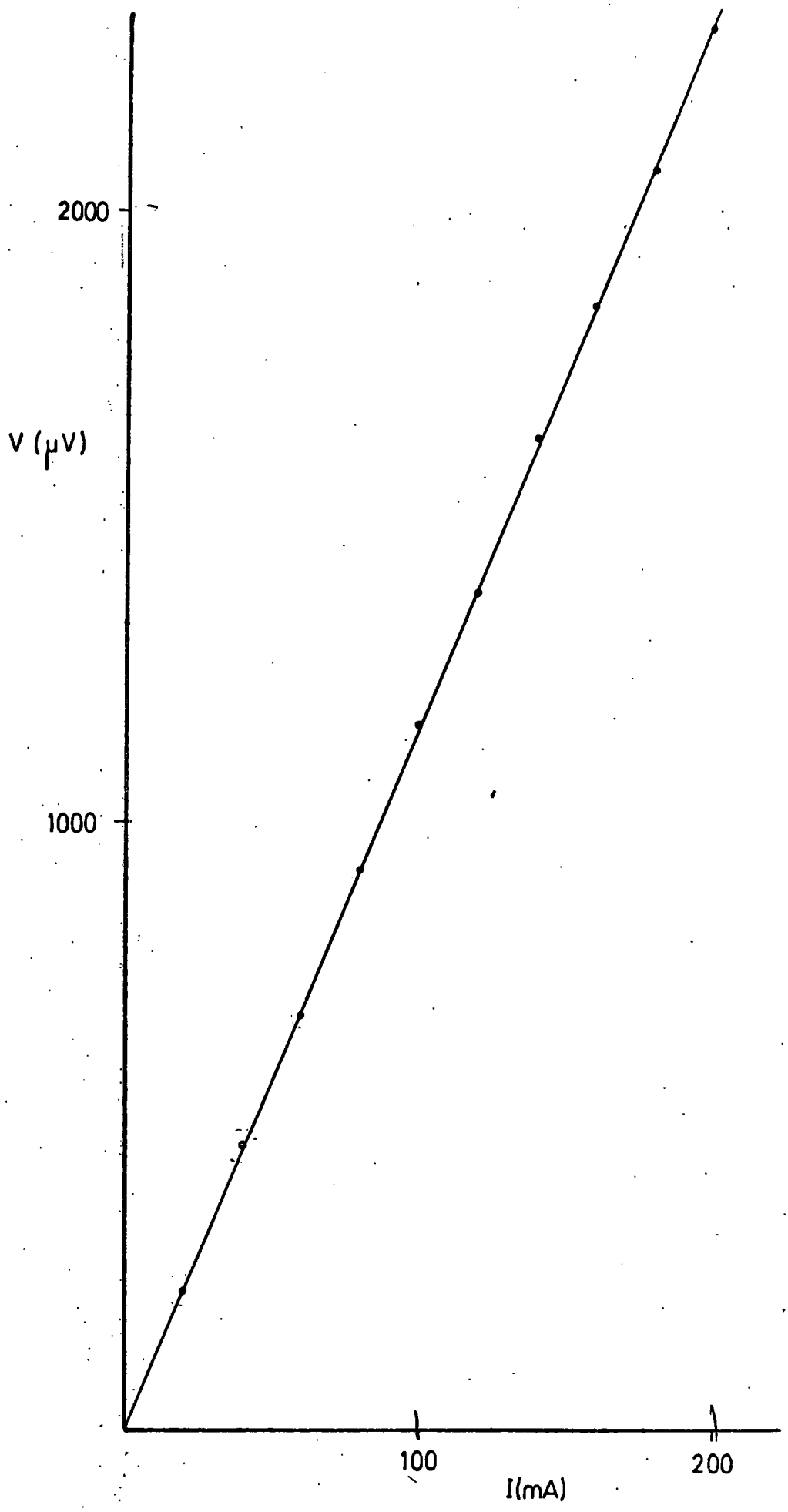

Figure 2.18 Sample voltage against current graph obtained from resistivity measuring apparatus.

TABLE 2.3 RESISTIVITY OF AS-PRODUCED IRON FOIL

Sample Number	Nominal Thickness (m)	Resistivity ($\mu\Omega$cm) Parallel ($\pm$ 5%)	Perpendicular
1	45	10.5	10.4
2	44	10.3	10.8
3	44	10.6	10.6
4	26	10.5	10.4
5	35	10.3	10.4
6	155	10.3	10.3
8	49	10.3	10.2
9	39	10.3	10.3
10	101	10.2	10.1
13	24	10.4	10.4
14	35	10.4	10.5
15	48	10.3	10.3

side and one rough, dull side, the roughness giving rise to a measured foil thickness which is systematically about 15% higher than the "calculated" value. On the microscopic scale, the foil has an irregular, randomly oriented grain structure with an average grain size of the order of a micron. The physical properties of the foil which have been investigated display no directional dependence in the plane of the foil, and generally are not systematically dependent on the foil thickness. Numerically these properties can be summarized as follows:-

Yield Stress	=	29.8 ± 0.7 kg mm^{-2}
Ultimate Tensile Stress	=	38.4 ± 0.9 kg mm^{-2}
Coercive Force	=	7.63 ± 0.15 Oe
Maximum Permeability	=	990 ± 50
Resistivity	=	10.37 ± 0.03 $\mu\Omega$cm

If these figures are compared with those in table 1.1 for commercial soft magnetic materials, it can be clearly seen that the electrodeposited iron foil as produced has very little value. In subsequent chapters the possibility of improving the magnetic characteristics of the foil by various heat treatments will be discussed.

CHAPTER THREE

GRAIN GROWTH PROCESSES IN METALS

3.1 Introduction

In Chapter 2 it has been shown that the magnetic properties of the as-produced electrodeposited iron foil are unexciting compared with commercial alternatives. However, means of improving magnetic behaviour do exist, and these relate largely to increasing the mobility of domain walls, a subject mentioned in section 1.6.1. In particular it should be possible to soften the foil magnetically by altering the grain structure by a suitable heat treatment; an increase in grain size and, if possible, the achievement of a degree of grain orientation should both prove advantageous.

In this chapter the subject of grain growth and its study will be discussed. Reference is made in particular to the reviews of Beck (1954) and Christian (1965); other works will be mentioned where applicable.

3.2 Gradual Grain Growth

Gradual, or normal, grain growth is defined as the uniform coarsening of the grain structure of a stress free metal maintained at a high temperature. The driving force for this process is due to the tendency to minimize the surface free energy of the grain boundaries. In order to achieve a reduction in this energy the grain boundaries tend to straighten by migrating towards their centres of curvature and the driving force is proportional to $r_1^{-1} + r_2^{-1}$ where r_1 and r_2 are the two principal radii of curvature in mutually perpendicular

directions of a local section of boundary. Harker and Parker (1945) have shown that approach to equilibrium also requires the migration of grain boundaries so as to minimize the surface tension forces exerted at a grain edge by the three grain boundaries intersecting at it. Smith (1948) showed that the true equilibrium configuration of grain boundaries would only be realized if each grain had the shape of a minimum area tetrakaidecahedron. This situation is most unlikely to be found in any real specimen however, and any deviation from it at any point in a polycrystal must result in continued boundary migration in the whole specimen because of the tendency of the deviation to spread to other areas. Hence true equilibrium in a pure material is not achieved in practice until the whole sample is converted into a single crystal.

If it is assumed that the instantaneous rate of grain growth is proportional to the instantaneous value of the excess grain boundary free energy per unit volume a parabolic relationship for the increase of average grain size with time on isothermal annealing can be derived. This is represented empirically by:

$$D^{1/n} - D_o^{1/n} = Ct \qquad (3.1)$$

where D_o is the average grain diameter before annealing, D is the average grain diameter after annealing, t is the annealing time and C and n are parameters which depend on the temperature but not on D. The instantaneous growth rate is given by:

$$\frac{dD}{dt} = nCD^{1-1/n} \qquad (3.2)$$

Since n is always less than unity, the growth rate decreases with increasing grain size. Theoretically n = 0.5 and good agreement for pure metals has been found by Feltham (1957) and Bolling and Winegard

(1958) whilst Beck, Kremer, Demer and Holzworth (1948) and Burke (1949) have obtained values between 0.056 and 0.6 in cases where the effects of impurities and inclusions are important.

It has already been mentioned that, in principle, grain growth should continue until the whole specimen is a single crystal. However it is usually observed that a limiting grain size is reached after which grain growth virtually ceases. This is due to the presence of inclusions which inhibit grain boundary motion. As the grain size increases during gradual grain growth the driving force for further growth decreases until the inhibiting effect of the inclusions is just sufficient to prevent further growth. The ultimate grain size achieved is stable over long periods of anneal and increases with increasing annealing temperature. The ultimate grain diameter D can be shown (Zener, 1948) to be given approximately by:

$$D = \frac{d}{f} \qquad (3.3)$$

where d is the average diameter of the spherical inclusions and f the volume fraction of inclusions in the specimen.

In sheet materials the ultimate grain size is often found to be close to the sheet thickness. When grains approach the thickness of the sheet, the radius of curvature of the grain faces increases much more rapidly than the average diameter of the grains and when the limiting curvature imposed by equation 3.3 is reached, growth stops. In very thin sheets, however, one might expect some two dimensional growth to occur after the grains have reached sheet thickness size since the grain boundary radii of curvature would still be rather small and the driving force for growth quite large.

3.3 Annealing of Cold Worked Metals

3.3.1 Introduction

When a metal or alloy is deformed at low temperature it becomes strain-hardened due to the increase in the number of dislocations and other imperfections which impede dislocation motion. Mechanical and many other physical properties are measurably changed by the cold working, but can be induced to return to their original values by heat treatment. If this is achieved without changing the original grain structure of the metal the process is known as recovery, but at higher temperatures most metals undergo a discontinuous change in grain structure known as recrystallization in which new strain-free grains consume the deformed structure. Primary recrystallization is followed by normal grain growth or in certain circumstances by a highly selective grain growth known as secondary recrystallization, but the change in most physical properties is virtually complete by the end of primary recrystallization.

Titchener and Bever (1958) have shown that between 1 and 15% of the energy expended in deforming the metal is stored, by means of increased dislocation and defect densities, in the metal and this energy provides the driving force for recovery and primary recrystallization. The remaining energy of cold work is dissipated as heat.

The precise details of recovery and recrystallization processes vary dramatically from metal to metal and are dependent on a large number of parameters, but a few general observations will be covered in the following sections.

3.3.2 Recovery

As mentioned above, recovery is the process by which the mechanical and physical properties of a cold worked metal can be restored to something like their original values without altering the grain structure of the metal. Structural changes do take place within the grains themselves however, the original deformed grains breaking up into a number of smaller sub-grains of almost identical orientation leaving the original grain boundaries undisturbed. This process is known as polygonisation after the early work of Cahn (1949) who studied the effects of annealing bent zinc crystals. The driving force for the formation of a polygonised structure arises from the strain energy of the dislocations trapped in the material by the deformation process. These dislocations can reduce their energy either by mutual annihilation of opposite dislocations or by assembly of dislocations into more or less regular arrays which form the boundaries of the sub-grains. The sub-grains themselves are consequently relatively defect free, which accounts for the recovery of physical properties resulting from polygonization. The misorientation at the sub-boundaries has been observed to vary from a few minutes to several degrees. Once a reasonably perfect polygonised structure has been formed, the strain energy is stored by the dislocations in the sub-boundaries, and this surface energy can lead to sub-grain growth in a manner which is exactly analogous to normal grain growth.

Polygonization can take place at temperatures well below those required for recrystallization; indeed in the case of aluminium, polygonized structures form during the deformation (Kellar et al, 1950 and Hirsch et al, 1957). Lightly worked specimens may be induced to polygonize into a structure which is sufficiently stable that no recrystallization

takes place at higher temperatures. Conversely a very heavily worked metal may recrystallize without detectable prior polygonization. Impurities appear to inhibit polygonization and to reduce the rate of sub-grain growth.

3.3.3 Primary Recrystallization

Primary recrystallization is the process by which a cold worked metal or alloy undergoes a complete change in grain structure, with new strain-free grains growing into the deformed matrix until the latter is completely consumed. The driving force for the process is a consequence of the stored energy of cold work introduced by the deformation. For deformation at room temperature the proportion of the stored energy removed by recovery processes prior to recrystallization varies from 0% for high purity copper to 70% for commercial purity nickel. However it is well established that some of the original stored energy is necessary to effect recrystallization and this remaining energy is then removed in proportion to the volume of the material that has recrystallized.

Experiments on the kinetics of primary recrystallization have shown that the volume percentage transformed as a function of annealing time follows a sigmoidal relationship, as shown in figure 3.1, in which the reaction rate is at first very low, then increases to a maximum before finally decreasing again. Such a process can be described in terms of two simultaneous processes, namely the nucleation of new grains and their subsequent growth. A certain incubation period is observed before the first new grain appears. Stanley and Mehl (1942) and Anderson and Mehl (1945) have used a statistical metallographic

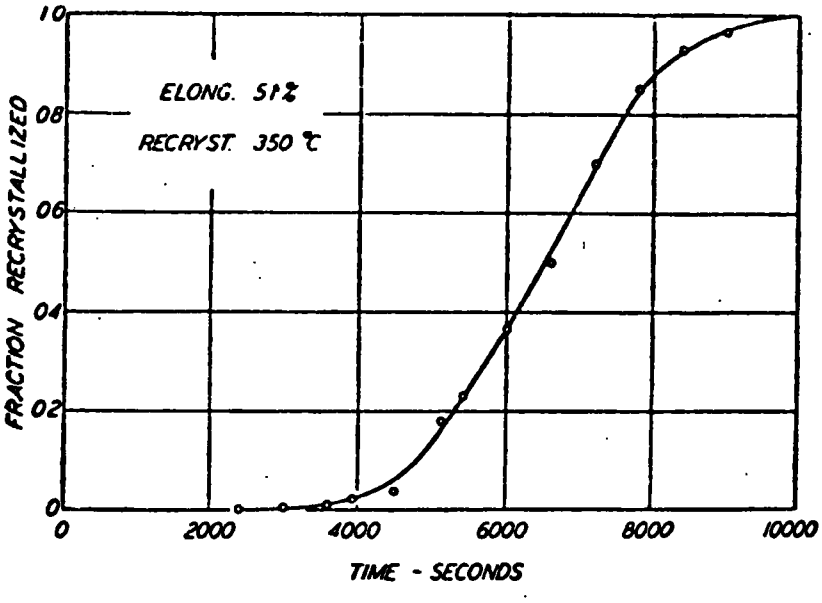

Figure 3.1 Isothermal recrystallization curve for pure Al at 350°C after a 5.1% extension (after Anderson and Mehl, 1945).

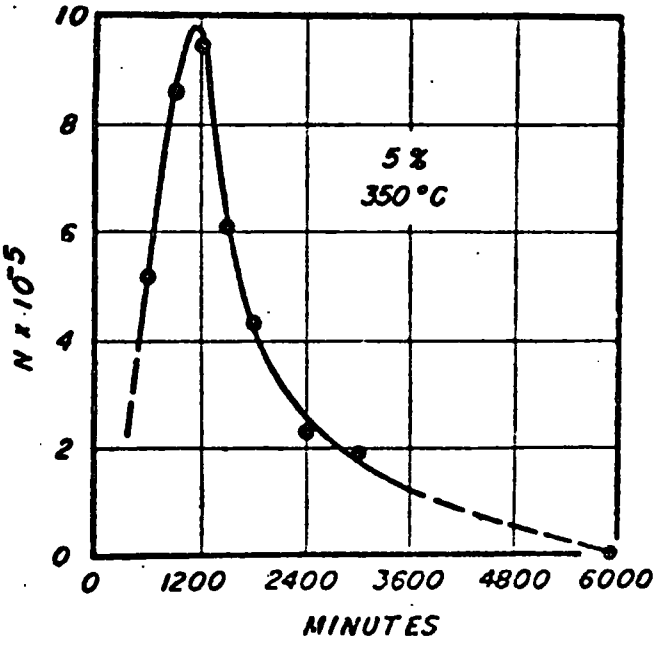

Figure 3.2 Rate of nucleation as a function of annealing time at 350°C after a 5% extension (after Anderson and Mehl, 1945).

technique to study recrystallization kinetics and found that the diameter of the largest recrystallized grain increased linearly with time. The rate of nucleation, that is the rate of increase of the number of recrystallized grains per unit of untransformed volume, was found typically to be represented by a curve such as figure 3.2.

The kinetics of recrystallization are critically dependent on a large number of external variables, in particular temperature, amount of strain, material purity and the orientation difference between a recrystallized grain and the deformed matrix into which it is growing. A minimum deformation is required before recrystallization can take place, while the grain size of the recrystallized product decreases with increasing strain. The temperature at which the recrystallization rate becomes appreciable and the time taken to complete the recrystallization process both decrease with increasing deformation. Impurities usually reduce the recrystallization rate by inhibiting grain boundary motion, whilst boundary mobility generally increases with increasing orientation difference between the growing grain and its surroundings.

3.3.4 Nucleation in Primary Recrystallization

Although the growth of new grains after a period of incubation is readily observed by metallographic means, the origin of the nuclei of these grains is not certain and indeed different theories may be applicable in various circumstances. It is certain that a strain-free nucleus must be above a critical size if it is to be capable of growth into a deformed matrix. At the critical size, for a small amount of growth the free energy gained from the additional volume transformed is just sufficient to compensate for the free energy required to

increase the interface area.

In Cahn's theory (1950) essentially strain-free regions of very small size form by polygonization during the early stages of annealing. This thermally activated dislocation rearrangement is not strictly a nucleation process and the apparent incubation period corresponds to an initial stage of very slow growth. This latter phenomenon has been explained by Cottrell (1953) as follows. The initial boundary between a growing region and its surroundings will be a low angle type and consequently relatively immobile, but as the nucleus grows into matrix material of strongly differing orientation a boundary of much greater mobility is formed.

An alternative model for nucleation is based on the observations of Beck and Sperry (1950) and Bailey (1960) that recrystallization can start from high angle grain boundaries present in the sample before deformation. This "strain induced boundary migration" model requires a local difference in dislocation density across the two sides of a grain boundary, causing the boundary to bulge out into a spherical cap creating a dislocation-free region. The rate of increase of linear dimensions of the growing grain is calculated to be a minimum when the grain is hemispherical (Bailey and Hirsch, 1962) which can lead to the apparent incubation period observed experimentally.

Both models appear to have areas of applicability. The strain induced boundary migration mechanism is apparently prevalent at low to medium deformations and certainly requires a polycrystalline matrix. The Cahn-Cottrell model predominates in single crystals or severely deformed polycrystals in which most of the recrystallized grains

originate within the deformed grains. Neither theory is strictly a nucleation and growth process, though the operational definition of the nucleation rate remains valid.

3.3.5 Secondary Recrystallization

If a metal is maintained at a high temperature after the completion of primary recrystallization, the average grain size continues to increase by one of two processes. The more common mechanism is that of gradual grain growth, which has already been covered in section 3.2 but under certain circumstances a highly selective growth of only a few grains, known as secondary recrystallization or coarsening, can occur. The favoured grains attain a size which is very much greater than that of the surrounding matrix and eventually consume it altogether. Secondary recrystallization displays the same apparent nucleation and growth characteristics as primary recrystallization, but the driving force for the reaction is rather different, being the tendency to reduce the grain boundary surface energy as in gradual grain growth. Secondary recrystallization is only observed in materials in sheet form. In order for complete secondary recrystallization to occur, the primary recrystallized grains must remain small relative to the larger grains which consume them. Inhibition of normal grain growth may be achieved either by the existence of a strong primary recrystallization texture in which case all the grain boundaries are of the low angle type and consequently of low mobility, or by the presence of dispersed second phase inclusions which inhibit grain boundary motion.

A stable growing nucleus must be large enough so that the surface energy gained by shortening the interfaces between the matrix grains

adjoining the nucleus must be at least equal to the surface energy lost by the corresponding extension of the nucleus-matrix interface. In general the nucleus for secondary recrystallization is a grain already present in the matrix after primary recrystallization selected for growth by virtue of its large size, its orientation and the relatively weak inhibition at its boundaries. The observed incubation period in secondary recrystallization corresponds to an initial period of slow growth and, in the case of inhibition dependent coarsening, may also be affected by the rate of re-solution and coalescence of the dispersed inhibiting particles.

3.4 Grain Orientation

3.4.1 Introduction

The superior properties of single crystals of most ferromagnetic materials along particular crystallographic directions suggests the production of useful polycrystalline materials by control of the crystallographic texture. The texture of a polycrystalline material is the distribution of the orientations of the crystal axes of the individual grains with respect to some reference directions. A non random texture is known as a preferred orientation. In the case of a sheet material the texture is specified with respect to the plane and edges of the sheet. The usual notation is to specify first the crystallographic plane which lies parallel to the plane of the sheet, followed by the crystallographic axis which lies parallel to the rolling direction. The subject of textured magnetic materials is reviewed generally by Graham (1969) whilst Littmann (1971) discusses iron and silicon-iron textures in particular.

3.4.2 Sources of Texture

Three of the most important sources of texture in metals are solidification, deformation and annealing after deformation.

Formation of texture by solidification is achieved by pouring the molten metal into a mould with a cold bottom and insulated side walls so that solidification begins at the bottom and proceeds upwards through the metal. Columnar grains result which in the case of cubic metals have a ⟨100⟩ direction or cube edge parallel to the column axis. This technique is particularly useful in forming Alnico permanent magnets which are brittle and incapable of being cold rolled and recrystallized.

Deformation textures result when a polycrystalline material is plastically deformed, but cold worked metals are of no use for magnetic applications and deformation textures only have value as a step towards an annealing texture.

Annealing textures occur when a deformed material with a non random texture is heated so that it undergoes primary recrystallization. The annealing texture is usually different from and sometimes sharper than the deformation texture. Secondary recrystallization can result in a different and often much sharper texture. Face centred cubic nickel-iron alloys develop a sharp (100) [001] or cube primary recrystallization texture when annealed after severe cold working of about 95%. Further annealing gives secondary recrystallization to a less sharp (120) [001] texture.

3.4.3 Grain-oriented Silicon-iron

Oriented silicon-iron alloys are the most important textured magnetic materials in terms of volume and value of material used. The benefit of preferred orientation is derived from the superior magnetic properties of iron along the ⟨100⟩ direction. The addition of silicon, apart from improving various physical and magnetic properties as outlined in section 1.6.4, eliminates the face centred cubic γ phase for compositions with greater than about 2.2% silicon, allowing high temperature heat treatments to develop texture. Two textures are commonly produced; these are the Goss or cube-on-edge (110)[001] texture and the cube (100)[001] texture which are illustrated schematically in figure 3.3.

The first successful process for making oriented silicon-iron sheet was that of Goss (1934) who produced the (110)[001] texture by a process involving two stages of cold rolling with an intermediate anneal at 800-900°C in a reducing atmosphere and a final anneal at 1100°C in a non oxidising atmosphere. The process has been modified over the years to improve the degree of orientation but the (110)[001] texture can be produced under a fairly wide range of conditions. Metallurgically the texture arises due to secondary recrystallization with impurity inhibition of gradual grain growth. Both manganese and sulphur were present as incidental impurities when Goss made his breakthrough, and May and Turnbull (1957) showed the importance of MnS particles in develcping the texture. Other second phase inclusions have a similar effect to MnS, nearly all of which involve carbon, oxygen, sulphur or nitrogen. These elements must be eliminated from the final product as they contribute to high hysteresis loss.

a)

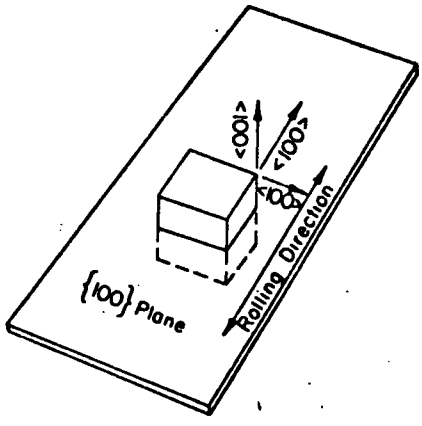

b)

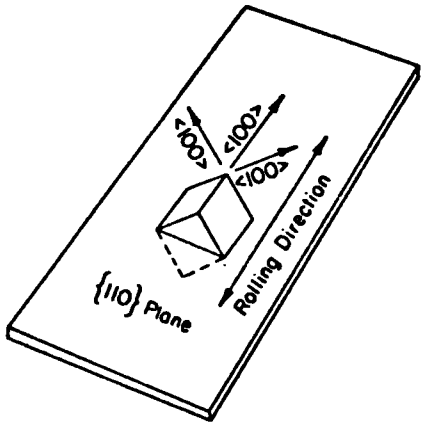

Figure 3.3 Schematic representation of the a) (100)[001] and b) (110)[001] textures (after Graham, 1969).

Goss textured silicon-iron shows excellent magnetic properties in the rolling direction but much inferior properties in other directions in the plane of the sheet. For applications such as U-shaped transformer laminations a sheet material with good magnetic properties both parallel and perpendicular to the rolling direction is desirable and led to the development of the cube (100) [001] texture with easy directions in both these directions. The production of silicon-iron with (100) planes in the plane of the sheet can be achieved by secondary recrystallization under conditions in which grains with (100) planes parallel to the sheet surface have lowest energy. The surface energy mechanism is especially effective in thin sheets, for which the surface area to volume ratio is high, and can be applied to the production of tapes for magnetic amplifier use. Taguchi et al (1964) have produced cube textured silicon-iron after cross cold rolling using aluminium nitride inhibitors.

The properties of Goss and cube textured silicon-iron in the rolling direction are comparable. Perpendicular to the rolling direction cube textured material is vastly superior to the Goss texture, though slightly inferior to its own properties in the rolling direction. However the advantages at the cube texture have generally proved insufficient to offset the higher production costs.

3.5 Observation Techniques

The direct observation of the kinetics of grain growth and recrystallization processes is complicated by the hostile environments normally required to bring about the structural changes to be studied. In general optical techniques are ruled out because of the high temperatures involved, although Tardy and Iskander (1969) have observed

directly by optical micrography the recrystallization of lead at room temperature. The slight etching action of a continuously circulating electropolish was used to reveal the positions of the moving grain boundaries. This technique, however, is limited to low melting point metals which can be induced to recrystallize around room temperature.

In general high temperature processes are studied by statistical metallographic techniques, such as that employed by Stanley and Mehl (1942) to study the recrystallization kinetics of silicon-iron. Large numbers of equivalent samples were annealed for different periods of time and the proportion of material recrystallized at each stage was determined planimetrically. The same sample cannot be used throughout the experiment because the etching process necessary to reveal the grain boundaries can impede their subsequent motion. This technique is clearly extremely tedious, though it has been improved slightly by Decker and Harker (1950) and Seymour and Harker (1950) who used an X-ray diffraction method to estimate the fraction of material recrystallized. This technique relies upon the fact that certain Bragg reflections have markedly different intensities for cold worked and recrystallized material, but still requires the use of a large number of samples heated for different times.

Evidently there is considerable scope for the development of a technique for the direct observation of the kinetics of grain growth and recrystallization processes at high temperatures, and the possibility of using synchrotron radiation in pursuing this aim will be examined in Chapter 4.

CHAPTER FOUR

APPLICATION OF X-RAY SYNCHROTRON TOPOGRAPHY TO STUDIES OF POLYCRYSTALLINE METAL SHEETS

4.1 X-Ray Diffraction Topography

4.1.1 Introduction

X-Ray diffraction topography is concerned with techniques by which a topographical display of the microstructural defects in a crystal can be obtained. Simply considered, contrast is obtained by the point to point variations in the directions or the intensities of x-rays that have been diffracted by a crystal. If the Bragg condition is satisfied for radiation of wavelength λ incident at an angle θ to the Bragg planes of spacing d, strong diffraction occurs where

$$n\lambda = 2d \sin\theta \qquad (4.1)$$

If part of the crystal is locally distorted or misoriented, the Bragg condition is not satisfied for the deformed region and a local variation in the intensity of the diffracted beam is observed. Details of the mechanisms of contrast are covered in the book (1976) and review article (1977) of Tanner.

4.1.2 Conventional Techniques

A few techniques for obtaining x-ray diffraction topographs using conventional laboratory x-ray generators will be outlined in this section. The methods divide into those using characteristic and those using continuous x-radiation.

Characteristic radiation methods include the Berg-Barrett and Lang

techniques. In the method originating from the work of Berg (1931) and Barrett (1945), illustrated schematically in figure 4.1(a), a single crystal is set to Bragg reflect the characteristic radiation from a chosen set of lattice planes using an extended source. A doubling of the image of any defect occurs because of the different angles of diffraction of the $K\alpha_1$ and $K\alpha_2$ lines, but this can be rendered negligible by placing the photographic recording plate close to the crystal.

The Lang (1958, 1959) method is the most commonly used topographic technique and is illustrated in figure 4.1(b). The beam from a fine focus generator is highly collimated so that only the $K\alpha_1$ line is diffracted by the chosen lattice planes of the crystal. The whole specimen is viewed by traversing the crystal and film together across the ribbon x-ray beam. Geometrical resolution approaching 1 micron can be achieved by placing the film within about 1 cm of the crystal.

Continuous radiation techniques have the advantage that the crystal does not need to be set to a precise angle to obtain Bragg reflection, since each set of lattice planes selects its own wavelength to satisfy the diffraction condition. Schulz (1954) used the reflection mode with a microfocus tube source, whilst the equivalent transmission technique was developed by Guinier and Tennevin (1949). The two techniques are illustrated schematically in figure 4.2.

In the continuous radiation techniques the beam at the specimen is sufficiently large for the entire sample to be imaged. Because the radiation is white the Bragg condition can be satisfied simultaneously

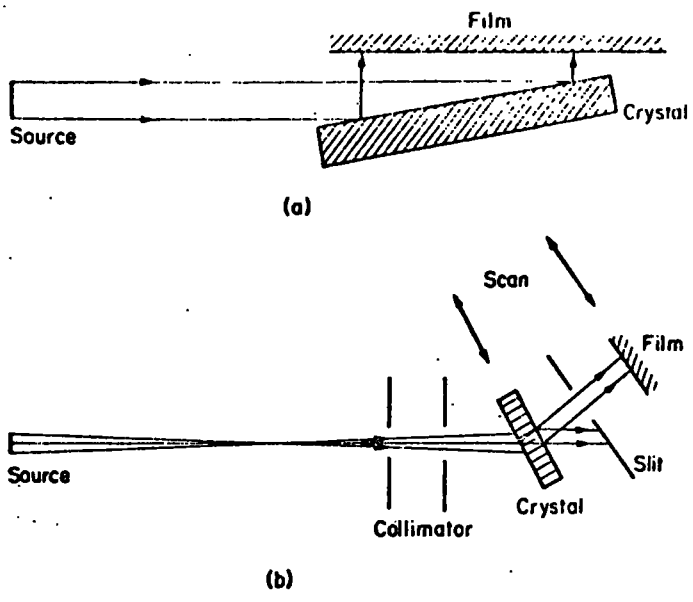

Figure 4.1 Experimental arrangement for the a) Berg-Barrett and b) Lang techniques (after Tanner, 1977).

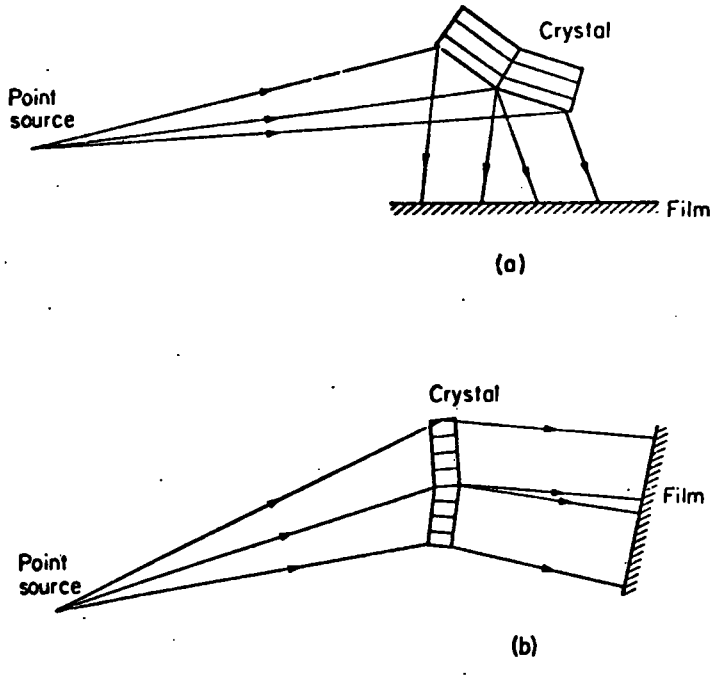

Figure 4.2 Experimental arrangement for the a) Schulz and b) Guinier and Tennevin techniques (after Tanner, 1977).

for several sets of lattice planes, each of which selects its own diffracting wavelength, and several images of the crystal are obtained just as in Laue pictures. In addition, bent crystals can be imaged, with the continuously varying Bragg condition being satisfied by different wavelengths. To achieve reasonable geometrical resolution in the laboratory, long exposure times are necessary, but in recent years continuous radiation topography has been advanced dramatically by the use of synchrotron radiation.

4.2 Synchrotron Radiation

An electron constrained in a circular orbit by a magnetic field in a synchrotron or storage ring emits electromagnetic radiation. The total power radiated is proportional to the fourth power of the electron energy (E), the electron current (I) and the inverse of the orbital radius (R). At relativistic electron velocities the radiation is emitted in the laboratory frame as a narrow cone (figure 4.3) whose angular divergence (ψ) is given at short wavelengths by

$$\psi \simeq \frac{m_o c^2}{E} \qquad (4.2)$$

where m_o is the electron rest mass. The beam is totally polarized in the orbit plane for radiation emitted along the tangent to the orbit and highly elliptically polarized otherwise.

The radiating electrons differ slightly in velocity due to betatron and synchrotron oscillations and their differing harmonic frequencies blur into a continuous spectrum extending through the visible and ultraviolet to the x-ray region. The spectral distribution can be characterized (Tomboulian and Hartman, 1956) by the critical wavelength

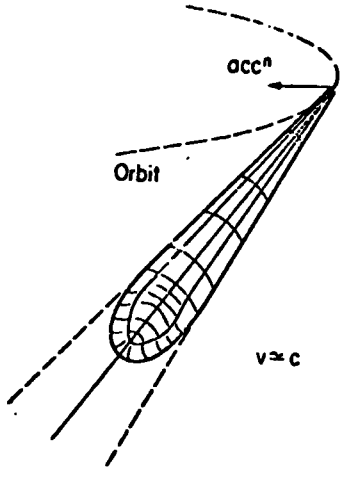

Figure 4.3 Synchrotron radiation cone (after Tanner,1977).

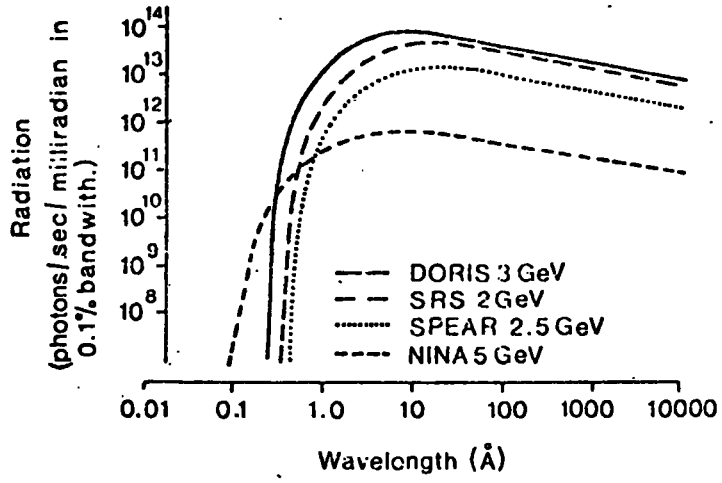

Spectral output from various synchrotron radiation sources. The photon flux figures refer to a one mrad "fan" in the orbital plane, after integration over all azimuthal angles. The assumed operating parameters for the accelerators, and their corresponding critical wavelengths, are as follows:

DORIS storage ring (Hamburg, Germany)	3 GeV, 1 A, 2.5 Å
SRS storage ring (Daresbury, U.K.)	2 GeV, 1 A, 3.9 Å
SPEAR storage ring (Stanford, U.S.A.)	2.5 GeV, 250 mA, 4.6 Å
NINA synchrotron (Daresbury, U.K.)	5 GeV, 20 mA, 0.93 Å.

(The NINA synchrotron was closed down on 1 April 1977, and is no longer available.)

Figure 4.4 (after Lea,1978).

(λ_c) defined as

$$\lambda_c = \frac{4\pi R}{3} \left[\frac{m_o c^2}{E}\right]^3 \qquad (4.3)$$

The intensity distribution peaks at $0.42\lambda_c$ and at shorter wavelengths the intensity falls rapidly so that λ_c is important in determining whether a machine will be useful for x-ray physics. Figure 4.4 shows the radiation spectra for various synchrotron radiation sources. The experiments reported in this chapter were performed using the synchrotron NINA at Daresbury Laboratory. When operated at an electron energy of 5 GeV, NINA had a critical wavelength of 0.93 Å and an angular divergence of about 10^{-4} radians. The intensity of synchrotron radiation is typically of the order of 10^3 times higher than that from conventional x-ray sources.

4.3 Synchrotron X-Ray Topography

Because of radiation hazards the experimental area at Daresbury Laboratory is situated some 50 m from the electron orbit, the synchrotron beam propagating along an evacuated beam pipe and emerging through a Be window. At the experimental end of the pipe lead slits allow an intense, highly parallel beam of continuous radiation about 1 cm square into the area. X-ray topography using the Schulz or Guinier and Tennevin techniques can be performed with the synchrotron x-radiation. When the synchrotron beam is incident on a crystal each set of lattice planes selects its own wavelength to satisfy the Bragg condition and a pattern of Laue spots is obtained. Because the beam is large enough to cover the entire area of the crystal, each Laue spot is an image of the crystal, revealing as much information as a conventional Lang topograph. The best resolution obtainable for this

technique can be easily estimated with the knowledge that the NINA effective source size is about 0.5 mm square. The resolution in both horizontal and vertical directions is given by

$$r = x \frac{D}{L} \qquad (4.4)$$

where D is the source dimension, L the source to specimen distance and x the specimen to film separation which is typically 5 to 10 cm. Substitution yields a best geometrical resolution of 0.5 to 1 microns. Hart (1975) and Tanner et al (1977a), working under optimum conditions, have achieved experimental resolutions approaching this figure.

Streaking of images is a common feature of synchrotron x-ray topographs. In a bent lattice, the Bragg angle varies continuously but all Bragg relations can be satisfied because of the continuous nature of the radiation. The image appears to be spread out across the film, perpendicular to the Bragg planes. The amount of lattice curvature can be estimated from the length of the streak and the specimen to film distance.

Synchrotron radiation has several advantages over conventional techniques in the field of x-ray diffraction topography, the most important of which can be summarized as follows:

1. The very high intensity of the radiation leads to a reduction in exposure time of 2 to 3 orders of magnitude.

2. A resolution of 1 to 2 microns can be obtained for relatively large specimen to film separations of 10 to 20 cm.

3 No critical adjustments are necessary and large amounts of space are available round the specimen.

4 The continuous nature of the radiation allows images to be obtained from bent crystals.

4.4 Study of Time Dependent Microstructural Changes using X-Ray Diffraction Topography

The study of dynamic physical processes is of great interest, and in many cases x-rays prove to be the best way of imaging the particular changing characteristic under study. For instance x-ray diffraction topography is well established as a technique for observing crystal defects and dislocations, and Nøst and Sørensen (1966) and Baudelet and Champier (1973) have observed directly changes in dislocation densities in aluminium single crystals during thermal treatments up to 400°C by building simple resistance furnaces onto Lang cameras.

However the rather stringent geometrical requirements of conventional techniques limit the amount of apparatus which can be incorporated into the experiment. The changes to be studied often require very high or low temperatures or large magnetic fields, all of which involve bulky equipment. The advantages of synchrotron radiation outlined in the previous section have made it a very powerful tool in the study of time dependent changes at the microstructural level. Step-by-step experiments can be performed successfully under conditions which would be impossible with conventional techniques.

Bordas et al (1975) have studied the phase transition in barium titanate

at about 130°C; here the intensity of the synchrotron radiation reduced exposure times to 15 to 30 seconds, obviating the need for elaborate temperature control.

Step-by-step domain wall motion in $KNiF_3$ was observed by Tanner et al (1976) and Safa and Tanner (1977, 1978) using a large electromagnet which could not possibly have been incorporated into a conventional Lang camera.

Furthermore Tanner et al (1977b) have demonstrated that there is sufficient intensity to allow the x-ray beam to pass through 8 mm of glass cryostat without unacceptable increase in exposure time, so that synchrotron radiation clearly has the potential to allow the study of dynamical microstructural physical processes in hostile environments. It is this realization which prompted the successful attempt to study the recrystallization kinetics of silicon-iron at about 1000°C which will be described in a following section.

4.5 Synchrotron Topography of Polycrystals

Guinier and Tennevin (1949), using a laboratory point source of white x-radiation, produced topographs of polycrystalline aluminium and iron. Each grain of the polycrystal produced a Laue pattern of spots, each corresponding to the dimensions of the grain. The relative geometrical dimensions and positions of the images yielded information on the size and orientation of the grains. Steinberger et al (1977) have studied the microstructure of vapour grown ZnS polytypes using synchrotron radiation and observed structural changes on heating to 250°C.

Using the Synchrotron Radiation Facility at Daresbury Laboratory it has been demonstrated (MacCormack and Tanner, 1978) that the grain size, perfection and orientation of polycrystalline sheets can be rapidly assessed using synchrotron radiation. For transmission work the beam passes normally through the specimen and a film placed about 10 cm behind the sample records the Laue topographs for all grains covered by the beam area.

Figure 4.5(a) shows an example of the images obtained from a commercial sheet of silicon-iron. The dimensions of each image, corrected for the geometrical image distortion, correspond directly to the grain size and different reflections from the same grain can be identified. In this example the boundaries of the images are quite sharp, indicating a discrete, mosaic block structure with little strain within each grain. There is however a large spread in orientation of the grains.

Figure 4.5(b) shows a similar synchrotron Laue topograph of a sheet of iron foil whose average grain size was determined microscopically to be about 50 microns. Again there is a large orientation spread, and in addition a degree of strain is seen to be associated with the material, as evidenced by the streaking of some images normal to the Bragg planes. In both the above cases, the electron beam energy and current were 4 GeV and 15 mA respectively and the topographs were recorded on 10 micron thick Ilford L4 nuclear emulsion with exposure times of 14 minutes.

Two more topographs of different commercial silicon-iron sheet material are included for comparison (figure 4.5(c) and (d)). Both were recorded

a)

1 cm

b)

Figure 4.5 Synchrotron topographs of a) commercial silicon-iron and b) iron foil annealed for 2 hours at 900°C.

c)

1 cm

d)

Figure 4.5 c) and d) Synchrotron topographs of commercial silicon-iron sheet material.

on Polaroid 4 x 5 Land Film Type 52. Figure 4.5(c) shows a fairly large grained, well oriented sheet and was recorded with a beam power of 4 GeV and 22 mA and an exposure time of 90 seconds. The sheet yielding the topograph shown in figure 4.5(d) has a rather smaller, more randomly oriented grain structure and was recorded with a beam power of 5 GeV and 12 mA and an exposure time of 8 seconds.

4.6 Application of X-Ray Synchrotron Topography to in-situ studies of Recrystallization

4.6.1 Introduction

In Chapter 3 the desirability of a direct means of observing the kinetics of the recrystallization process at high temperatures was mentioned, and in this section the preliminary studies of the application of synchrotron x-radiation to this problem are reported. It has been shown in section 4.5 that the individual grains of a polycrystalline sheet can be imaged using synchrotron radiation, so it should be possible with the design of suitable apparatus to observe the growth of such grains during recrystallization from a cold worked sheet.

4.6.2 Apparatus and Experimental Technique

The material studied in the recrystallization experiment was a commercial silicon-iron sheet containing 3.5% silicon. The sheet had previously been cold rolled so that its thickness had been reduced by 85% to a final value of 370 microns. As with the studies of polycrystalline sheet at room temperature, we require that the synchrotron beam passes normally through the sheet, and that the diffracted beam can be recorded on a suitable film placed within about 20 cm of the sample. The problems to be overcome in the recrystallization experiment are the incorporation of a suitable furnace to heat the sheet to temperatures

around 1000°C and the containment of the sheet in an inert atmosphere to prevent oxidation.

The apparatus used in the experiment is shown schematically in figure 4.6. The sample of silicon-iron, 2.5 x 2 cm^2 in superficial area, was cut from the cold rolled sheet and supported in a vertical plane by a simple holder fashioned from graphite. The holder was pushed inside a cylindrical alumina tube 4 cm in diameter and 1 m long which in turn was supported inside a resistance heated furnace. A platinum/platinum - 13% rhodium thermocouple linked to a Eurotherm temperature controller allowed the temperature of the specimen to be maintained at about 1000°C. A brass fitting sealed to the cold end of the alumina tube with a rubber 'O' ring allowed the tube to be evacuated by a rotary pump and filled with high purity argon, the procedure being repeated 5 times to reduce the level of residual oxygen to minimal proportions.

The synchrotron radiation beam entered the alumina tube at the cold end through a mylar window in the brass fitting and passed along the length of the tube to strike the silicon-iron sheet normally. Diffracted beams passed through the hemispherical closed end wall of the alumina tube and were recorded on Polaroid 4 x 5 Land Film Type 52 situated 20 cm from the sample. Considerable heat was radiated from the hot end of the furnace, so the film was cooled with a stream of cold air. The alumina produced a halo around the direct beam but images of individual grains were not observed.

A little care was necessary in arranging the furnace geometry so that the angle of divergence of the emerging x-ray beams was sufficient to

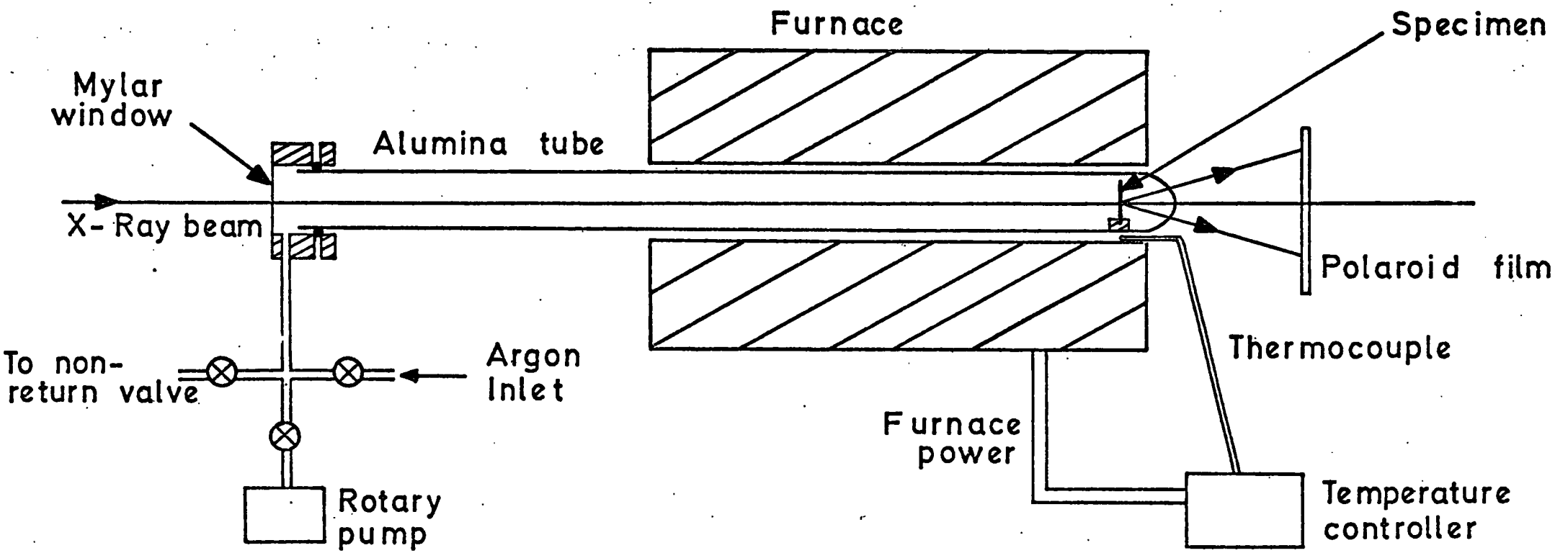

Figure 4.6 Apparatus used in recrystallization experiment.

enable a reasonable fraction of the Laue pattern to be recorded. Once the furnace had reached 1000°C, after about 100 minutes, micrographs were taken sequentially. The electron beam energy and current were 5 GeV and 7 mA respectively and exposure times of 30 seconds were found to be adequate. However, because of the beam area search procedure in operation at the Daresbury Laboratory a total interval of 2 minutes between each data point was unavoidable.

4.6.3 Results

No diffraction pattern was obtained from the sample initially, because of the large amount of deformation introduced by the cold rolling. In run 1, 31 minutes elapsed after reaching 1000°C before any recrystallized grains appeared on the film, and the grains then continued to grow for a further 18 minutes until they had all impinged on one another and recrystallization ceased. Figure 4.7 shows a sequence of micrographs of the growing grains. It can be seen that the incubation period for all the grains covered by the beam area was very similar, all grains appearing between 31 and 33 minutes after reaching 1000°C. There is very little strain associated with the recrystallized grains at any stage during their growth, and the recrystallized grains are large and display a small orientation spread around a preferred direction.

Images of several grains can easily be identified throughout the sequence, though there is a tendency for the images to overlap as the grains approach their ultimate size. This problem would not occur of course in a more randomly oriented array of grains. However the areas of five separate grains were measured throughout the sequence and the

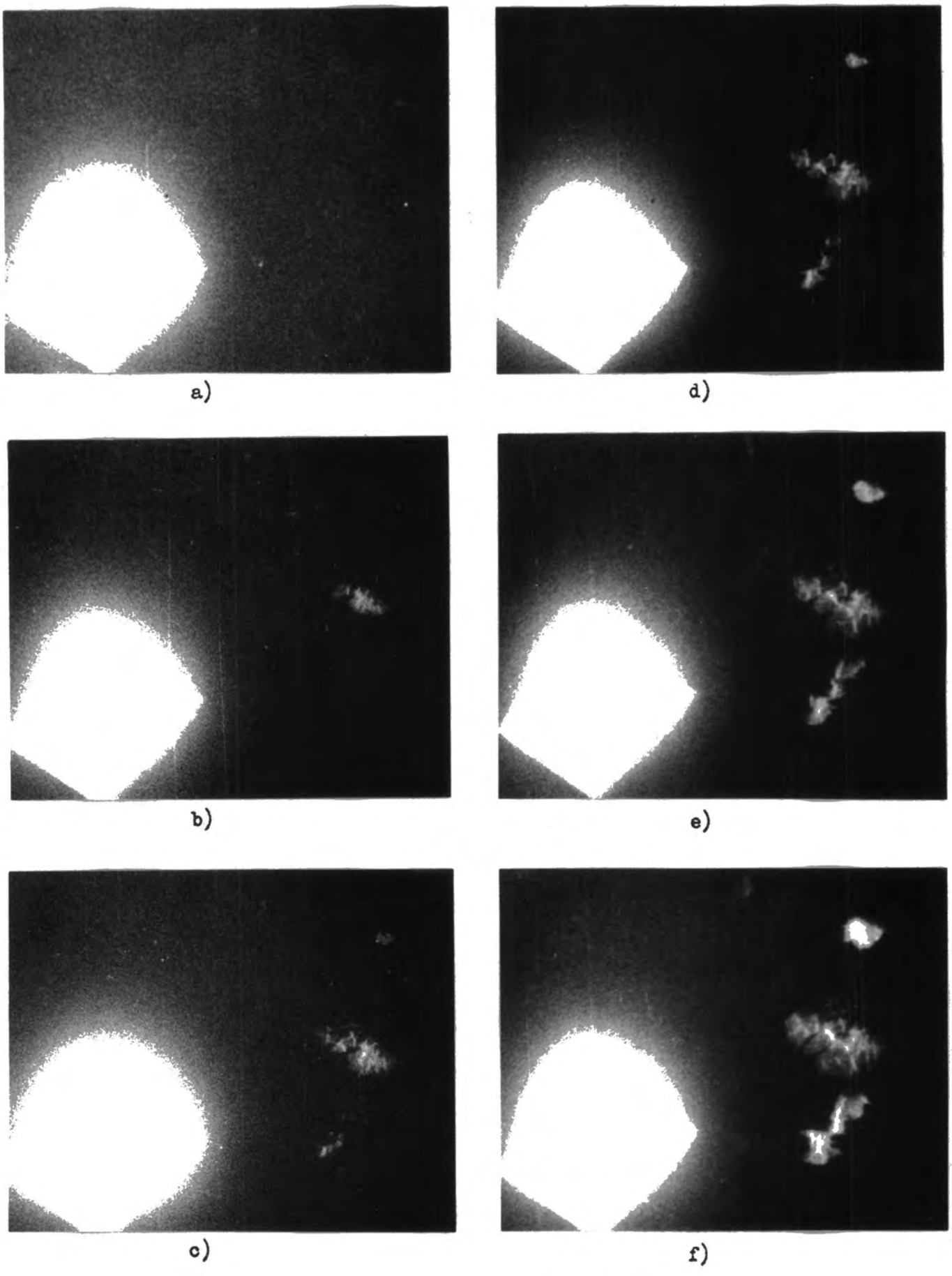

Figure 4.7 Sequence of silicon-iron recrystallization topographs after a) 25 b) 31 c) 33 d) 35 e) 37 f) 39 g) 41 h) 43 i) 45 j) 47 and k) 49 minutes at 1000°C.

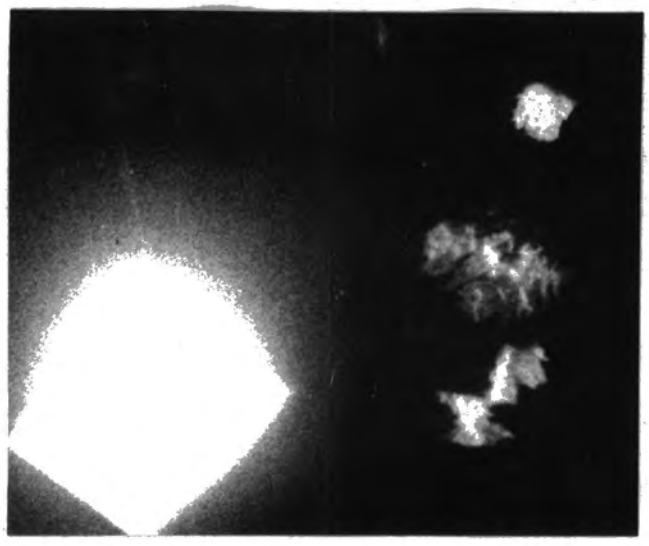

g)

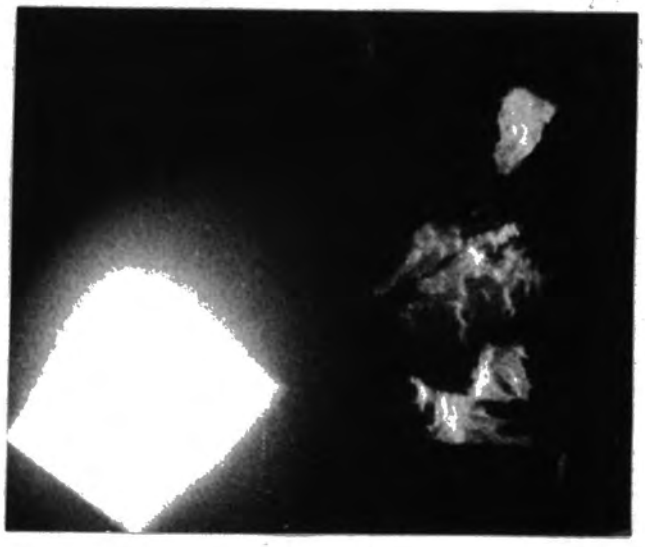

j)

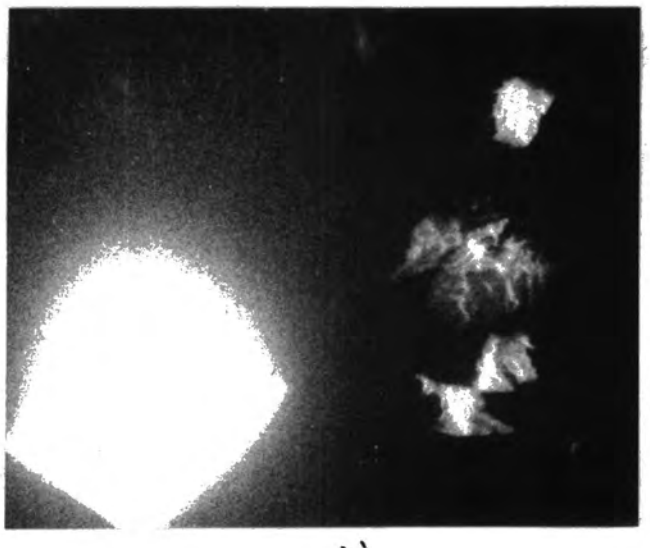

h)

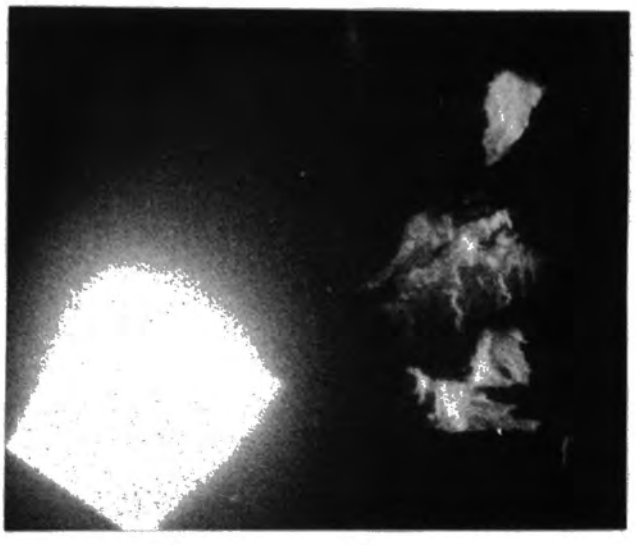

k)

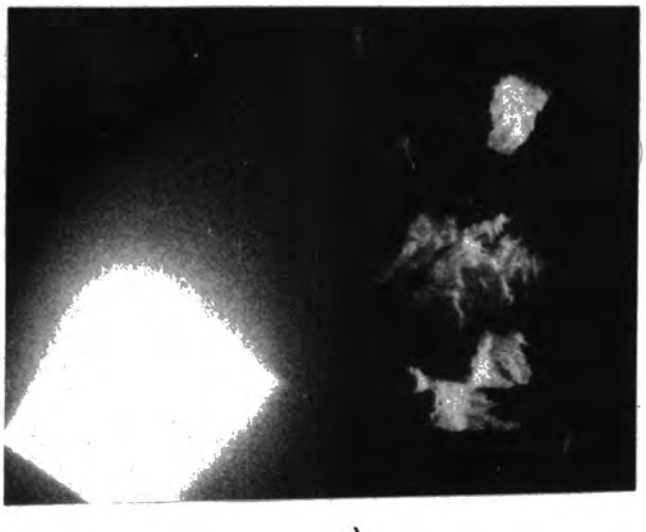

i)

1 cm

square root of the grain area, a useful parameter related to the grain linear dimensions, is plotted as a function of time in figure 4.8.

At small grain sizes, the rate of radial growth is approximately constant and nearly equal for all five grains. The general shape of the curve is very similar to that obtained for Fe - 1% Si by Stanley and Mehl (1942). The average value for the rate of change of grain diameter was measured as 5.5 ± 0.3 micron sec^{-1} which is in good agreement with the value of 5.8 micron sec^{-1} reported by Spychal (1977) for similar material at $1000^{o}C$, using a standard metallographic statistical technique. The average final grain area is 15 ± 2 mm^2.

Unfortunately with the fairly unsophisticated apparatus used, it was impossible to reproduce the results of the experiment on successive runs. In run 2, at the same nominal temperature of $1000^{o}C$, the recrystallization commenced almost immediately after reaching the maximum temperature and was complete after only 8 minutes. The recrystallized grains were smaller, with an average area of 10 ± 4 mm^2 and rather more widely distributed in orientation. It is assumed that the temperature in this run was somewhat higher than in the first. It was found that a temperature gradient of $5^{o}C$ mm^{-1} existed at the position of the sample and hence small changes in the location of sample and thermocouple could have resulted in a significant temperature difference.

It is interesting at this stage to consider the contrast within the individual grain images. Gastaldi et al (Miltat, 1978) have observed the growth of large recrystallized grains in polycrystalline aluminium annealed at $350^{o}C$ using synchrotron radiation, and were able to observe

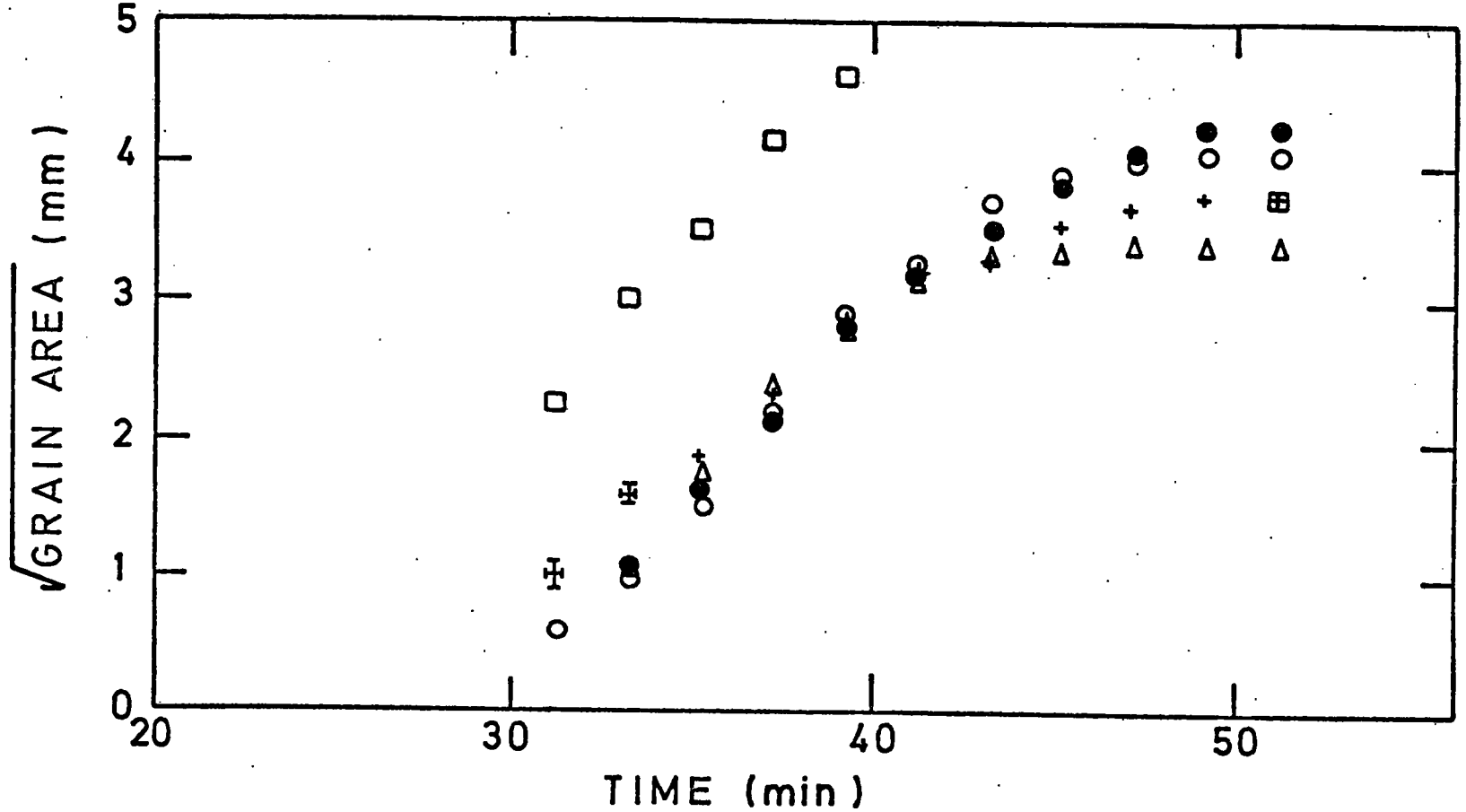

Figure 4.8 Kinetics of silicon-iron recrystallization experiment.

the generation of individual dislocations during the growth process. In the present experiment Polaroid film was used as the recording medium because of its greater resistance to the radiated heat and the shorter exposure times permissible and this does not have sufficient resolution to allow imaging of individual defects. However the wavy contrast seen on the Polaroids is very similar to that appearing on the Ilford L4 nuclear emulsions (figure 4.5(a)) which were obtained at room temperature from a commercial silicon-iron sheet. Individual defects could not be resolved in the nuclear emulsions; this is presumably because the dislocation density in the grains of the silicon-iron is high, although the long range strain effects are clearly small.

4.6.4 Conclusions

The experiment represents the first in-situ x-ray topographic study of crystal growth under normal growth conditions. The very high intensity of synchrotron radiation allowed topographs to be taken directly through the closed end wall of the alumina tube and permitted very short exposure times so that a significant number of discrete data points could be obtained during the relatively short period of grain growth. In addition, good geometrical resolution could be achieved even with the film some 20 cm from the sample, and clearly the experiment would have been impossible using a conventional laboratory x-ray source.

Improvements in the experiment can be envisaged, particularly with regard to the temperature measurement and control so that reproducible quantitative data can be extracted. A furnace in which the specimen is heated directly by the passage of an electric current and in which thermocouples are welded to the sample would allow accurate temperature

measurement and also eliminate the troublesome warm up period. In addition, the development of direct imaging systems for x-ray topography would overcome the disadvantages of step-by-step photographic recording. However further developments were rendered impossible by the closure of the Synchrotron Radiation Facility at Daresbury Laboratory and the lack of a suitable alternative synchrotron radiation source.

4.7 Synchrotron Topography of the α-γ Phase Transition in Iron

4.7.1 Introduction

Below 916^{o}C iron possesses a body centred cubic structure, known as the α- phase but at this temperature it undergoes a phase transition to the face centred cubic or γ - phase. An attempt was made, using the apparatus described in the previous section, to study the microstructural changes accompanying this phase transition. A sample of electrodeposited iron foil of thickness 45 microns was used in the experiment.

4.7.2 Experimental Technique and Results

The apparatus and experimental technique were the same as those described in section 4.6 for the recrystallization experiment. The iron foil was heated to a maximum nominal temperature of 1000^{o}C over a period of 140 minutes. Topographs were taken of the foil using Polaroid 4 x 5 Land Film Type 52 at intervals of 100^{o}C during the heating. The beam energy and current were 5 GeV and 20 mA respectively and exposures of 10 seconds were adequate. The initial grain size of the electrodeposited iron foil is of the order of 1 micron and no diffraction pattern was obtained at low temperatures because of the resolution of the Polaroid film and the background halo produced by the

alumina tube. The topograph taken at 900°C after 127 minutes of heating (figure 4.9(a)) still shows no diffraction pattern, but 13 minutes later when the nominal temperature had reached 1000°C a diffraction pattern was observed (figure 4.9(b)) indicating a sudden grain growth on passing through the transition temperature. Considerable strain is associated with the grains, as evidenced by the streaking of the images. The sample was maintained at 1000°C for 40 minutes during which time several more topographs were taken. The last of the sequence (figure 4.9(c)) reveals that very little change in the grain structure had occurred during this period. The sample was then cooled at the rate of 200°C hr^{-1} to 900°C with topographs being taken every 20°C. Down to a nominal temperature of 940°C (figure 4.9(d)), little change from the 1000°C grain structure was observed but six minutes later at 920°C (figure 4.9(e)) a dramatic change in grain structure had taken place as the sample cooled through the transition temperature. This new structure remained at 900°C and was still evident when the sample was reheated to a nominal temperature of 950°C (figure 4.9(f)). However 11 minutes later at 1000°C a further structural change had taken place (figure 4.9(g)). Much strain is associated with the grains. The sample was finally cooled rapidly to 900°C when a further structural change had occurred (figure 4.9(h)).

4.7.3 Discussion and Conclusions

The experiment shows that synchrotron radiation can be employed to follow microstructural transitions at high temperatures. Although measurements of grain sizes are not possible because of the streaking of the images, qualitative data can be derived from the number of images

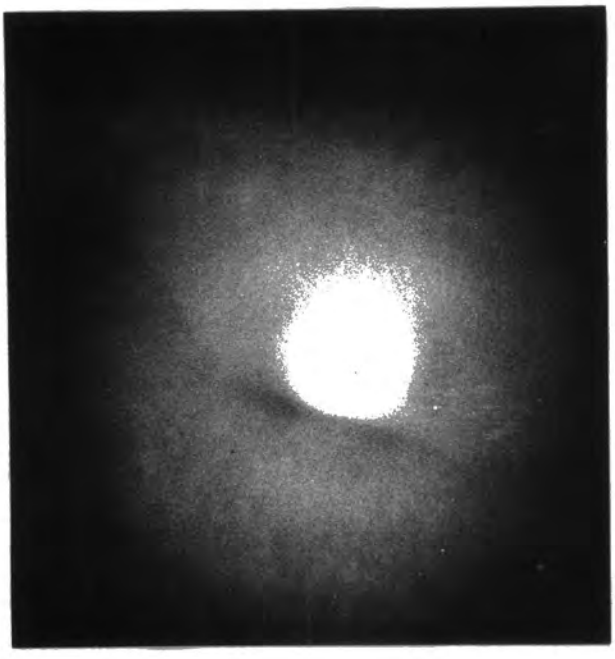

a)

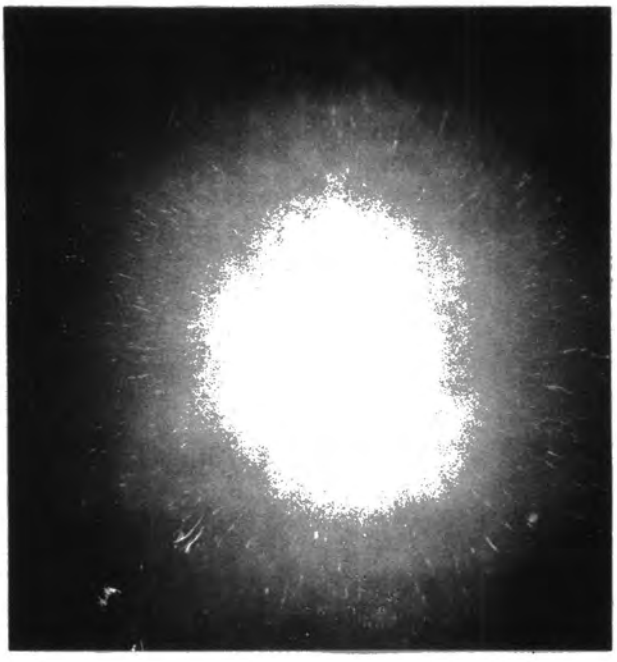

c)

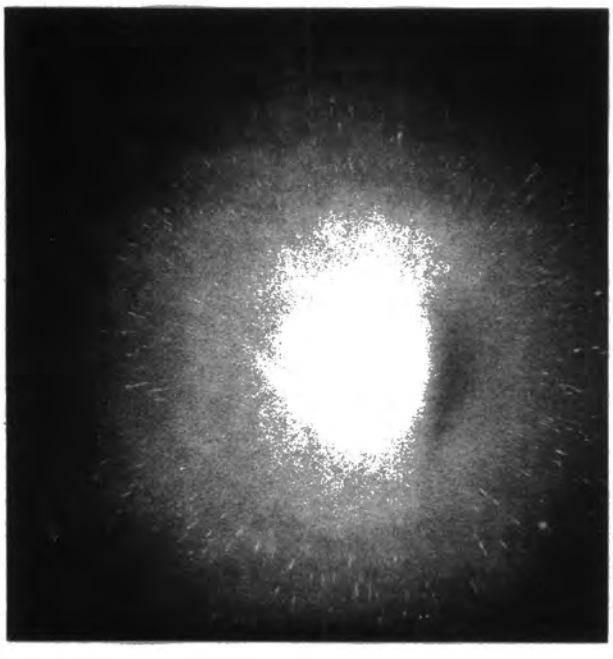

b)

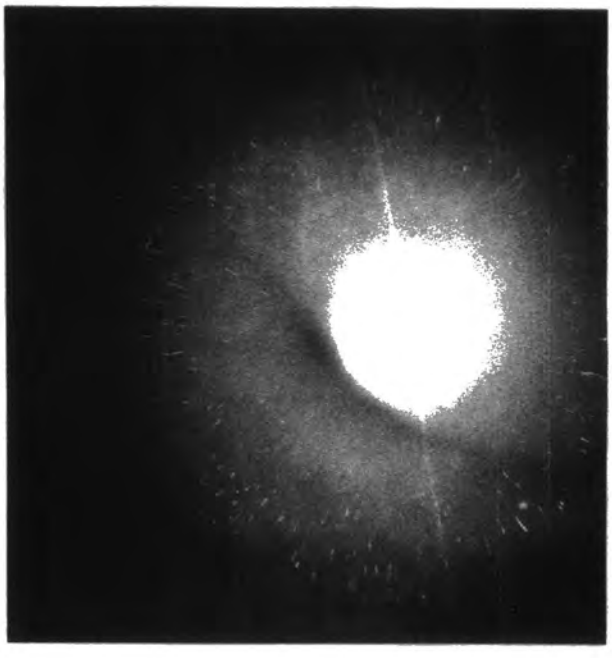

d)

Figure 4.9 Sequence of topographs of iron foil during thermal cycling around the phase transition temperature of 916°C.

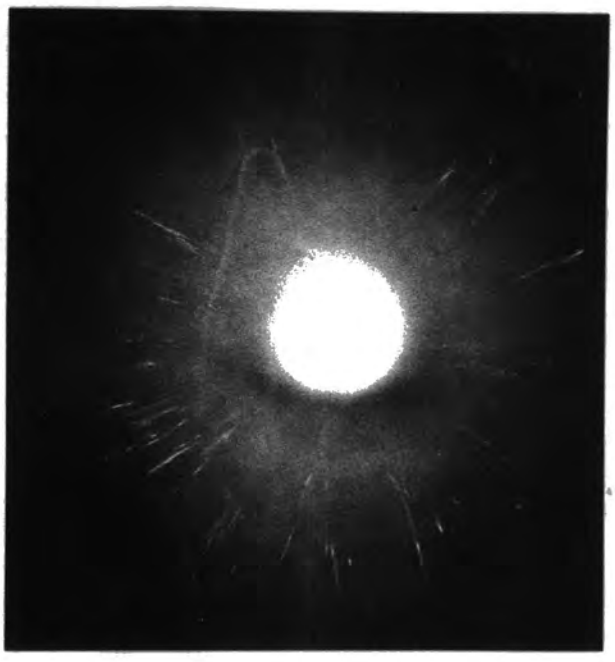

e)

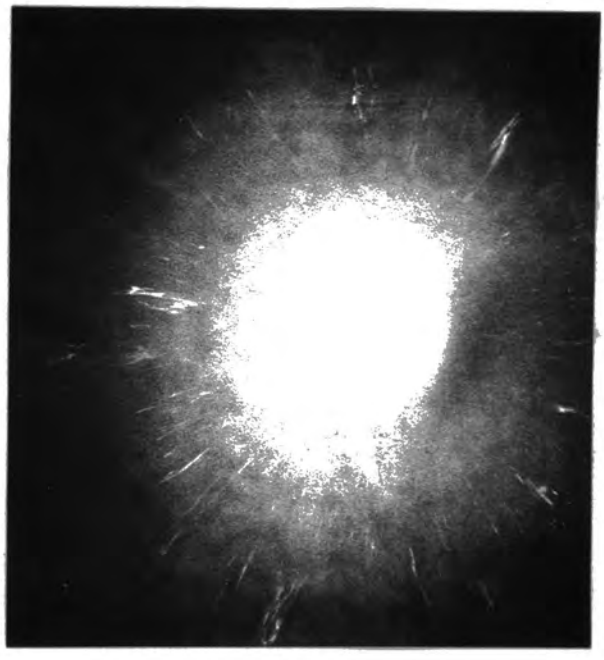

g)

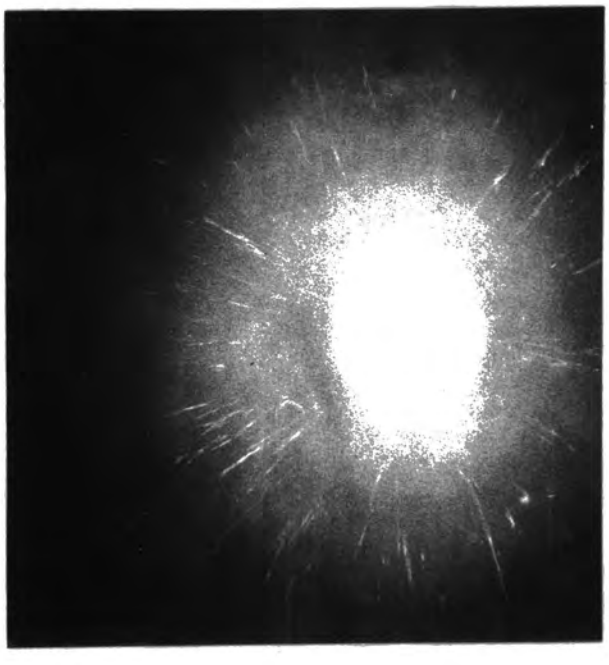

f)

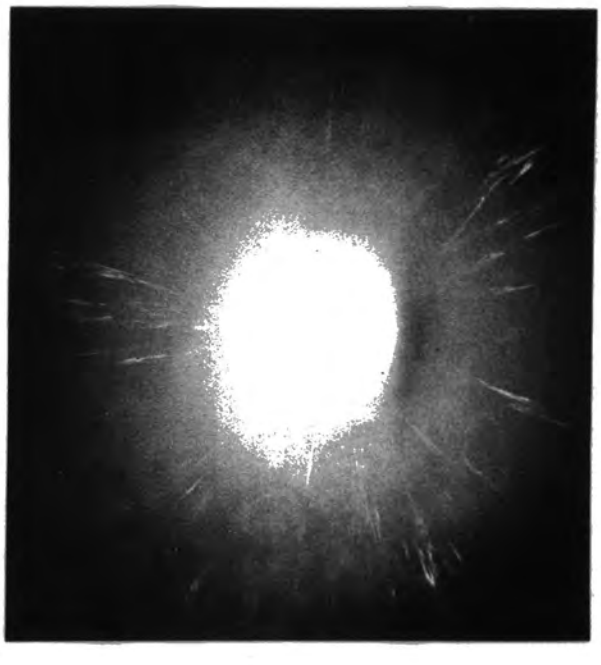

h)

1 cm

present. Clearly the average grain size is increasing with successive crossings of the transition temperature. Furthermore information on the time scale of the structural changes and the strain associated with the phase transition can be derived. Evidently the structural changes occur very quickly on crossing the transition temperature with the generation of considerable strain due to the phase change from body centred cubic to face centred cubic or vice versa.

The temperature measurement again proved to be inadequate. The phase transition occurred in different nominal temperature ranges during heating and cooling and at values higher than the accepted value of $916^{\circ}C$. These thermal lags and inaccuracies are attributed to the fact that the thermocouple was not welded directly to the sample, a modification which it is expected would allow reliable quantitative data to be extracted.

CHAPTER FIVE

HEAT TREATMENT OF ELECTRODEPOSITED IRON FOIL

5.1 Introduction

In Chapter 2 it was demonstrated that the properties of as-produced electrodeposited iron foil are very poor compared with commercially available soft magnetic materials. Crystalline imperfections, impurities, grain boundaries and internal stress all impede domain wall mobility and a reduction of the effect of any of these features can be expected to improve the soft magnetic characteristics of the foil. The simplest way of bringing about an improvement is through suitable heat treatment which has the effect of increasing grain size and relieving stress. Grain growth processes at high temperature in metals were discussed in Chapter 3, and in this chapter the application of some of these processes to electrodeposited iron foil will be covered. The work is divided into the structural effects induced by straightforward annealing treatments and those resulting from strain-anneal techniques. The associated changes in physical properties will be discussed in Chapter 6.

5.2 Annealing Treatments of Iron Foil below the Transition Temperature

5.2.1 Introduction and Experimental Technique

In this section the changes in grain structure resulting from gradual grain growth will be covered. In order to achieve a reasonable rate of growth the annealing temperature should be as high as possible. The b.c.c to f.c.c phase transition occurs at 916^{o}C so an annealing

temperature of 900°C was chosen. The furnace arrangement was very similar to that described in Chapter 4 except that the middle portion of the furnace was used with the result that temperature measurement was more precise because of the smaller temperature gradient at that position. All heat treatments were carried out in an inert atmosphere of high purity argon to minimize the effects of oxidation. The furnace took about 80 minutes to reach 900°C at which temperature the samples were maintained for 2 or 20 hours, whilst the cooling rate was never allowed to exceed $200^{\circ}C\ hr^{-1}$ in order to minimize strain effects due to thermal contraction. The typical superficial area of the samples used was 2 x 5 cm^2, the samples being pushed into place in the furnace tube with a rod and withdrawn using a small magnet on the end of a rod. Slight surface oxidation of the samples took place due to residual oxygen in the tube but the oxide layer could readily be removed by dipping the samples in the etching reagent of ferric chloride in 30% hydrochloric acid for 5 to 10 minutes which also had the effect of revealing the grain boundaries for subsequent microscopical examination. Photographs of large numbers of grains in the annealed samples were taken on a Vickers M.17 industrial microscope and the grain size determined by counting the number of grains in a known area. Typically several hundred grains were counted and the average grain diameter determined on the assumption that the grains are circular. Standard Laue and synchrotron x-ray topographs of the annealed samples were also taken to provide information on grain orientation and perfection.

5.2.2 Results

Most of the foil samples were subjected to the 2 hour anneal at 900°C.

The grain diameters resulting from the anneal varied from about 30 to 100 microns which is of the order of 50 times the grain size of the as-produced foil as determined by the scanning electron microscope. The average grain diameters of individual samples are plotted as a function of foil thickness in figure 5.1. A typical optical micrograph obtained from a foil sample of thickness 45 microns is shown in figure 5.2. The grains are polyhedral in section with typically five or six sides. It is expected that the larger grains spread through the specimen thickness, though the smaller ones probably do not penetrate so far.

A transmission Laue x-ray photograph from the same foil sample is shown in figure 5.3. The pattern is based on the ring formation shown in figure 2.5 for the as-produced foil, but is discontinuous and spotty due to the larger grain size of the annealed foil. The picture was recorded on Polaroid 4 x 5 Land Film Type 57 using Mo Kα radiation with a Zr filter with tube voltage and current settings of 50 kV and 20mA respectively. The specimen to film separation was 3 cm and the exposure time 20 minutes. The distribution of spots round the rings indicates that there is no preferred orientation of the grains in the foil, and this is confirmed by the transmission synchrotron topograph for annealed foil of thickness 45 microns which has already been shown in figure 4.5(b). The slight radial streaking in the latter picture suggests that a small amount of strain is associated with the grains.

Several foil samples were annealed for 20 hours at 900^{o}C to determine whether further gradual grain growth would occur in the extra period of annealing. Table 5.1 shows the average grain sizes of these six

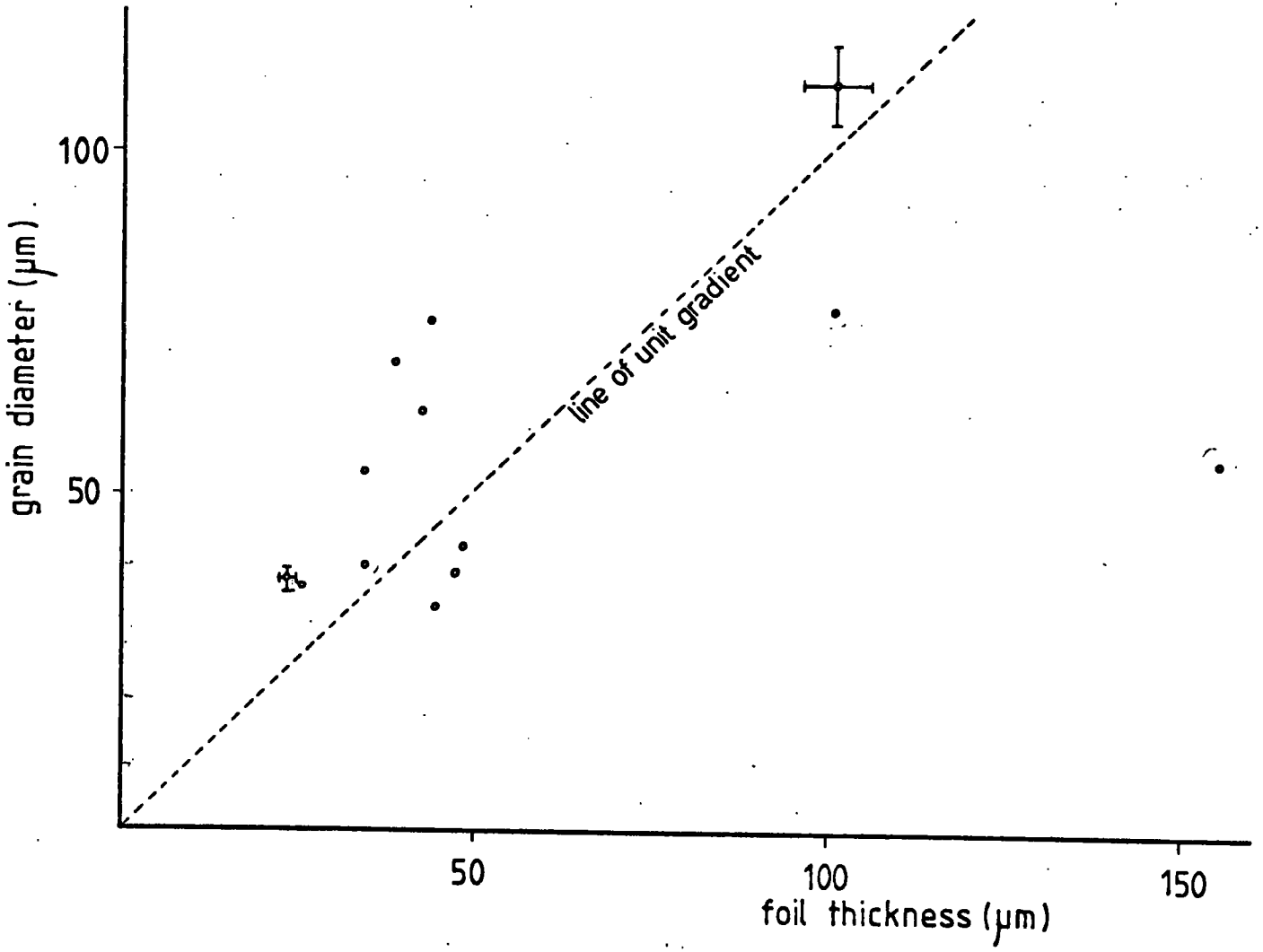

Figure 5.1 Grain diameter after a 2 hour anneal at 900°C against foil thickness.

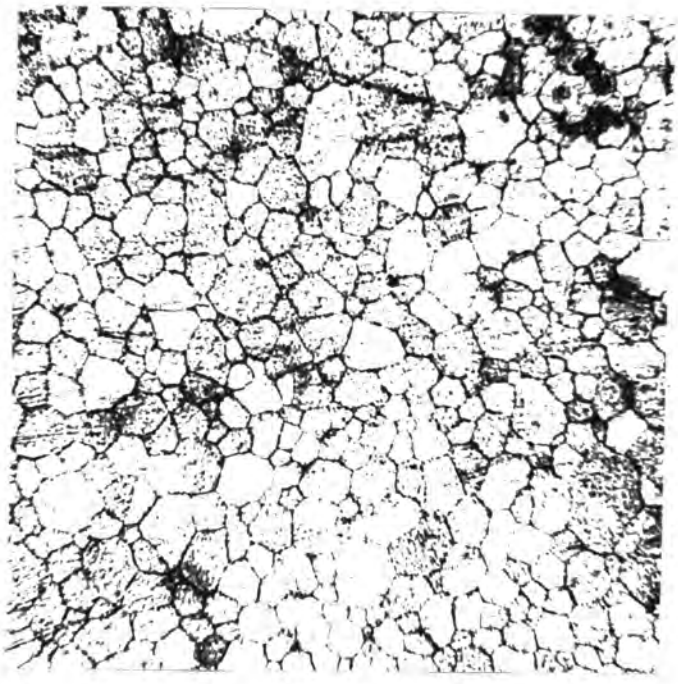

Figure 5.2 Optical photograph of foil annealed for 2 hours at 900°C.

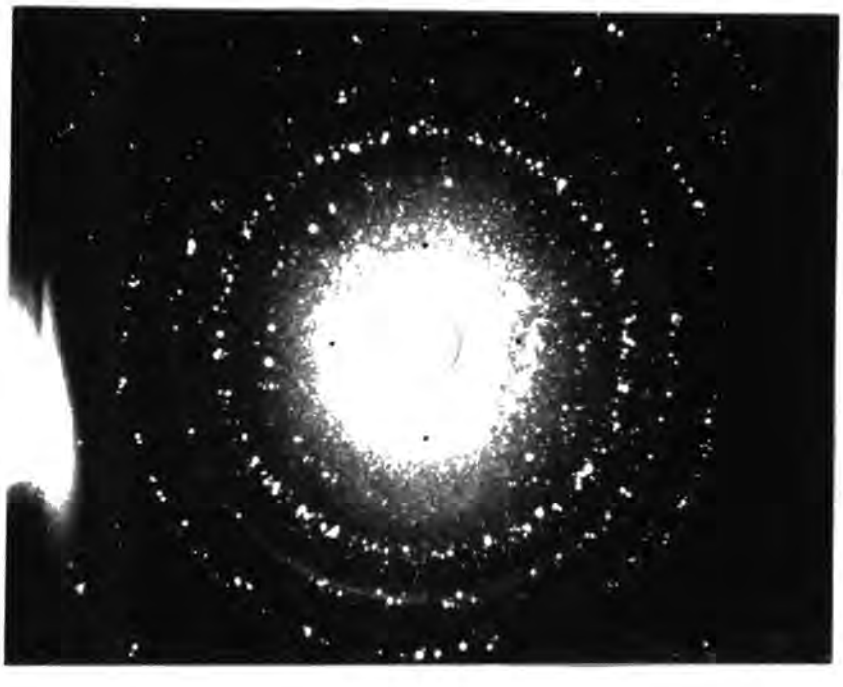

Figure 5.3 Transmission Laue photograph of iron foil annealed for 2 hours at 900°C.

TABLE 5.1 AVERAGE GRAIN DIAMETER AFTER 900°C ANNEAL

Sample Number	Nominal Thickness (μm)	Average Grain Diameter (μm) (± 2.5%) 2 hr Anneal	20 hr Anneal
1	45	33	40
2	44	75	84
3	44	62	86
6	155	55	78
8	49	42	49
10	101	77	112

foil samples after periods of 2 and 20 hours at 900°C. Considering that the initial grain size of the foil is of the order of a micron, it can be seen that little improvement in the grain size results from the extended period of annealing. The ultimate grain size of the foil has apparently almost been reached after 2 hours at 900°C and the additional energy expended in annealing for 20 hours is clearly not justified.

In the light of this observation, the results of figure 5.1 can be compared reasonable favourably with the specimen thickness effect discussed in Chapter 3. For several foil samples, the ultimate grain size is quite close to the foil thickness although deviations from a general trend do occur, perhaps due to slight differences in levels of inclusions which inhibit grain boundary motion.

5.3 Annealing of Iron Foil above the Transition Temperature

The direct observation using synchrotron radiation of the microstructural changes accompanying the cycling of electrodeposited iron foil through the b.c.c. to f.c.c. phase transition temperature of 916°C has already been described in Chapter 4. A more controlled anneal at 1000°C was performed on samples of foil of various thicknesses. After a warm up period of about 100 minutes, the foil was maintained at 1000°C for 2 hours before being cooled at a rate not exceeding 200°C hr^{-1}. After etching as described previously, the foil was examined optically; the grain structure was found to be very irregular with grains up to several millimetres across. A typical optical photograph obtained from a foil sample of thickness 101 microns is shown in figure 5.4.

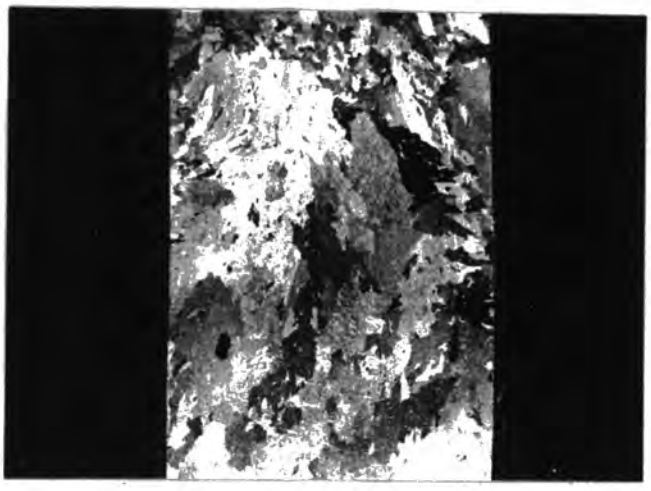

Figure 5.4 Optical photograph of foil annealed for 2 hours at 1000°C.

Figure 5.5 Transmission Laue photograph of foil annealed for 2 hours at 1000°C.

A transmission Laue photograph obtained under the usual conditions of a similar sample is shown in figure 5.5. The radial streaking of the spots indicates that considerable strain is associated with the grains and this is confirmed by the synchrotron topograph shown in figure 5.6 which was recorded on Polaroid 4 x 5 Land Film Type 52 with electron beam energy and current values of 4 GeV and 15 mA respectively and an exposure time of 30 seconds. These results confirm the in situ high temperature observations described in Chapter 4 that the straining is associated with the phase change and that the grain growth occurs rapidly on crossing the transition temperature. Despite the fairly large grain size, foil treated in this way is unlikely to be interesting magnetically because of the high degree of strain.

5.4 Strain-Anneal Treatment of Electrodeposited Iron Foil

5.4.1 Historical Introduction

As an alternative to gradual grain growth techniques, it should be possible to increase the grain size of the iron foil by a suitable recrystallization process. Literature on the recrystallization of iron is rather scarcer than that on silicon-iron because of its limited applicability as a soft magnetic material, but some interesting work has been reported.

Dunn and Walter (1960) have induced secondary recrystallization in 99.99% pure iron of thickness 65 microns after a cold reduction of 75%. The introduction of grain growth inhibitors added to the melt has not proved effective in pure iron, but Kohler (1967) has reported that the diffusion of additional sulphur inhibitors direct into the grain boundaries during recrystallization after cold rolling produces a

Figure 5.6 Synchrotron radiation topograph of iron foil annealed for 2 hours at 1000°C.

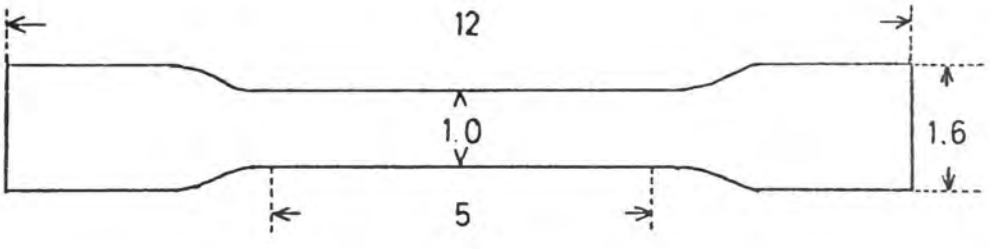

Figure 5.7 Dimensions of test pieces used in strain-anneal technique (figures in cm).

(110) [001] secondary recrystallization texture. The same texture has been produced by Thornburg et al (1976) by primary recrystallization and grain growth in iron containing small amounts of Si, Cr and Mn and good magnetic properties are reported. All these processes involve considerable thickness reduction by cold rolling however, and could not readily or usefully be applied to the electrodeposited iron foil which is already of the same order of thickness as the final product described in the above experiments.

The previous work of greatest interest in relation to the present investigation is that of Antonione et al (1973, 1977) who have studied the kinetic features of recrystallization and grain growth in pure iron after deformation in tension of up to 10%. Working with iron of purity better than 99.998% and grain sizes from 50 to 200 microns, secondary recrystallization at an annealing temperature of 690^{o}C has been observed after elongations of 2 to 10%. The final grain size achieved decreased with increasing deformation. It is not clear whether a critical strain for the onset of secondary recrystallization exists, but undeformed samples underwent normal grain growth.

The work of Antonione et al has been used as a basis for successful attempts to induce secondary recrystallization in electrodeposited iron foil. The technique employed and results obtained will be described in the following sections.

5.4.2 Strain-Anneal Technique

All the deformations involved in the strain-anneal technique were performed on a Hounsfield Tensometer. The test piece dimensions are

shown in figure 5.7. The percentage elongation after straining was determined by measuring with a rule the increase in separation of two lines about 5 cm apart on the gauge length. The straining rate in all cases was 1.6 mm min^{-1}.

In Chapter 2 it was shown that, in the as-produced form, the iron foil can only be extended by a few percent before fracture occurs. Deformations of this extent were found to be insufficient to induce secondary recrystallization upon subsequent annealing. In the experiments of Antonione et al the iron grain size was between 50 and 200 microns compared with the one micron of the as produced electro-deposited iron foil. In general an increase in grain size gives rise to a decrease in yield stress and an increase in the maximum elongation possible before fracture, effects which will be covered in further detail in Chapter 6. By annealing the test pieces for 2 hours at 900°C, as detailed in section 5.2, prior to straining a grain size of the order of 50 microns was achieved and this was found to allow elongations of at least 10% before fracture. After straining the test pieces were again annealed to induce recrystallization. A 20 hour anneal at 900°C was used in order to ensure that all recrystallization effects were complete, and all strain relieved. The cooling rate was the standard 200°C hr^{-1}.

After removal from the furnace the test pieces were immersed in the usual etching reagent to remove the oxide layer and to reveal the grain structure for optical examination.

5.4.3 Results

For small strains below 4% the grain structure after the strain-anneal treatment is very similar to that before, suggesting that the small amount of strain stored in the foil as a result of the deformation has been removed by polygonization. Above 4% strain a transition region is observed in which part of the foil has been transformed by secondary recrystallization into a large grained structure, with crystallites several millimetres across. The transition region varies for different foil samples, but above about 9% strain the entire gauge portion of the foil is transformed. In the transition region the percentage of the foil which has been transformed was estimated using an optical sampling technique and is plotted as a function of strain for 4 different foil samples in figure 5.8.

In another experiment the temperature of the final 20 hour anneal was varied. The percentage transformation is plotted as a function of percentage strain for a foil sample of thickness 45 microns at final annealing temperatures of 700, 800 and 900°C. Very little difference is observed between the three sets of data (figure 5.9).

It was discovered that the foil sample of thickness 155 microns (sample 6) could be extended by as much as 30% after a 2 hour anneal at 900°C and this allowed an investigation of the final grain size after secondary recrystallization as a function of strain. The mean grain diameter was estimated by counting the number of grains in a known area and assuming that the grains are circular in section. The grain diameter is plotted against percentage strain in figure 5.10 and is in general agreement with the observations of Antonione et al that

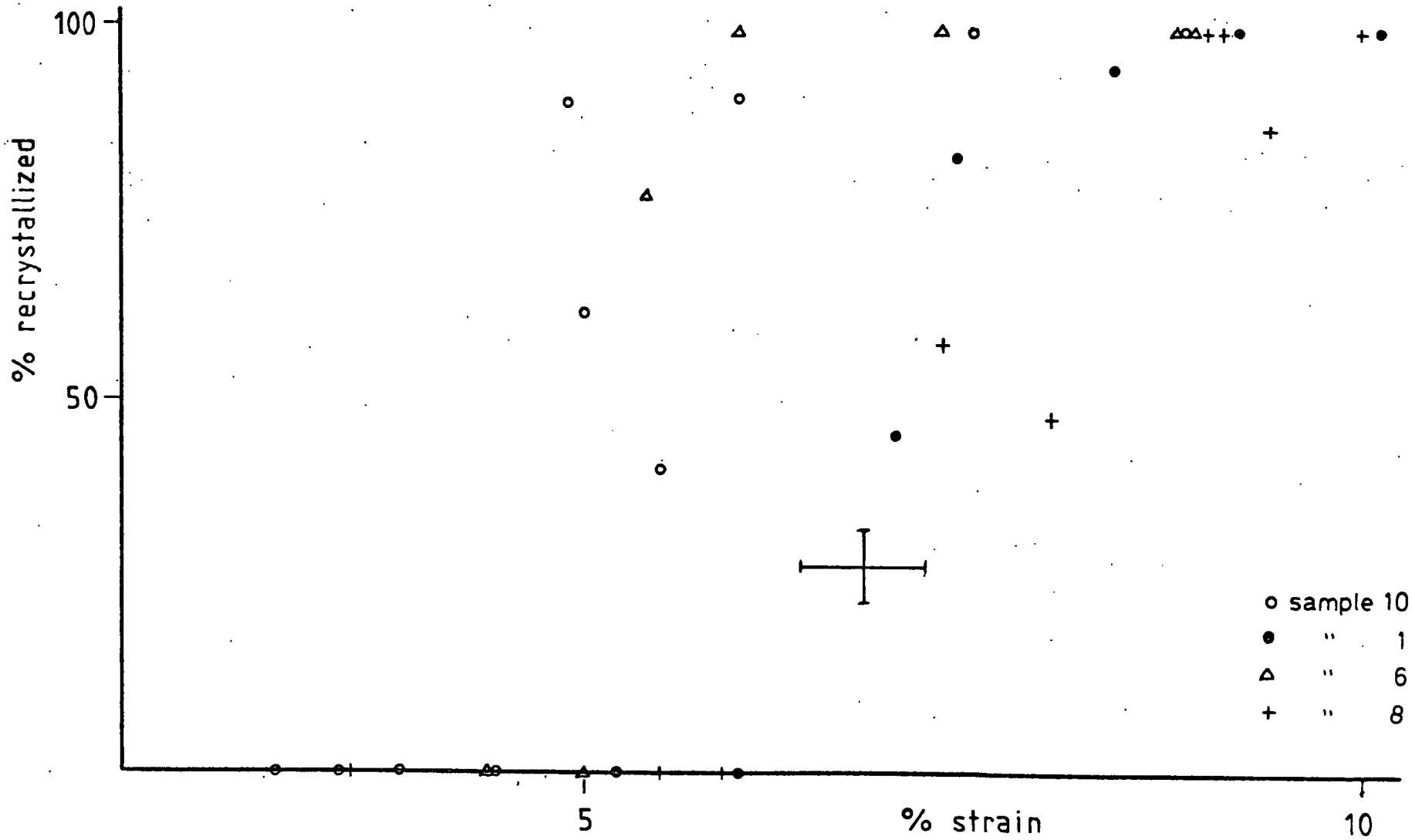

Figure 5.8 Percentage recrystallization against strain relationships for four foil samples at a final anneal temperature of 900°C.

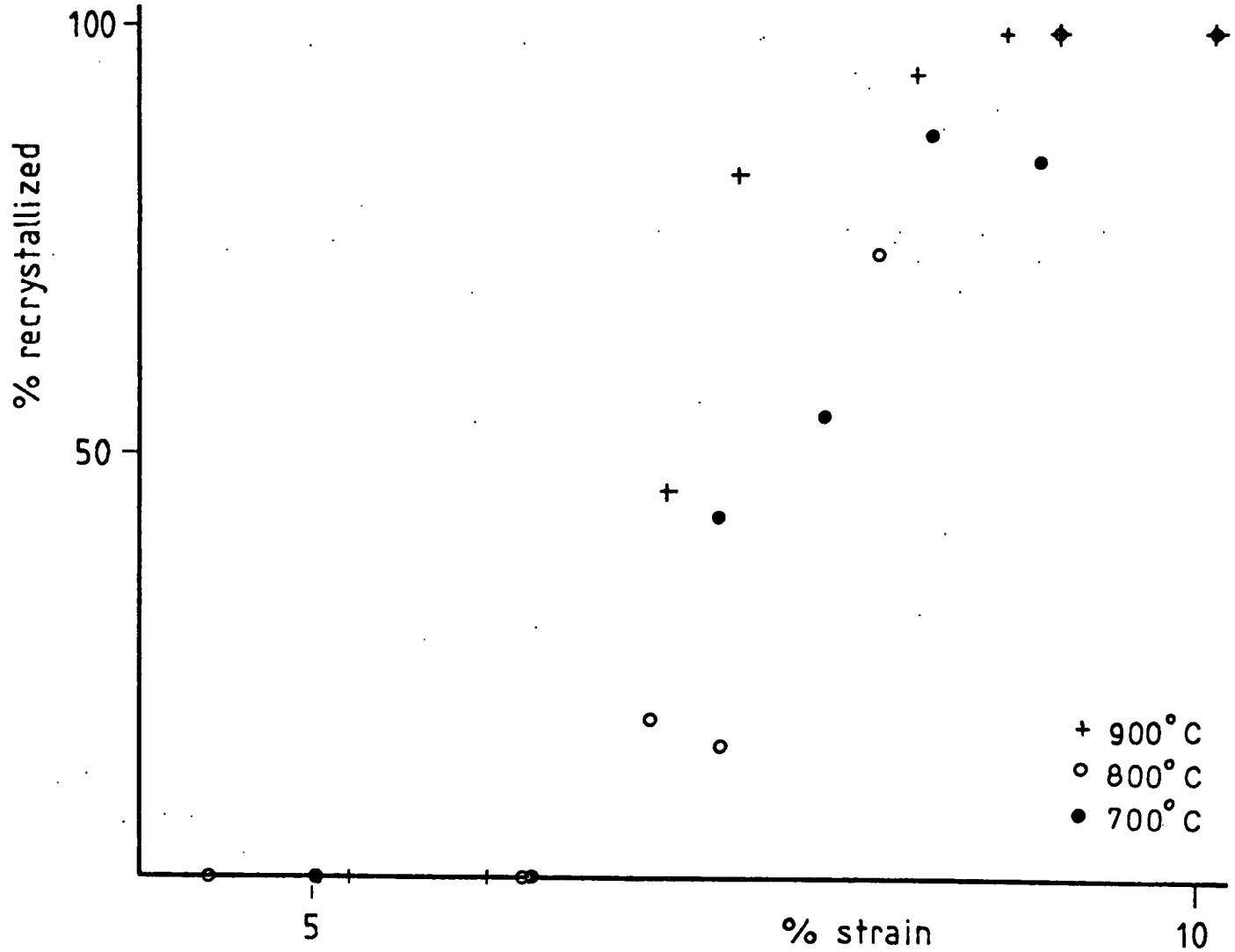

Figure 5.9 Percentage recrystallization against strain relationships for sample 1 foil for three final anneal temperatures.

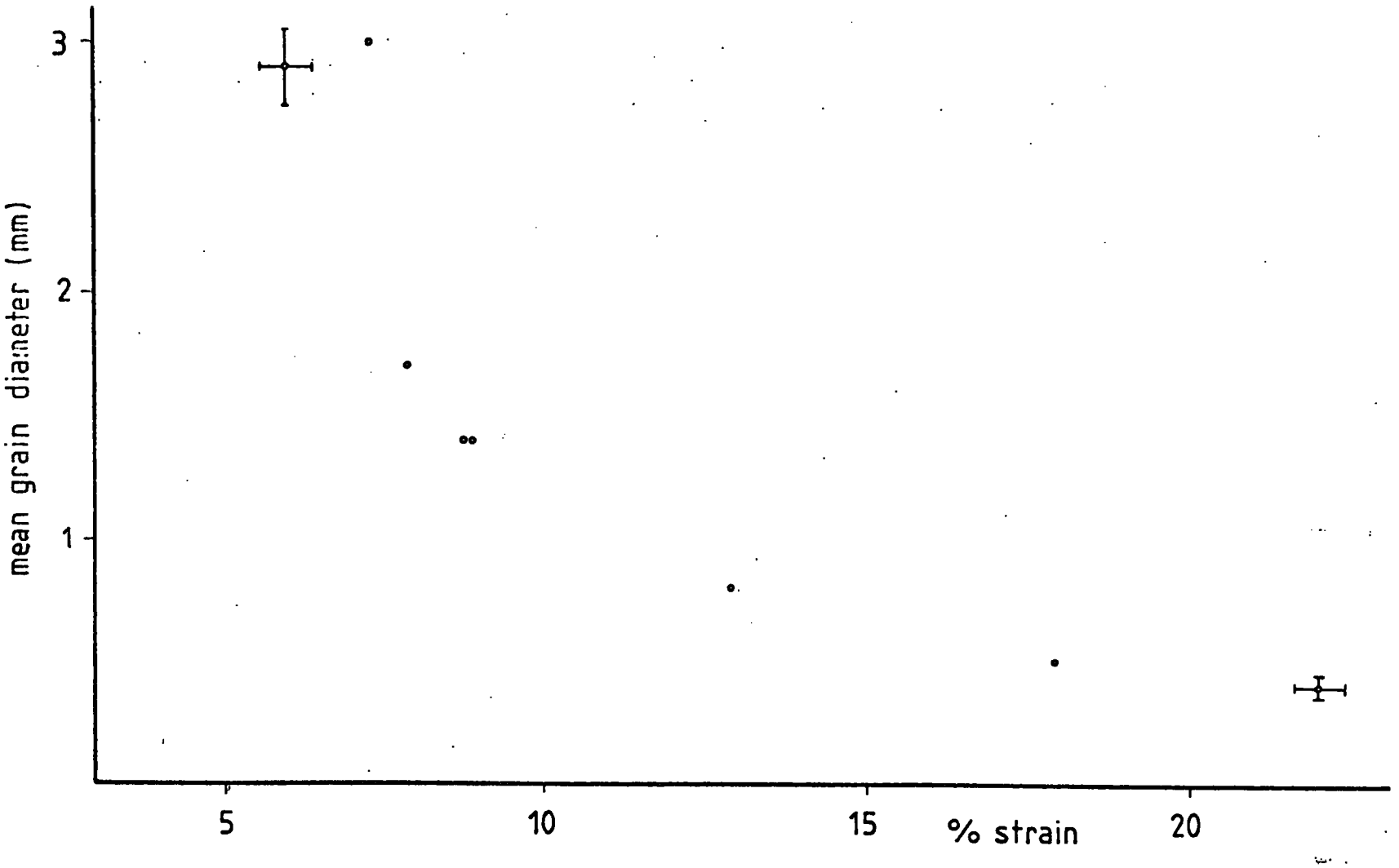

Figure 5.10 Grain diameter against percentage strain after recrystallization of sample 6 foil.

grain size after secondary recrystallization decreases with increasing deformation. A photograph of the grain structure of annealed test pieces of sample 6 foil after various strains is shown in figure 5.11.

The synchrotron radiation source DESY at Hamburg was used to take topographs of the grains of the strain-annealed foil. Examples recorded on Polaroid 4 x 5 Land Film Type 52 are shown in figure 5.12. The electron beam energy and current were 7 GeV and 10 mA respectively and exposure times of about 5 seconds were used. In general the images are clearly defined and undistorted suggesting that the grains are relatively strain free. On a few exposures radial elongation of the images is observed (figure 5.12c) but this is thought to be due to macroscopic bending of the samples. There appears to be no preferred orientation of the grains.

In summary a successful though somewhat tedious technique for producing large, strain-free grains in the foil has been developed, although the value of the process will depend on the properties of the foil in this form, which will be discussed in the next chapter.

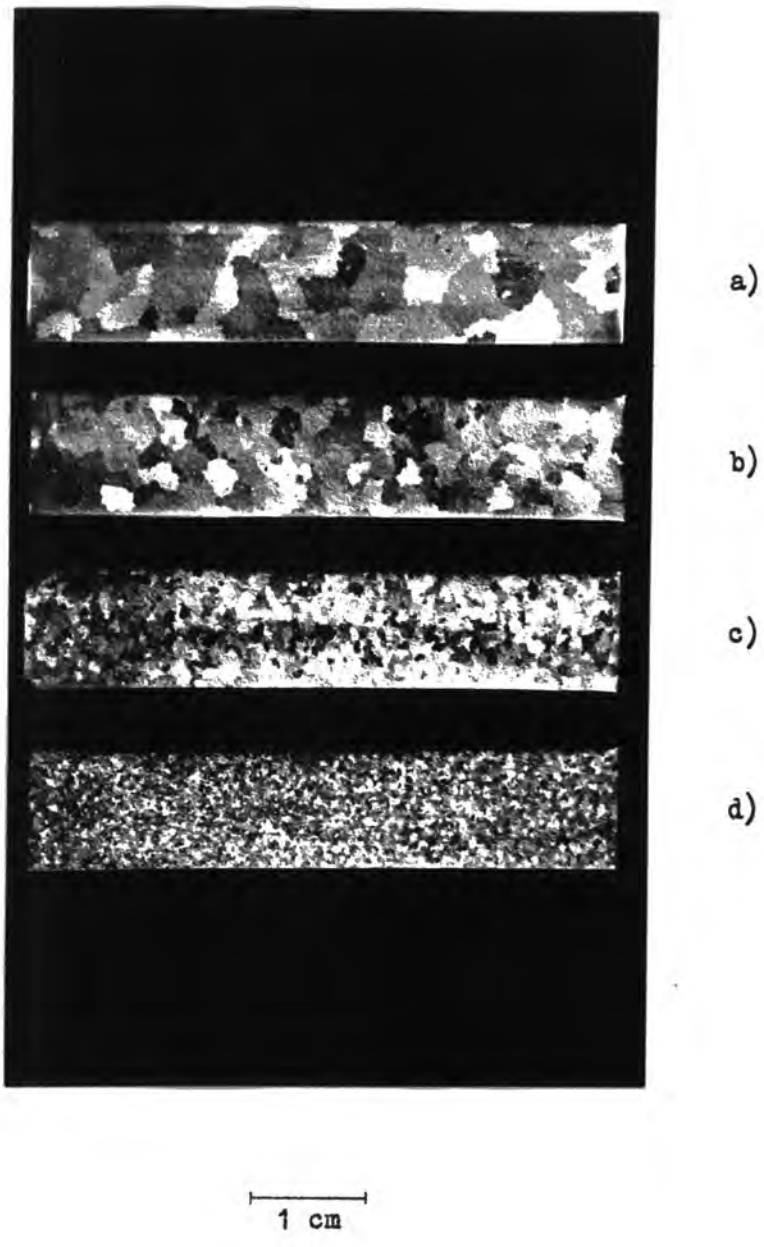

Figure 5.11 Grain structures resulting from the strain-anneal treatment after strains of a) 6.0 % b) 8.8 % c) 12.9 % and d) 17.9 %.

a)

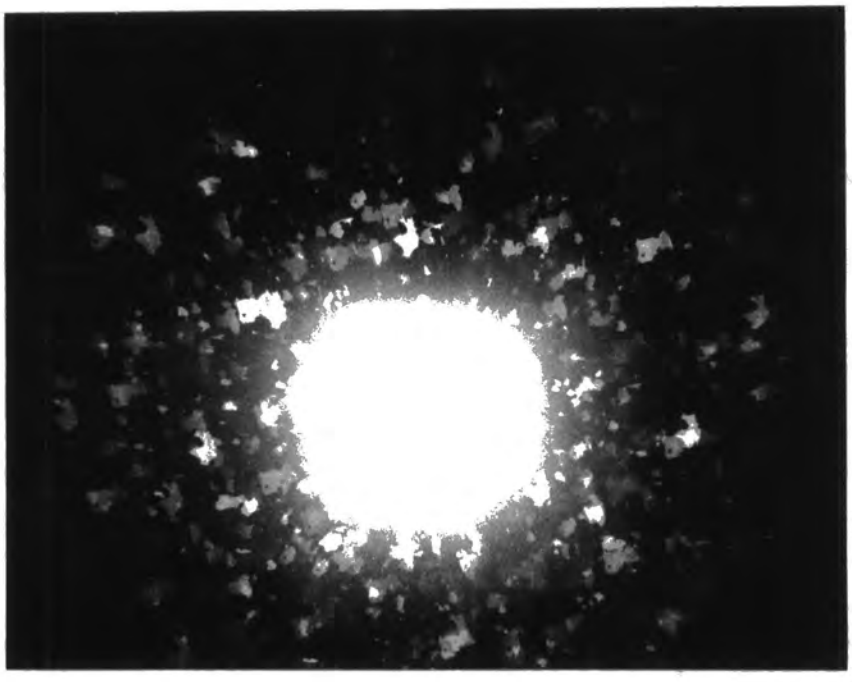

1 cm

b)

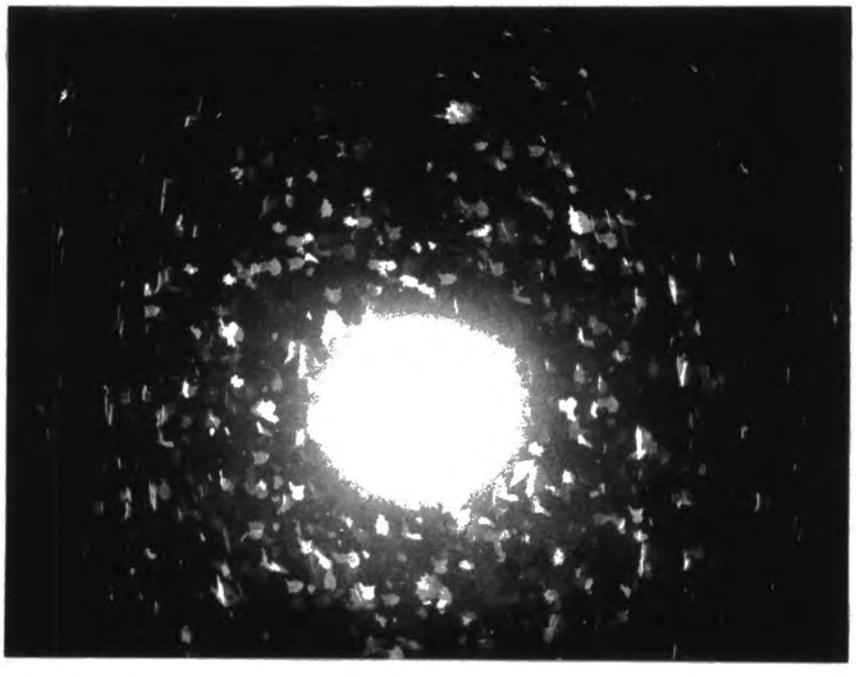

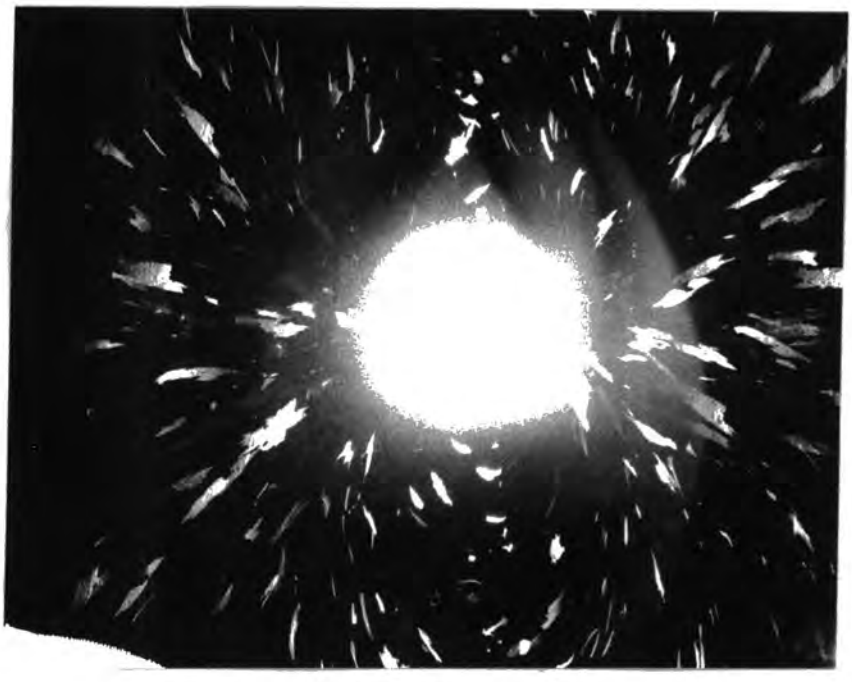

c)

Figure 5.12 Synchrotron topographs of foil subjected to the strain-anneal treatment.

CHAPTER SIX

PROPERTIES OF HEAT TREATED FOIL

6.1 Introduction

In this chapter the physical and magnetic properties of electrodeposited iron foil which has been subjected to the annealing and strain-anneal processes described in the previous chapter will be discussed and compared with the properties of the as-produced foil. The mechanical and magnetic properties resulting from the increased grain size of the heat treated foil will be covered and the possibility of using the foil for magnetic shielding purposes investigated.

6.2 Mechanical Properties

6.2.1 Introduction

The mechanical properties of a polycrystalline metal are rather different from those of a single crystal. The deformation of each grain is dictated by the deformation of its neighbours, giving rise to complicated intersecting slip processes in the various grains. In addition the grain boundaries themselves act as obstacles to the passage of dislocations and slip cannot propagate freely from grain to grain. A stress concentration builds up where the slip band in the first grain meets the neighbouring grain boundaries which helps to initiate slip in these other grains. Plastic yielding for the specimen occurs at a yield stress σ_y given by

$$\sigma_y = \sigma_i + k_y d^{-\frac{1}{2}} \qquad (6.1)$$

where σ_i is the stress required to move dislocations within the grains themselves, d is the average grain diameter and k_y is a constant for a given metal at a given temperature and rate of strain. Equation 6.1

is known as the Hall-Petch equation, and is obeyed by a number of metals including iron and molybdenum (Martin, 1969). The equation leads to the yield stress decreasing with increasing grain size; a decrease in ultimate tensile stress and an increase in the percentage elongation at fracture are also observed. In the following sections an investigation of these relationships for electrodeposited iron foil will be described.

6.2.2 Experimental Procedure and Results

The tensile test strips used in the investigation were of the same dimensions as those shown in figure 2.7. All deformations were performed using a Hounsfield Tensometer at a straining rate of 1.6 mm min^{-1}. The properties of four samples which had been subjected to 2 hour anneals at 900°C and two which had undergone the strain-anneal treatment were tested. In each case three test pieces were used and the figures quoted are the average of the three values obtained.

In table 6.1 the yield stress, ultimate tensile stress and percentage elongation at fracture for the four samples which had undergone the straightforward annealing treatment are shown. The grain sizes quoted are those given in the previous chapter. If the figures are compared with those given in table 2.1 for the as-produced foil it can be seen that the yield stress has been reduced by a factor of between 4 and 8 as a result of the coarsening of the grain structure, whilst the ultimate tensile stress has been reduced by a factor of about 2.5 and the percentage elongation at fracture dramatically increased, particularly in the case of the sample 6 foil which could be extended by more than 30% before fracture occurred.

TABLE 6.1 MECHANICAL PROPERTIES OF FOIL ANNEALED FOR 2 HR AT 900°C

Sample Number	Nominal Thickness (μm)	Grain Diameter (μm)	Yield Stress ($kg\ mm^{-2}$) ($\pm$ 5%)	Ultimate Tensile Stress ($kg\ mm^{-2}$) ($\pm$ 5%)	Percentage Elongation at Fracture ($\pm$ 0.5)
1	45	33	7.9	17.4	17.4
6	155	55	8.3	18.4	31.4
10	101	77	5.9	15.3	14.1
17	101	110	5.1	15.3	17.0

Only two foil samples were tested mechanically after the strain-anneal treatment because of the difficulty of producing samples with the same grain size. Test pieces were subjected to similar strains after the 2 hour pre-anneal at 900°C and then annealed for 20 hours at the same temperature. A light etch was used to reveal the grain structure and the grain size estimated by counting the number of grains in a given area. When three test pieces with similar grain sizes had been obtained for each sample, they were subjected to the tensile test. The results for all six test pieces and the average values for each of the two foil samples are displayed in table 6.2. Further reductions compared with the data in table 6.1 in the yield and ultimate tensile stresses associated with the much larger grain sizes are observed. The percentage elongation at fracture is slightly larger in the case of the sample 10 foil, whilst the values for the sample 6 foil are rather inconsistent and generally lower than those obtained after the straightforward annealing treatment.

The validity of the Hall-Petch equation for electrodeposited iron foil has been investigated in the case of the sample 6 and 10 foils. Only three data points are available for each foil sample, and one of these is only approximate as the exact value of the grain size of the as-produced foil is not known. A figure of 1 micron has been assumed. The three data points correspond to the as-produced, annealed (2 hr, 900°C) and strain-annealed conditions of the foil. The yield stress σ_y has been plotted against the reciprocal of the square root of the grain diameter d in figure 6.1. The data is too limited to draw significant conclusions about the applicability of the Hall-Petch equation, although the qualitative trend of the figures is correct.

TABLE 6.2 MECHANICAL PROPERTIES OF STRAIN-ANNEALED FOIL

Sample Number	Nominal Thickness (μm)	Grain Diameter (mm)	Yield Stress ($kg\ mm^{-2}$) ($\pm$ 5%)	Ultimate Tensile Stress ($kg\ mm^{-2}$) ($\pm$ 5%)	Percentage Elongation at Fracture ($\pm$ 0.5)	
6	155	3.7d	3.5	11.1	22.4	
6	155	4.0	4.2	10.3	15.6	
6	155	3.8	3.7	9.5	26.9	
10	101	1.2	4.7	10.0	17.5	
10	101	1.2	4.7	10.1	16.0	
10	101	1.2	4.8	9.9	16.6	
6	155	3.8	3.8	10.3	21.6	Average values
10	101	1.2	4.7	10.0	16.7	

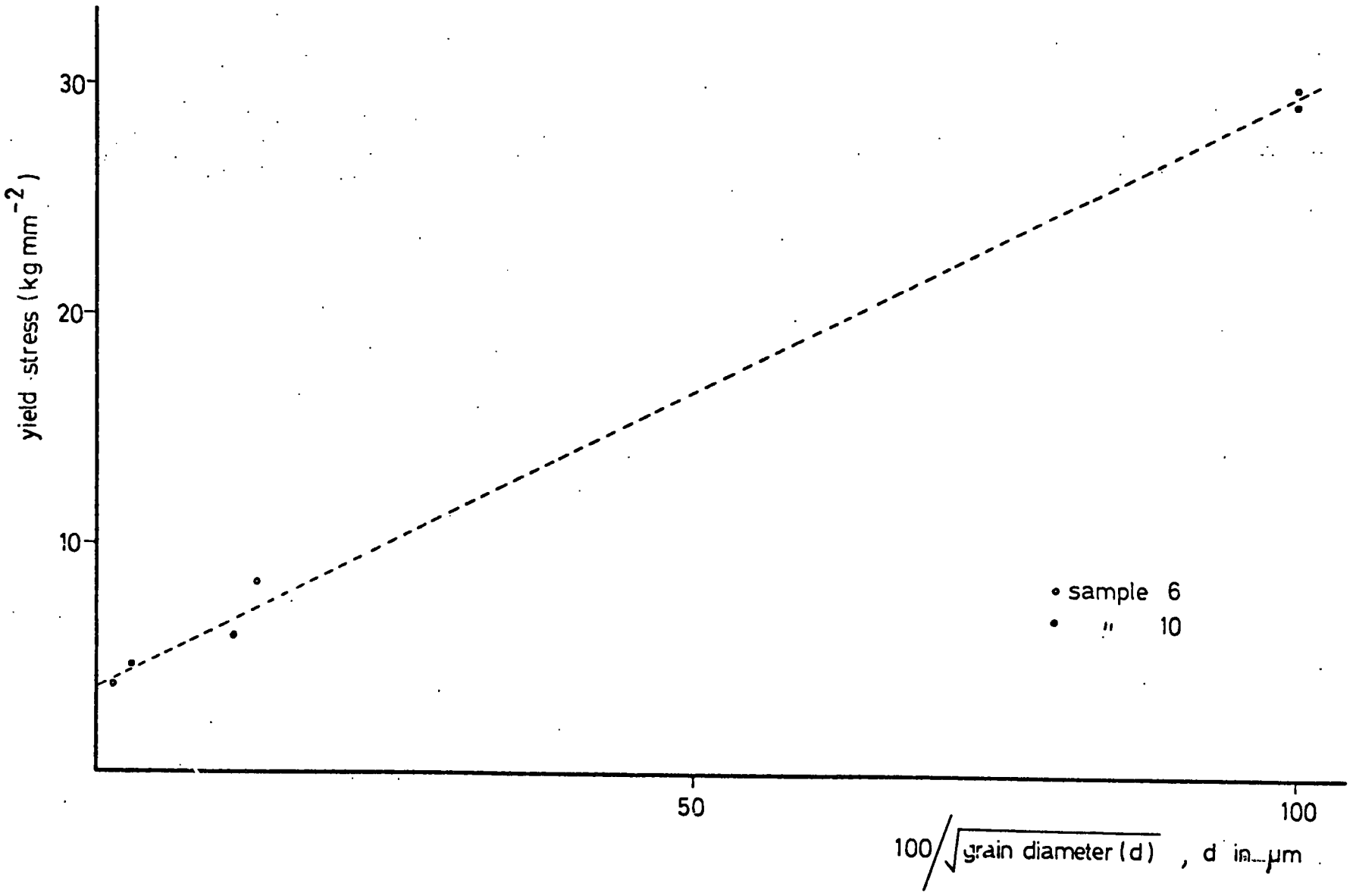

Figure 6.1 Yield stress against reciprocal of root grain diameter for two foil samples.

From figure 6.1 the stress σ_i required to move dislocations within the grains themselves is of the order of 4 kg mm^{-2}.

6.3 Magnetic Properties

6.3.1 Introduction

The coercive force of various foil samples subjected to annealing and strain-anneal treatments has been measured. It is expected that the increase in grain size will improve the soft magnetic characteristics of the foil, though a significant change is necessary before the foil can be regarded as competitive with commercially available soft magnetic materials. An estimate of the maximum permeability of the annealed foil was also made using a similar extrapolation technique to that described for the as-produced foil in Chapter 2.

6.3.2 Results

The hysteresis loop plotter described in Chapter 2 was used to obtain all the magnetic data for heat treated foils, with rectangular test pieces 5 cm x 1 cm again being used. In table 6.3 the coercive force of six foil samples after annealing treatments at 900°C for periods of 2 and 20 hours is displayed. Each figure is the average value obtained from three test pieces. The coercive force has been reduced by a factor of between 4 and 6 compared with the data for as-produced foil presented in table 2.2; within measurement limits the longer anneal is no more effective than the short one. The coercive force of foil which had been annealed above the transition temperature was not investigated systematically because of the poor quality of the grain structure, but the sample 1 foil had an identical coercive force after 2 hour anneals at 900°C and 1000°C.

TABLE 6.3 COERCIVE FORCE AFTER 900°C ANNEAL

Sample Number	Nominal Thickness (μm)	Coercive Force (Oe) (± 5%) 2 hr Anneal	20 hr Anneal
1	45	1.8	1.7
2	44	1.7	1.7
3	44	1.8	1.6
6	155	1.6	1.4
8	49	1.6	1.6
10	101	1.3	1.1

TABLE 6.4 COERCIVE FORCE AFTER STRAIN-ANNEAL TREATMENT

Sample Number	Nominal Thickness (μm)	Temperature of Final Anneal (°C)	Coercive Force (Oe)
1	45	700	1.77 ± 0.04
1	45	800	1.85 ± 0.05
1	45	900	1.75 ± 0.04
6	155	900	1.59 ± 0.02
8	49	900	1.62 ± 0.03
10	101	900	1.18 ± 0.02

All the four foil samples which had undergone the strain-anneal treatment were tested in the hysteresis loop plotter after the 5 cm x 1 cm gauge portion had been cut from the oar shaped test pieces shown in figure 5.7. In all cases the coercive force was found to be independent of the final grain size of the foil; the values were similar regardless of whether the degree of strain introduced in the strain-anneal process had been sufficient to induce secondary recrystallization to the very large grained structure. Consequently all the results for a given foil sample have been grouped together and an average value taken. The results are displayed in table 6.4. For the case of the sample 1 foil three different final anneal temperatures were used but the coercive force was found to be independent of this parameter. The coercive forces are also very similar to those obtained using the straightforward annealing treatments which were displayed in table 6.3.

Evidently all the heat treatments performed on the iron foil have a similar effect upon the magnetic properties and the limit to the improvement that can be achieved by increasing the grain size has been reached at a grain size of about 50 microns. Further improvement could probably be effected by reducing the already low impurity levels by some electrotransport technique or by developing a technique for introducing a degree of preferred orientation into the grain structure.

Since all the heat treated samples have similar hysteresis loops, a single photograph is included as a typical example. This is shown in figure 6.2 and was obtained from a foil sample of thickness 101 microns which had undergone a 2 hour anneal at 900°C.

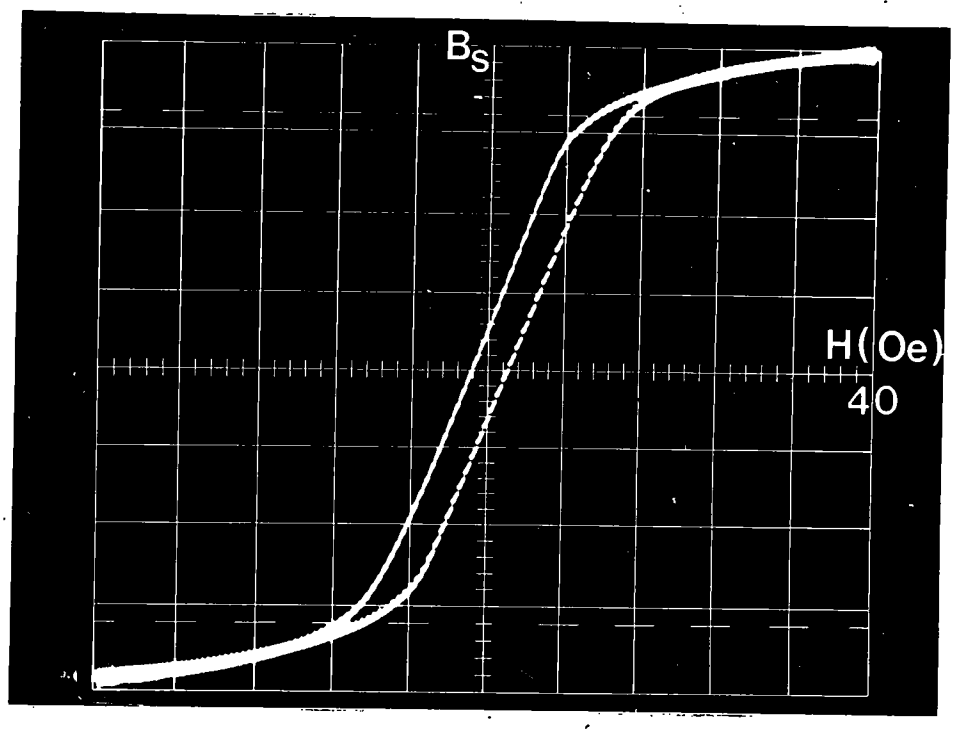

Figure 6.2 Sample hysteresis loop from foil annealed for 2 hours at 900°C.

An estimate of the maximum permeability of the heat treated foil was obtained by an extrapolation technique similar to that explained in Chapter 2. The hysteresis loops were again sheared due to the demagnetizing field which increases with increasing foil thickness. The measured maximum permeability is plotted as a function of foil thickness for two separate foil samples in figure 6.3. The foil samples had both undergone a 2 hour anneal at 900°C. Clearly a linear extrapolation is invalid in this case, although all the points lie on a fairly well defined line. A flexicurve extrapolation has been used to obtain an estimate of the maximum permeability of the heat treated foil corresponding to zero thickness and hence zero demagnetizing field. A value of 4000 was obtained, though an uncertainty of at least 20% must be associated with this value. This is about four times the maximum permeability of the as-produced foil.

6.4 Domain Observations on Electrodeposited Iron Foil

6.4.1 The Colloid Technique

The colloid technique, which originates from the work of Bitter (1931, 1932), is the most widely used method of observing magnetic domain structures. The technique consists of allowing fine magnetic particles to settle onto the surface of the material under examination. The particles generally consist of a single domain and have a magnetic moment; under the influence of a non-uniform field they are attracted to local maxima in the field intensity, in particular to the intersection of domain walls with the specimen surface. It is essential that the surface under study be flat and strain free otherwise complicated "maze" patterns characteristic of the state of strain of the surface layer rather than the underlying domain structure are obtained. Rather stringent conditions govern the size of particles which contribute to

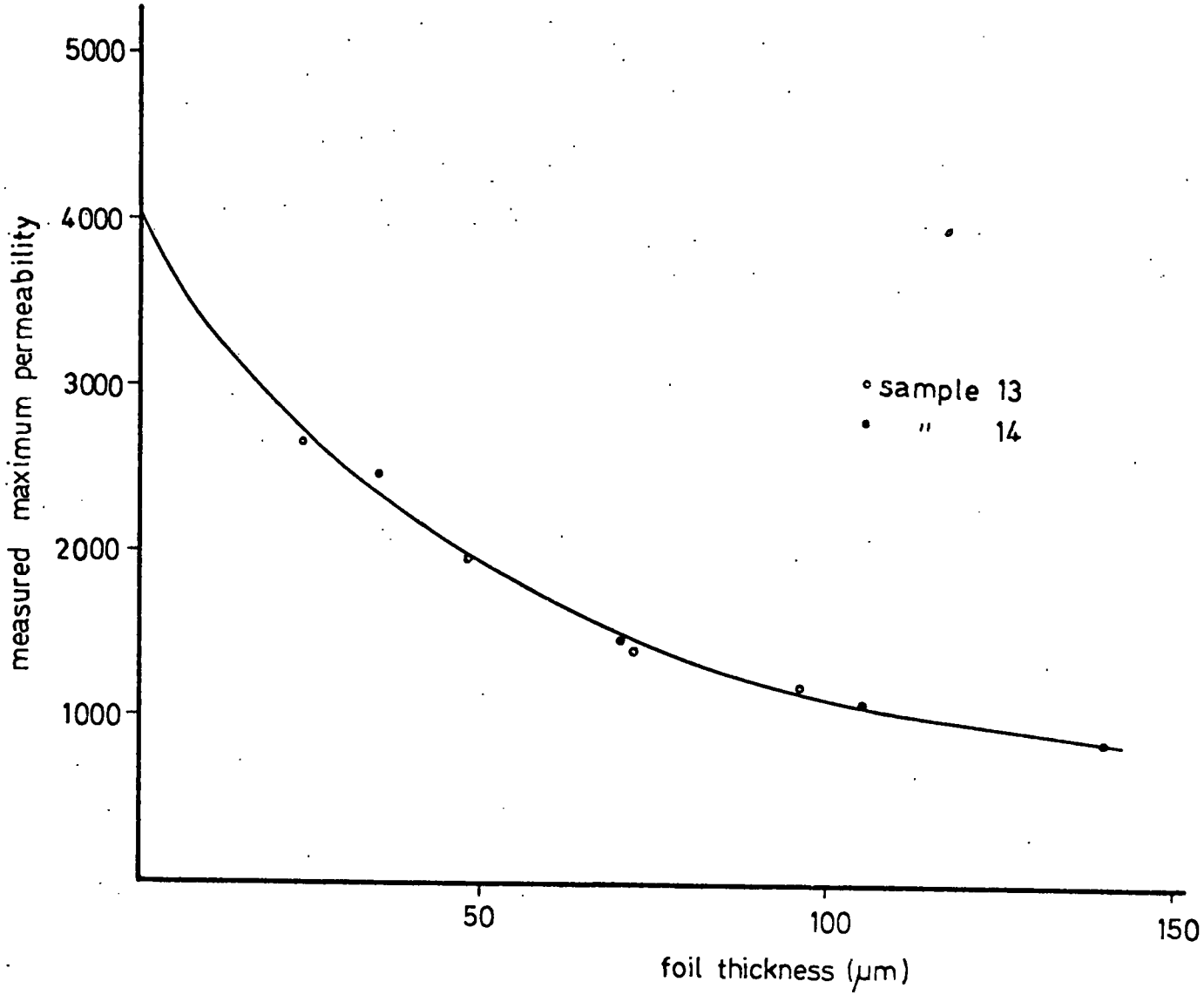

Figure 6.3 Measured maximum permeability against foil thickness for two annealed foil samples.

pattern formation. Larger particles tend to aggregate in their own self fields whilst smaller particles undergo predominantly thermal motion. The useful particle diameter is found to encompass a small range around 100 Å.

The magnetic particles can be applied to the specimen surface in two ways. In the wet colloid technique a colloidal suspension of magnetic particles in a suitable liquid is placed on the surface of the sample and the particles are then attracted to the regions of maximum stray field. In the dry colloid method the magnetic particles are produced by coalescence from the vapour phase in a low pressure atmosphere of an inert gas. The sample is supported a few centimetres from the evaporating filament and the particles settle onto the surface under the influence of the stray fields present.

Both techniques have areas of superiority: the wet colloid technique is simpler to employ and can be used in a limited way to study dynamic changes in domain structure, whilst the dry colloid technique can be used over a much wider temperature range since the problem of freezing or evaporation of the colloidal suspension is eliminated.

With either colloid method the surface domain patterns observed are very difficult to interpret unless the surface under examination contains at least one easy axis of magnetization. The patterns formed on an arbitrary crystal plane generally correspond to a complex surface closure structure and are not representative of the underlying bulk domain structure.

The colloid technique, along with historical references, is covered in further detail by Carey and Isaac (1966).

6.4.2 Experimental Methods

Both wet and dry colloid techniques have been used to study the domain patterns on electrodeposited iron foil. The observations were confined to large grained foil produced either by annealing at 1000°C for 2 hours or by the strain-anneal technique described in Chapter 5. All patterns were obtained at room temperature. Flat, strain free iron surfaces were produced using the mechanical and electrolytic polishing technique described in Chapter 2.

The wet colloid used was water based "Ferrofluid A01" produced by Ferrofluidics Corporation. After dilution a drop of the colloid was placed on the iron surface and covered with a microscope cover slip to give a uniform film of colloid over the surface and reduce the rate of evaporation. The patterns obtained were observed and photographed using a Vickers M17 Industrial Microscope.

The dry colloid technique was performed using the evaporation chamber described by Mundell (1976). In the chamber, fine magnetic particles were produced by evaporation of iron from a tungsten filament in a low pressure inert gas atmosphere. The sample was supported several centimetres above the filament and the particles were carried to the sample by the thermal currents produced by the hot filament. The parameters governing the particle size are the filament temperature, the type, pressure and temperature of the inert gas and the type of metal being evaporated. The experimental conditions yielding the optimum domain patterns have been determined by Smith (1978) and are

summarized as follows. The evaporation was performed in an atmosphere of helium at a pressure of 1 torr. A V-shaped filament was formed from tungsten wire of 99.97% purity and 1 mm diameter. The polished iron sample was attached to the underside of a glass slide with sellotape and supported 7 cm above the filament. In the work of Smith the evaporating metal was iron wire of 99.99% purity and 0.27 mm diameter. In this work however it was considered appropriate to use electrodeposited iron foil, whose purity is better than 99.9%, as the evaporating metal. A strip of foil 12 microns thick, 1.5 mm wide and 200 mm long was wound round the tip of the tungsten filament. A D.C. voltage of 2.5 V applied to the filament for 5 seconds produced satisfactory domain patterns which were observed and photographed as before.

6.4.3 Results and Discussion

The first series of domain patterns, shown in figure 6.4, was obtained using the wet colloid technique on the surface of a sample of foil 101 microns thick which had been subjected to a 2 hour anneal at 1000°C and had an average grain diameter of the order of a few millimetres.

In figures 6.4(a) and (b), obtained from different parts of the same large grain, we see parallel 180° domain walls, spaced by between 70 and 100 microns. The domains themselves contain a considerable number of daggers, and the situation is interpreted as follows. The specimen surface is lying almost in the (110) plane, with the domains magnetized in the [001] direction. This [001] direction lies a few degrees out of the specimen surface which leads to the formation of the daggers which are regions of reverse magnetization reducing the free pole energy at the surface. Bates (1965) has varied the angle of deviation

a)

100 μm

b)

Figure 6.4 Domain patterns observed using the wet colloid technique on the surface of foil annealed for 2 hours at 1000°C.

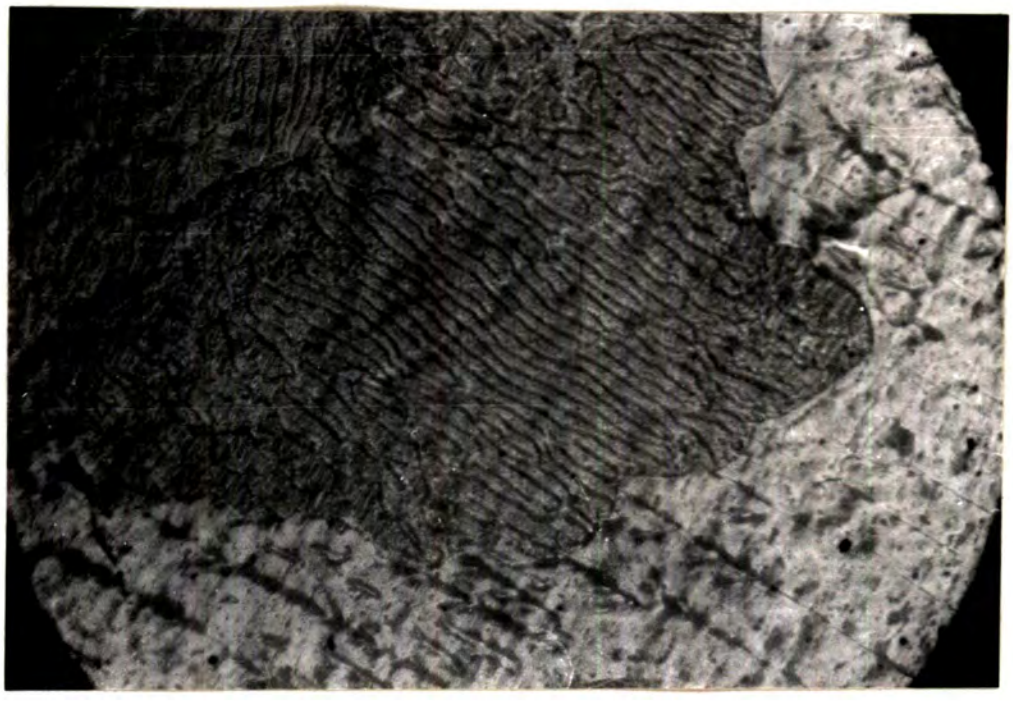

c)

100 µm

d)

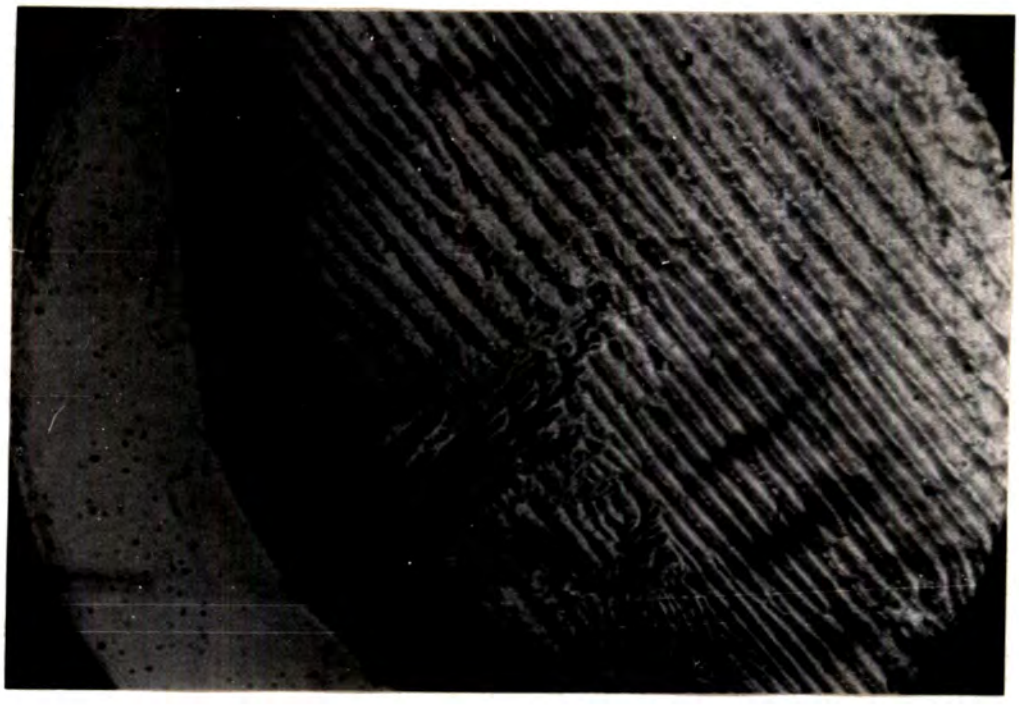

e)

100 µm

f)

between the (110) plane and the surface of a silicon-iron specimen and found that daggers appeared between the domain walls for deviations of between 1^{o} and 4^{o}.

In figure 6.4(c) two grains are evident. In that occupying the bottom and right hand side of the picture, parallel fairly widely spaced domain walls are seen. A small number of daggers exist, indicating as above that the surface of the grain is close to a (110) plane. The orientation of the central grain is clearly much more complicated and the pattern seen probably represents a surface closure structure and its wavy nature may indicate some variable residual stress.

The main grain in figure 6.4(d) contains predominantly parallel walls spaced by between 10 and 30 microns. Towards the right hand side of the grain the main domain wall pattern is complicated by the presence of wavy more closely packed lines, possibly indicating a region of local strain.

Figure 6.4(e) was obtained from a grain at the corner of the specimen and shows a more complicated contrast effect, with the colloid particles being spread widely across the domain walls so that at the bottom right hand corner of the picture in particular the contrast appears to be between adjacent domains rather than between domains and walls. A considerable number of closure domains exist, these having the function of reducing the free pole surface energy at the sample edges.

Several grains are covered in figure 6.4(f). The grain at the right hand side of the picture shows a simple, parallel 180^{o} domain wall

structure indicating that the surface of this grain probably contains a (100) plane, the domains being magnetized in the [001] direction. The central grain exhibits a slightly complicated "fir-tree" domain structure. These patterns were shown by Williams, Bozorth and Shockley (1949), working with silicon-iron, to occur on surfaces misoriented by up to 3° from the (100) plane. The fir-trees are centred on the main domain walls and are transversely magnetized superficial domain structures which cause partial flux closure and reduce the free pole surface energy. If the main walls are assumed to lie along [001] directions, then the [001] direction in the central grain is misoriented by about 40° from that in the grain on the right hand side of the picture. The other grains present show very complicated structures and clearly their surfaces do not lie close to any simple crystallographic planes.

The patterns which have been shown in figure 6.4 were selected from a very large number of grains which exhibited no interpretable structures. This supports the x-ray evidence, presented in Chapter 5, that after a 2 hour anneal at $1000^{\circ}C$ the foil has a randomly oriented grain structure.

Figures 6.5 and 6.6 present a number of domain patterns on 2 samples of foil 101 microns thick which had been subjected to the strain-anneal treatment consisting of a 2 hour anneal at $900^{\circ}C$, a deformation in tension of about 10% and a final 20 hour anneal at $900^{\circ}C$. The patterns in figure 6.5 were obtained using Ferrofluid: figure 6.5(a) shows a complicated fir-tree pattern, whilst the main grain in figure 6.5(b) displays a zig-zag wall structure. The surface domain structure in the latter picture consists of triangular prismatic closure domains magnetized parallel to the specimen surface, which is a (100) plane, and

a)

100 μm

b)

Figure 6.5 Domain patterns obtained using the wet colloid technique on the surface of foil subjected to the strain-anneal treatment.

perpendicular to the length of the domains. The main domains in the bulk of the specimen have their magnetizations perpendicular to the sheet surface, that is in the [100] direction, because internal stresses make this easy axis one of lower energy (Chikazumi and Suzuki, 1955; Carey, 1962; Corner and Mason, 1963).

Figure 6.6 presents a number of domain patterns obtained with the dry colloid technique on the strain-annealed foil. In figure 6.6(a) and (b), obtained from the same large grain, parallel, widely though unevenly spaced 180° domain walls are observed indicating that the specimen surface contains a simple crystallographic plane. Not all the walls are perfectly straight, the deviations indicating the presence of either inclusions or residual stress.

Figure 6.6(c) shows the domain pattern at the edge of the sample with parallel domain walls separated by about 20 microns. Several closure structures are observed. More parallel domain walls are displayed in figure 6.6(d). Although the walls are heavily decorated it can be seen that continuation of the walls through the portion of grain boundary running down the centre of the picture occurs. A misorientation of about 20° exists between the [001] directions in the two grains.

The final picture (figure 6.6(e)) shows a remarkable pattern. The main parallel 180° domain walls are separated by about 50 microns, but on this pattern is superimposed a fine, regular, wavy structure recurring approximately every 7 microns. This structure may be due to a small, periodic perturbation of the magnetization in the main domains caused

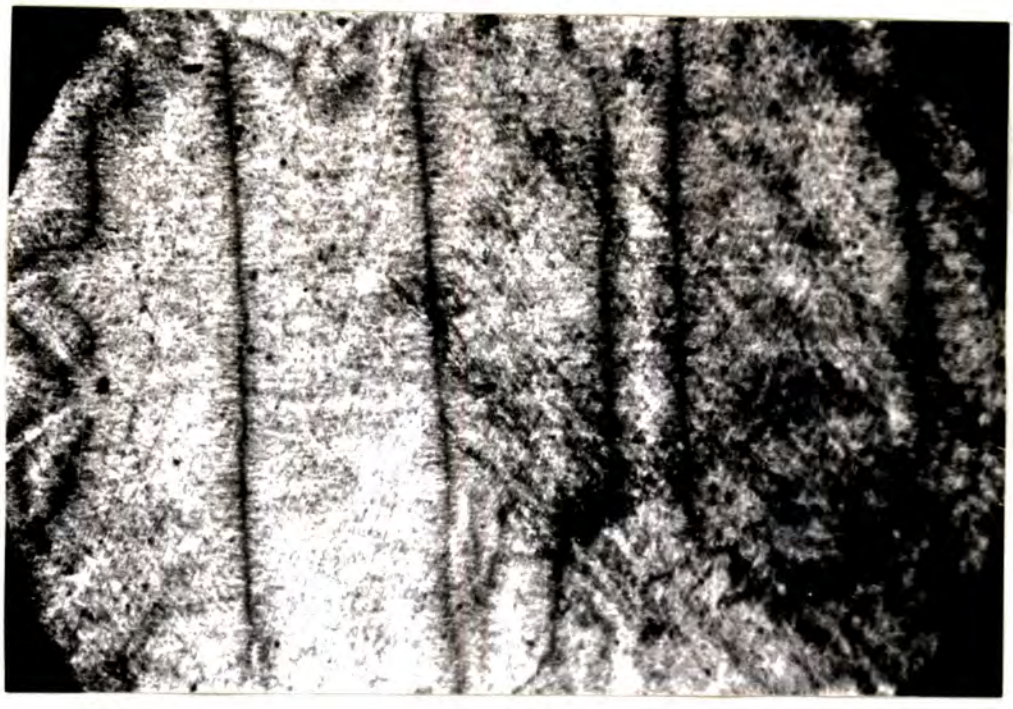

a)

100 μm

b)

200 μm

Figure 6.6 Domain patterns obtained using the dry colloid technique on the surface of foil subjected to the strain-anneal treatment.

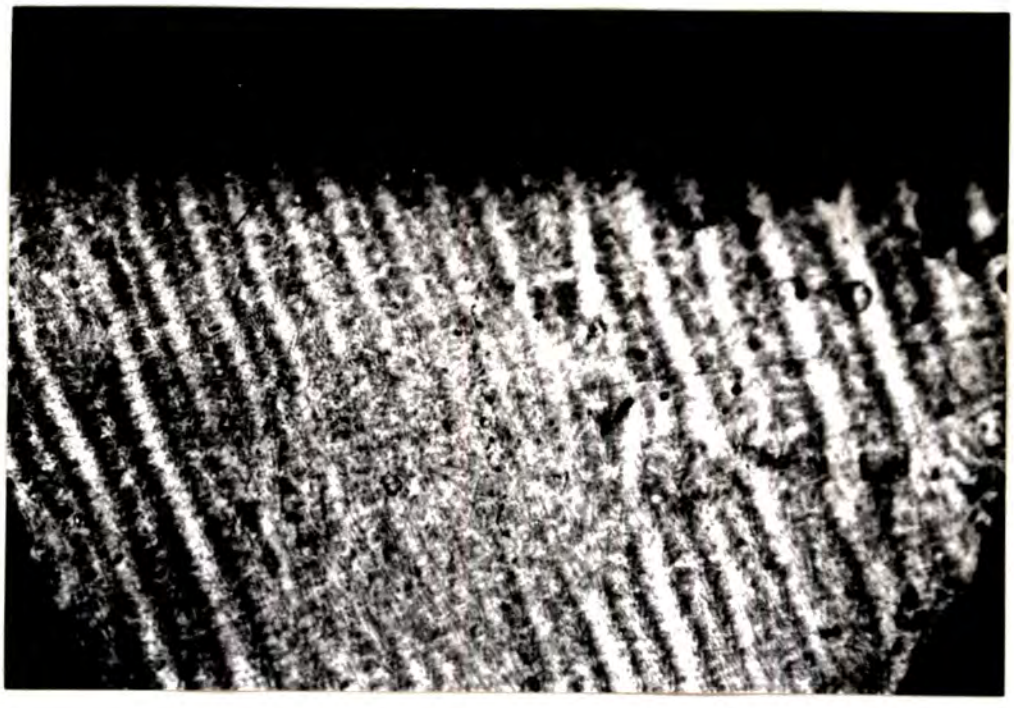

c)

100 µm

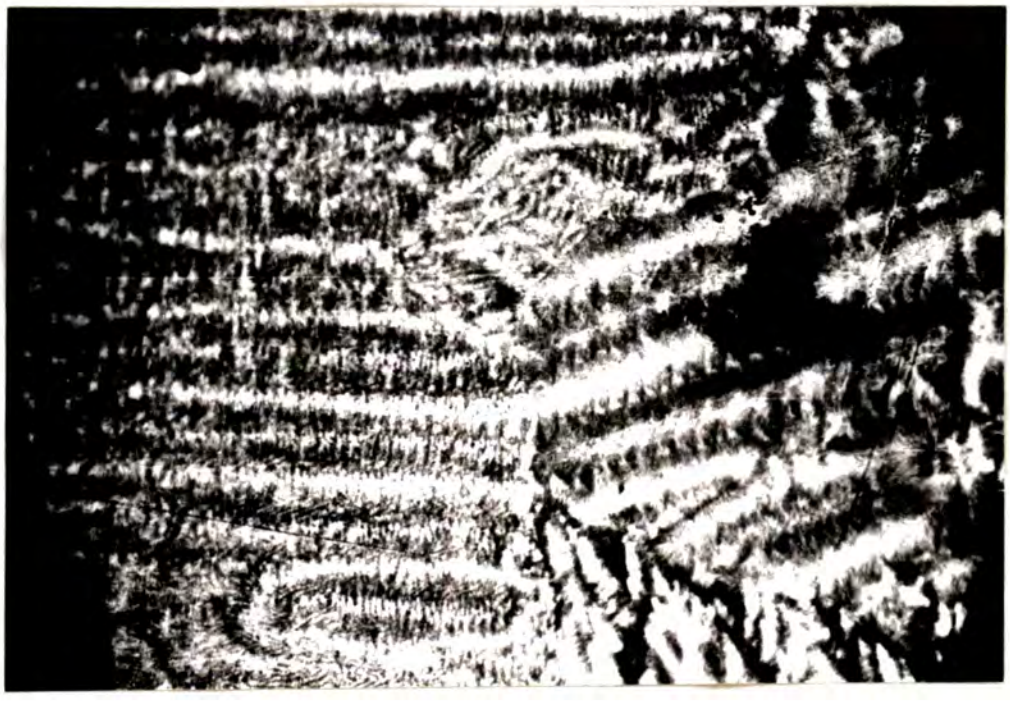

d)

e)

100 µm

by some strain effect.

As with the domain patterns obtained from the foil annealed for 2 hours at 1000°C the few interpretable patterns are vastly outnumbered by grains on which no sensible structures are observed. In only one instance was domain wall continuity through a grain boundary observed. It is concluded that the strain-anneal treatment does not produce a grain oriented structure, supporting the synchrotron radiation evidence presented in Chapter 5.

6.5 Magnetic Shielding

6.5.1 Introduction

In many electrical applications it is desirable to shield certain circuit components from stray magnetic fields of either a static or alternating nature. These fields include the earth's magnetic field and local fields arising from permanent magnets or current carrying coils, and can have an adverse effect on the performance of electrical equipment such as photomultipliers and cathode ray tubes. By completely enclosing the component in a shield of a ferromagnetic material of high permeability the field inside the shield can be dramatically reduced because of the high conductance of the shield material to magnetic flux.

Commercial magnetic shields come in either a preformed shape to fit closely round the relevant component or as a foil which can be cut to shape and wrapped around the device. Nickel-iron alloys, in particular mumetal, are commonly employed as magnetic shields but any high permeability soft magnetic metal or alloy could be used, and in this

light the possibility of using electrodeposited iron foil as a magnetic shield has been investigated. The discussion is limited to cylindrical shields.

6.5.2 Theory

The theory of the screening effect of a cylindrical magnetic shield is covered by Page and Adams (1931). In order to justify the use of simplified expressions later in the section, the calculation of the shielding factor is reproduced here and the magnetic induction inside the shield material is also derived.

We consider an infinitely long cylindrical shell of permeability μ, inner radius a and outer radius b, with its axis lying along the z-axis, placed in a uniform magnetic field H_0 parallel to the x-axis. This situation is illustrated in figure 6.7. Because of the inverse square law of attraction and repulsion for magnetic poles the magnetic potential V in a region containing no magnetic poles must satisfy Laplace's equation:

$$\frac{\partial^2 V}{\partial x^2} + \frac{\partial^2 V}{\partial y^2} + \frac{\partial^2 V}{\partial z^2} = 0 \qquad (6.2)$$

We require 3 solutions to this equation: V_1 to represent the potential outside the shell, V_2 to represent the potential in the shell material and V_3 to represent the potential in the cavity. The potential is a function of r and θ only. The boundary conditions are as follows:

1 For r very large V_1 must become $-H_0 x = -H_0 r \cos\theta$ provided the potential is taken as zero on the cylinder axis.

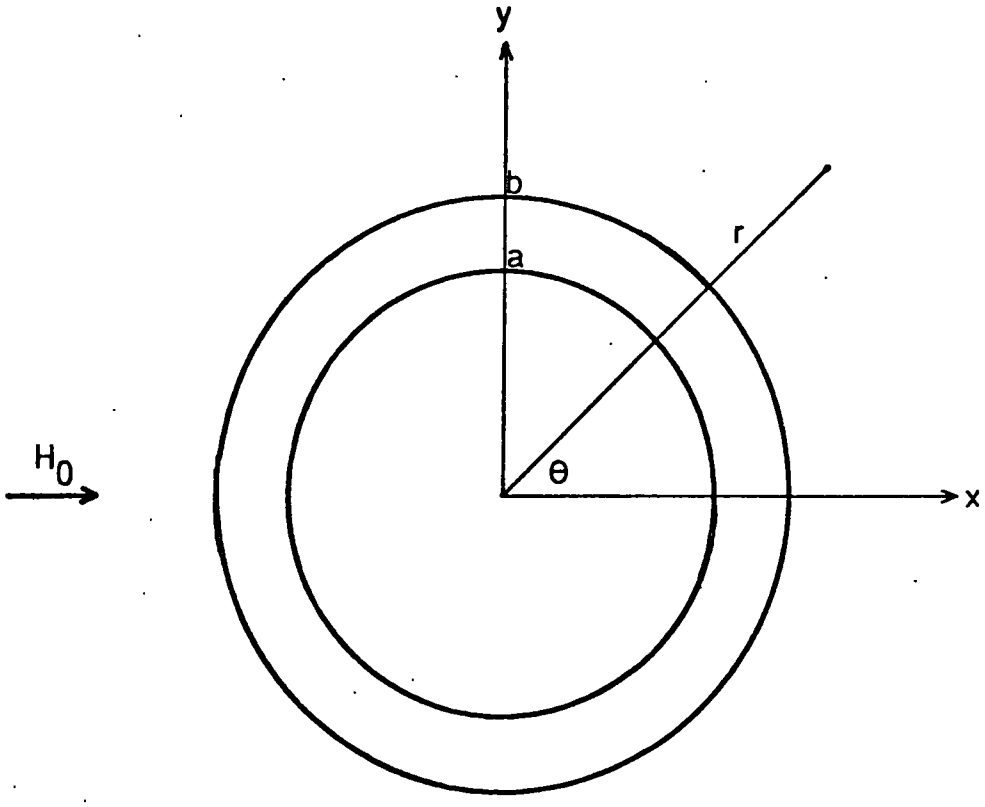

Figure 6.7 Magnetic shield coordinate system.

2 At each surface of the shell the radial component of the magnetic induction and the transverse component of the magnetic intensity must be continuous as we pass from the outside to the inside of the shell.

The latter of these two conditions is satisfied if the potential itself is continuous.

As the potential at infinity must be $-H_0 r \cos\theta$ it is clear that we are limited to harmonics involving only the first power of $\cos\theta$. It follows that the three potentials must be of the form

$$V_1 = -H_0 r \cos\theta + D_1 \frac{\cos\theta}{r} \qquad (6.3)$$

$$V_2 = C_2 r \cos\theta + D_2 \frac{\cos\theta}{r} \qquad (6.4)$$

$$V_3 = C_3 r \cos\theta \qquad (6.5)$$

where the term in r^{-1} has been omitted from V_3 since it would make the potential infinite at the origin.

In order to solve for the constants D_1, C_2, D_2 and C_3 we must introduce the boundary conditions as follows:

$V_1 = V_2$ for $r = b$;

$$-H_0 b^2 + D_1 = C_2 b^2 + D_2 \qquad (6.6)$$

$V_2 = V_3$ for $r = a$;

$$C_2 a^2 + D_2 = C_3 a^2 \qquad (6.7)$$

Continuity of radial component of induction at r = b;

$$H_o b^2 + D_1 = \mu(-C_2 b^2 + D_2) \tag{6.8}$$

Continuity of radial component of induction at r = a;

$$\mu(-C_2 a^2 + D_2) = -C_3 a^2 \tag{6.9}$$

Solving for C_2, D_2 and C_3 we have

$$C_2 = \frac{2H_o b^2 (\mu + 1)}{a^2 (\mu - 1)^2 - b^2 (\mu + 1)^2} \tag{6.10}$$

$$D_2 = \frac{2H_o a^2 b^2 (\mu - 1)}{a^2 (\mu - 1)^2 - b^2 (\mu + 1)^2} \tag{6.11}$$

$$C_3 = \frac{4H_o b^2 \mu}{a^2 (\mu - 1)^2 - b^2 (\mu + 1)^2} \tag{6.12}$$

In practical cases the permeability μ of the shield material is much greater than unity and the inner and outer shell radii are nearly equal so that we can write (b - a) = t, the material thickness, and $a \simeq b$. The constants above can now be approximated by

$$C_2 = -\frac{H_o b}{\mu t} \tag{6.13}$$

$$D_2 = -\frac{H_o b^3}{\mu t} \tag{6.14}$$

$$C_3 = -\frac{2H_o b}{\mu t} \tag{6.15}$$

The field in the x-direction inside the cavity is given by

$$H_3 = -\frac{\partial V_3}{\partial x} = -\frac{\partial}{\partial x}\left[C_3 r \cos\theta\right]$$

$$H_3 = \frac{2H_o b}{\mu t} \tag{6.16}$$

The shielding factor g, defined as the ratio of the external field to the field in the shield cavity, is therefore given by

$$g = \frac{H_o}{H_3} = \frac{\mu t}{d} \qquad (6.17)$$

where d is the shield diameter.

The calculation of the field H_2 inside the shield material is simplified by representing the appropriate potential in Cartesian coordinates:

$$V_2 = C_2 x + D_2 \frac{x}{x^2 + y^2} \qquad (6.18)$$

Components of the magnetic field in both the x and y directions must be considered by obtaining the appropriate partial derivatives of V_2. Representing the component of field in the x-direction by H_{2x} and that in the y-direction by H_{2y} we obtain:

$$H_{2x} = -\frac{\partial V_2}{\partial x} = - C_2 - D_2 \frac{(y^2 - x^2)}{(x^2 + y^2)^2} \qquad (6.19)$$

$$H_{2y} = -\frac{\partial V_2}{\partial y} = D_2 \frac{2xy}{(x^2 + y^2)^2} \qquad (6.20)$$

Since we are considering shields for which the inner and outer radii are nearly equal, at any point in the shield material we can write $x^2 + y^2 = b^2$. We can also introduce the values of C_2 and D_2 from equations 6.13 and 6.14 and multiply the field components by the permeability μ to yield x and y components of the magnetic induction B in the shield material. These are given by:

$$B_{2x} = \frac{H_o b}{t} + \frac{H_o b}{t} \frac{(y^2 - x^2)}{b^2} \qquad (6.21)$$

$$B_{2y} = - \frac{2H_o b}{t} \frac{xy}{b^2} \qquad (6.22)$$

The maximum induction in the shield material occurs at the point at which $x = 0$ and $y = b$. At this point we have

$$B_{2x} = \frac{2H_o b}{t}$$

$$B_{2y} = 0$$

The induction is a minimum on the x-axis where $x = b$ and $y = 0$. Here

$$B_{2x} = B_{2y} = 0$$

Since it is important not to saturate the shield at any point, the maximum induction is the most important value and can be written as:

$$B = H_o \frac{d}{t} \qquad (6.23)$$

Equations 6.17 and 6.23 are the fundamental relationships defining the performance of a given magnetic shield. It should be noted that the material permeability is not a constant but varies with induction as discussed in Chapter 1.

For A.C. fields the shielding factor is increased by the reflection and absorption of electromagnetic waves at the shield, but only D.C. tests have been performed on the iron foil.

6.5.3 Experimental Procedure and Results

In investigating the shielding capability of the electrodeposited iron foil, cylindrical shields of identical dimensions to an available mumetal shield manufactured by Magnetic Shields Limited were fabricated. Rectangles of iron foil 10 x 11.5 cm^2 were rolled to form cylinders 10 cm long and 3.1 cm in diameter. The overlapping edge was stuck down with tape to form a closed flux path. Comparisons with the mumetal shield were then possible.

The external magnetic field was provided by a pair of Helmholtz coils which were supplied by a D.C. magnet power supply. Currents of up to 1 amp were used, these being measured on a 1000 mA D.C. ammeter. The Helmholtz coils were calibrated first with a Hall probe which gave a calibration factor of 81.9 Oe A^{-1}. The sensitivity of the Hall probe was insuffieient to measure the small fields inside the magnetic shields, so these measurements were made using a 5000 turn search coil linked to an integrating fluxmeter. In the absence of any shields the search coil gave a calibration factor of 5.77 mWb turns A^{-1} for the Helmholtz coils. By relating this figure to the Hall probe calibration factor, all the field measurements could readily be converted into oersteds.

Three shields were tested in the experiment; first the mumetal one followed by shields made from the sample 6 foil in the as-produced state and after a 2 hour anneal at 900°C. The latter shield was annealed in its final shape to avoid strain due to bending. The shields were firmly supported in turn between the Helmholtz coils with their axes perpendicular to the field. The 5000 turn search coil was used to measure the field H_3 existing inside the shield cavity as a function of the external field H_o which had previously been measured for the same current values in the absence of any shields. H_3 is plotted as a function of H_o for the three shields in figures 6.8, 6.9 and 6.10. A hysteresis effect was noted as the external field was reduced from its maximum value and a small field remained inside the shield cavity when the external field was reduced to zero. This field was always antiparallel to the external field and was due to the demagnetizing effect in the shield material which gave rise to free magnetic poles at the opposite sides of the shields during the magnetization process.

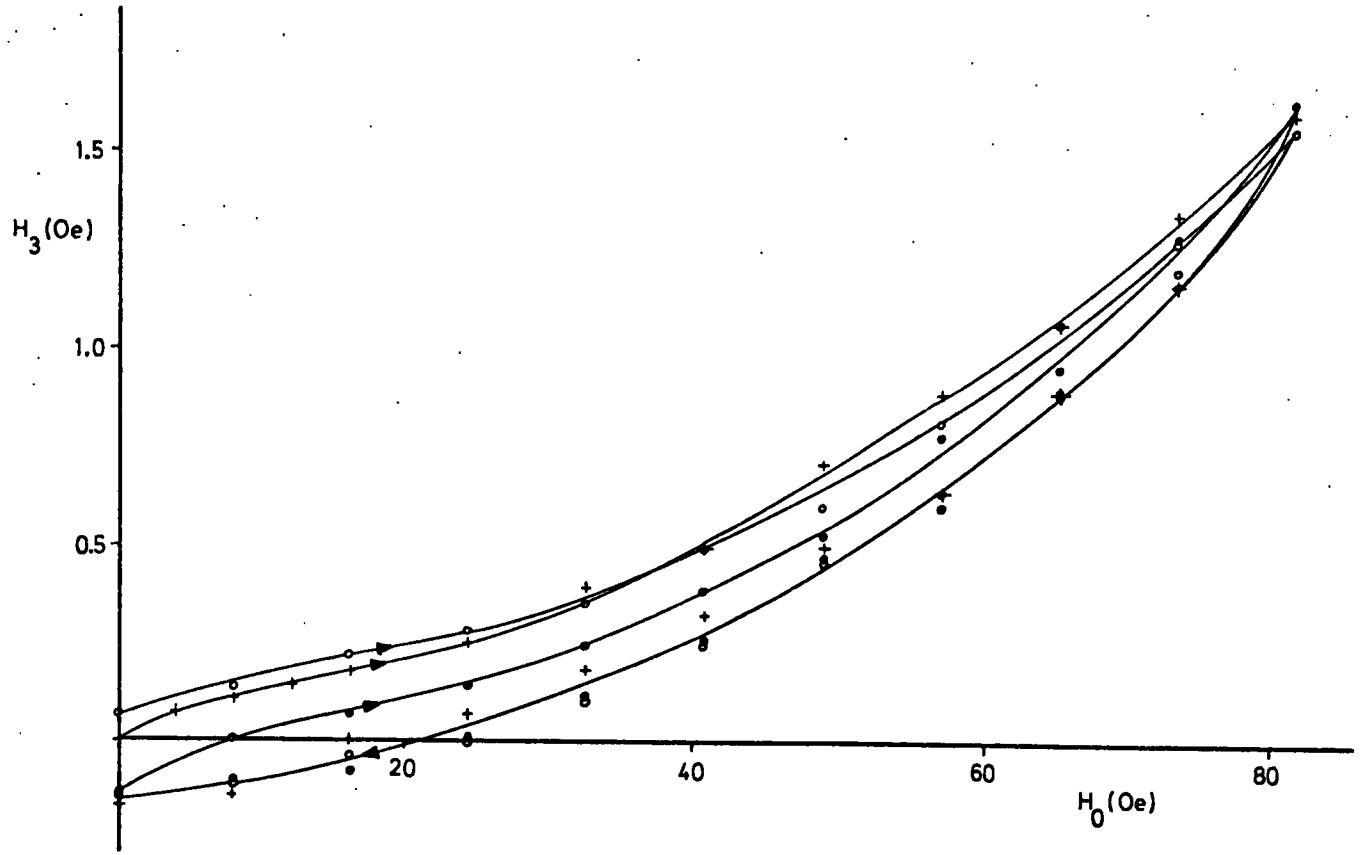

Figure 6.8 Experimental relationships between internal and external fields for mumetal magnetic shield.

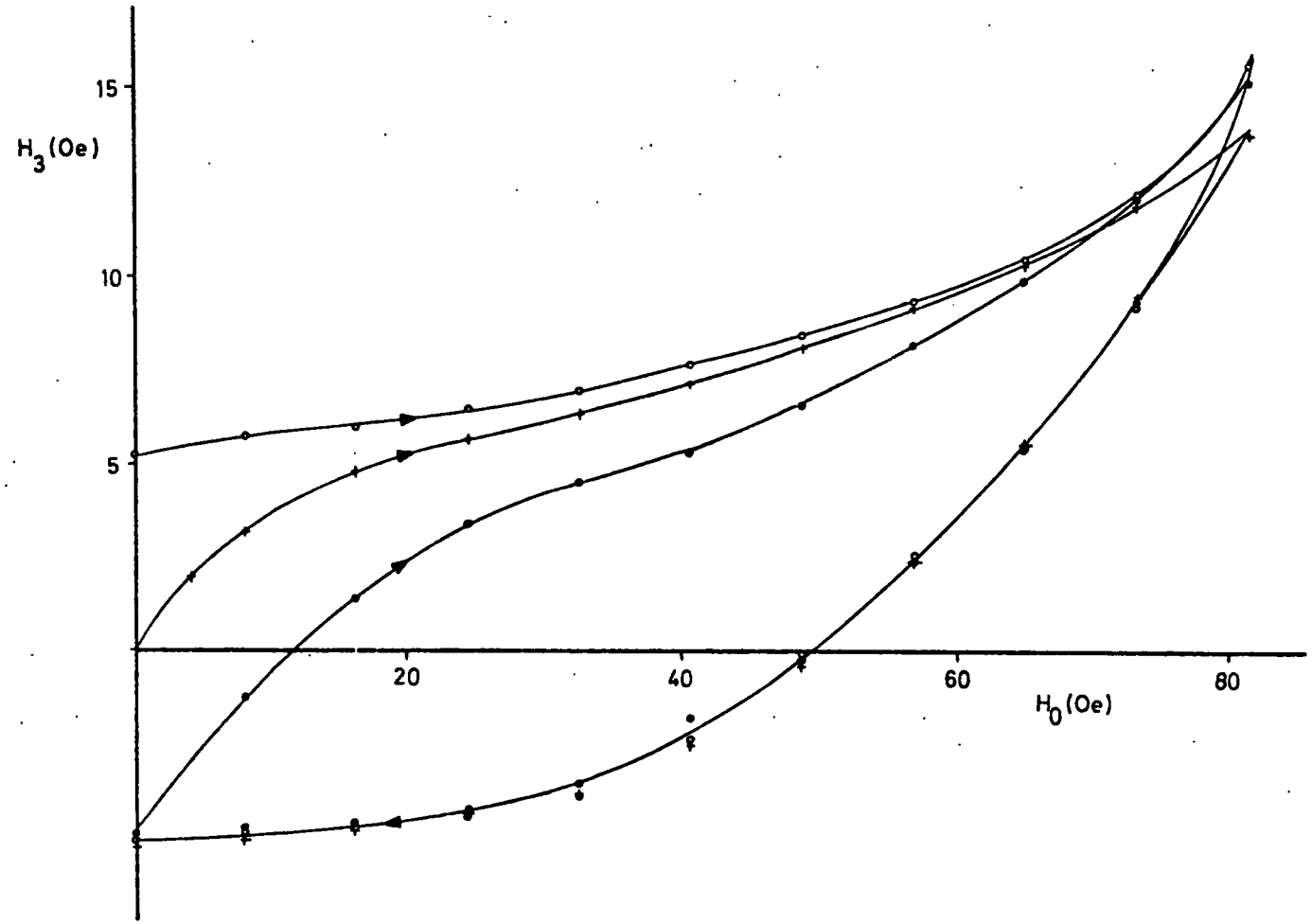

Figure 6.9 Experimental relationships between internal and external fields for as-produced iron magnetic shield.

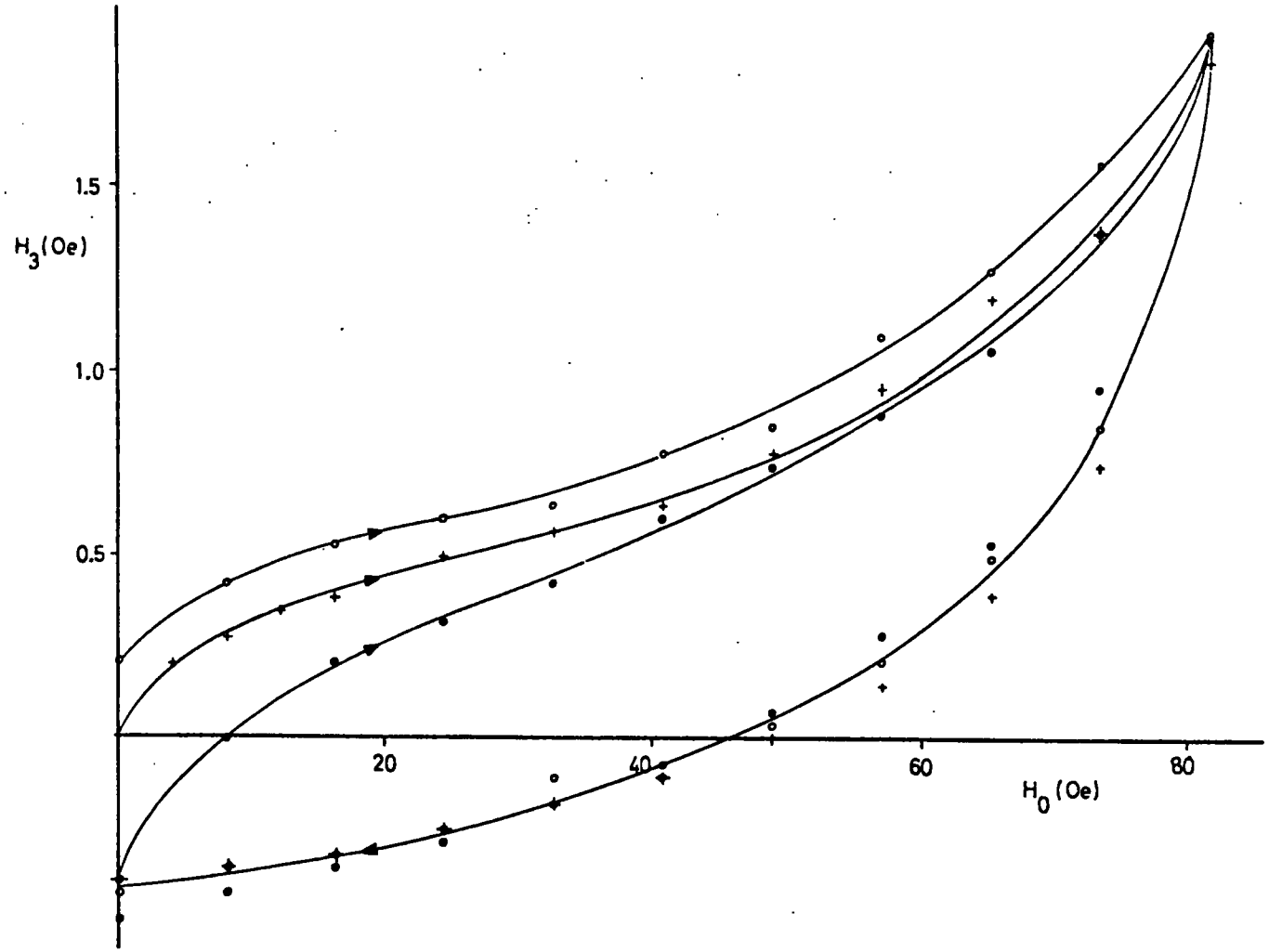

Figure 6.10 Experimental relationships between internal and external fields for annealed iron magnetic shield.

When the external field was reduced, these free poles gave rise to the reverse field in the shield cavity. Each of figures 6.8, 6.9 and 6.10 displays three sets of data points corresponding to three initial states of the shield. These are, respectively, the demagnetized state and the states in which the remanent field in the shield cavity existing after a previous magnetization is aligned parallel or antiparallel to the external field.

These graphs do not give a true representation of the relative merits of the shields however because of the geometrical dependence of the shielding factor. The mumetal shield was composed of material 400 microns thick which exaggerates its shielding effect compared with the 155 micron thick iron shields. The only physical properties governing the shield performance are the material permeability μ and induction B. Equation 6.17 and 6.23 have been used to calculate the μ - B curves for the three shields tested and these are plotted in figure 6.11 on logarithmic axes. Also plotted for comparison are data for typical mumetal shielding material (Telcon Metals Limited, Publication No 17-369) and silicon-iron (Mond Nickel Company Limited, 1950). It can be seen that the annealed iron foil has a maximum permeability which is exceeded only by that of the Telcon mumetal. Furthermore, above an induction of about 7500 G the annealed iron has the highest permeability.

It is interesting to note that the maximum permeabilities for the as-produced and annealed iron foils measured by this method are greater than the values obtained by the extrapolation procedure involving minor hysteresis loops which was covered earlier. This is probably due to the different measuring techniques used, the present one being a static

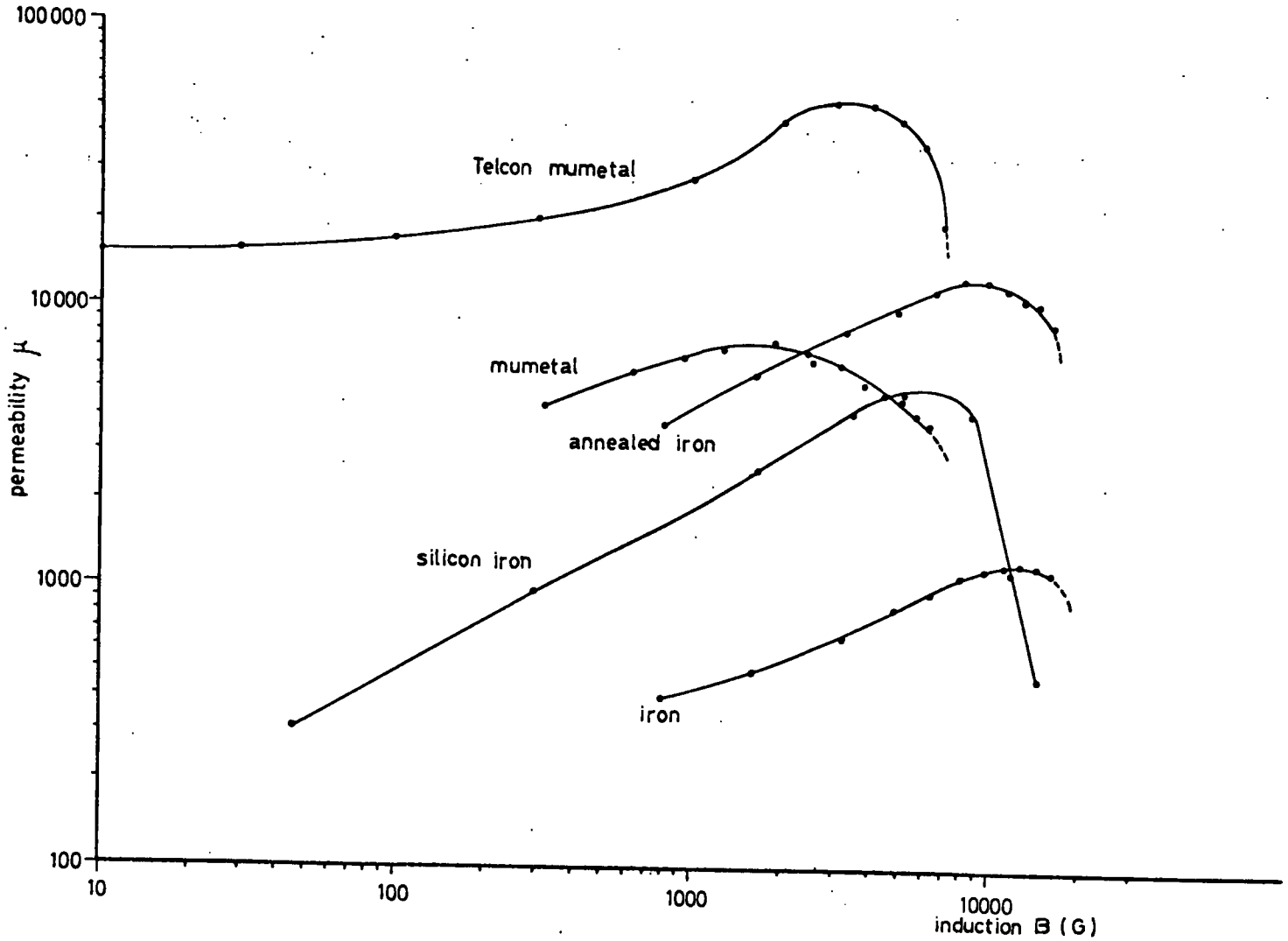

Figure 6.11 Permeability against induction curves for various magnetic shielding materials.

field method compared with the alternating field determination which yielded the lower values.

6.5.4 Design of Magnetic Shields

The performance of a magnetic shield is completely specified by the permeability against induction curve of the shield material and the ratio of the diameter of the shield to the thickness of the shielding material. In this section a few graphical guidelines to the design of shields constructed from typical silicon iron, mumetal (Telcon Metals Limited) and annealed electrodeposited iron foil will be presented.

In designing a shield it is necessary to know the value of the field to be shielded and the maximum field that can be tolerated inside the shield cavity. Inspection of equation 6.17 indicates that the shielding factor increases with increasing t/d. However, in the interests of economy and weight it is desirable to minimize the thickness of the shield, so it is important to fit the shield closely round the component in order to minimize d and hence maintain the shielding factor.

Using the data in the μ - B curves (figure 6.11) the field H_3 inside the shield cavity has been calculated as a function of external field H_o for d/t ratios of 10, 30, 100, 300 and 1000 for shields constructed of mumetal, silicon-iron and annealed iron foil. The data appears in figures 6.12, 6.13 and 6.14 respectively. From the graphs it is possible to estimate the ratio of d/t necessary to give a particular value of H_3 for any given value of H_o. The shielding material which achieves the desired shielding ratio for the minimum material thickness can then be chosen. For low external fields mumetal is vastly superior

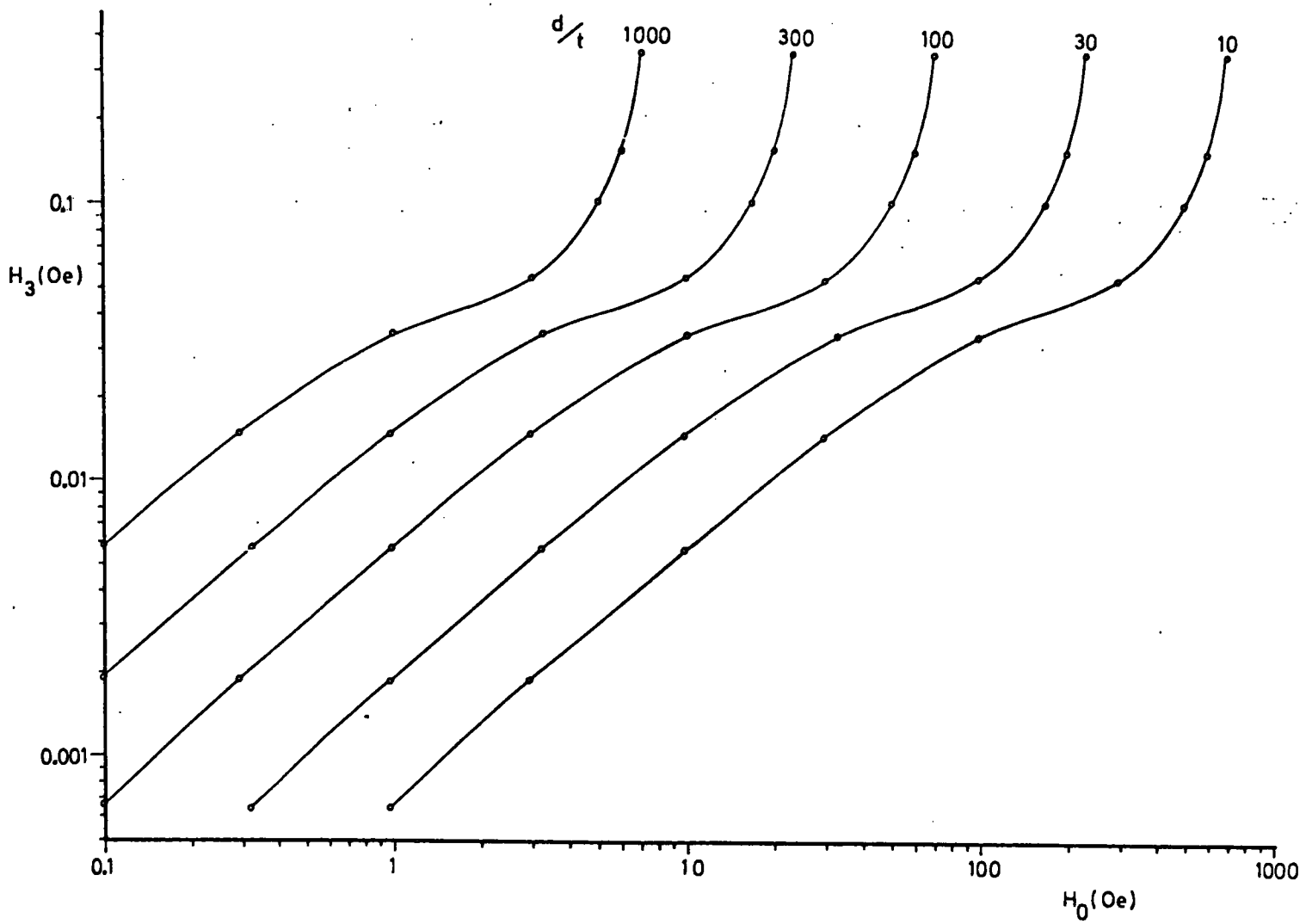

Figure 6.12 Calculated relationships between internal and external fields for Telcon mumetal magnetic shields of various dimensions.

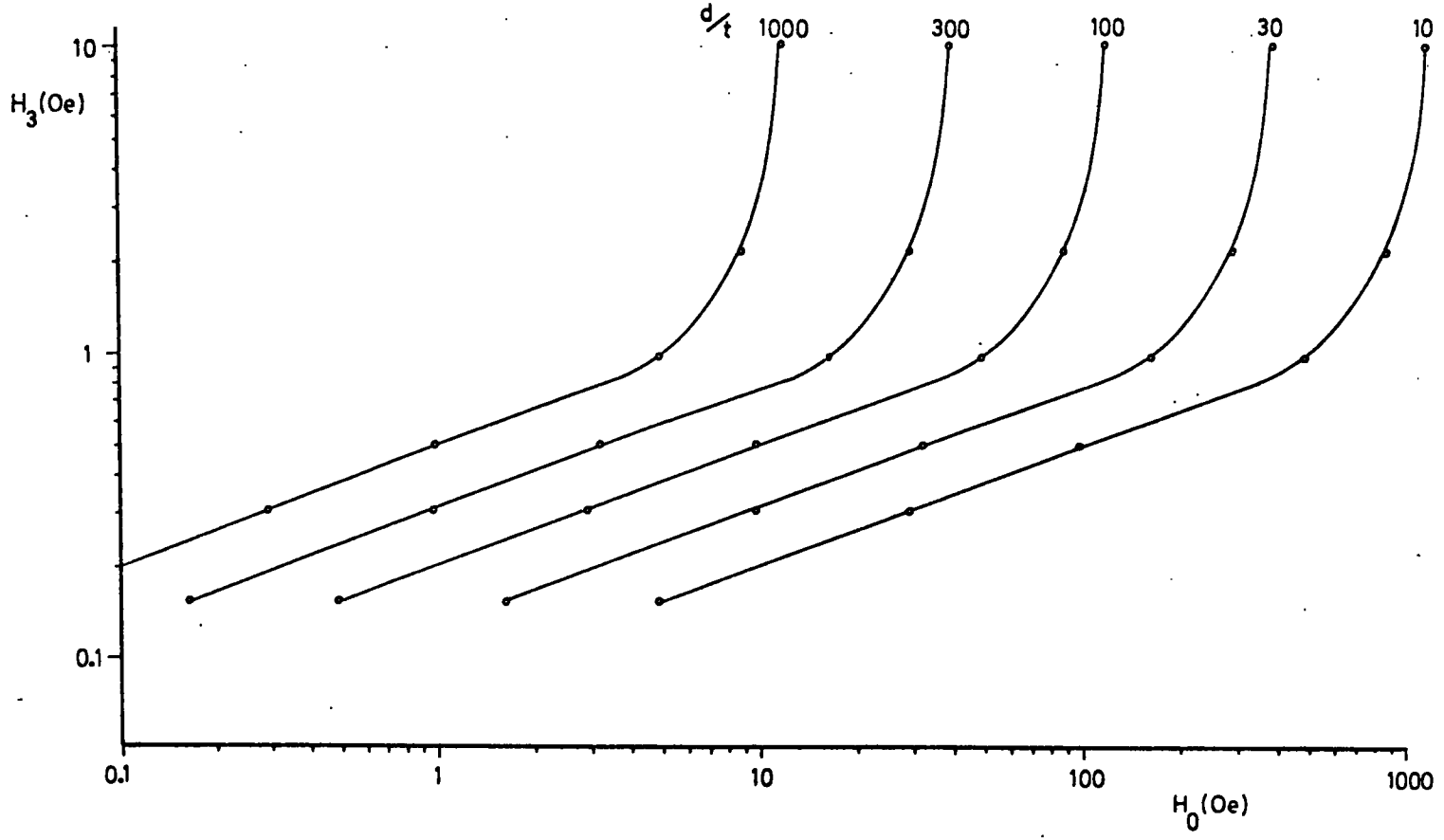

Figure 6.13 Calculated relationships between internal and external fields for silicon-iron magnetic shields of various dimensions.

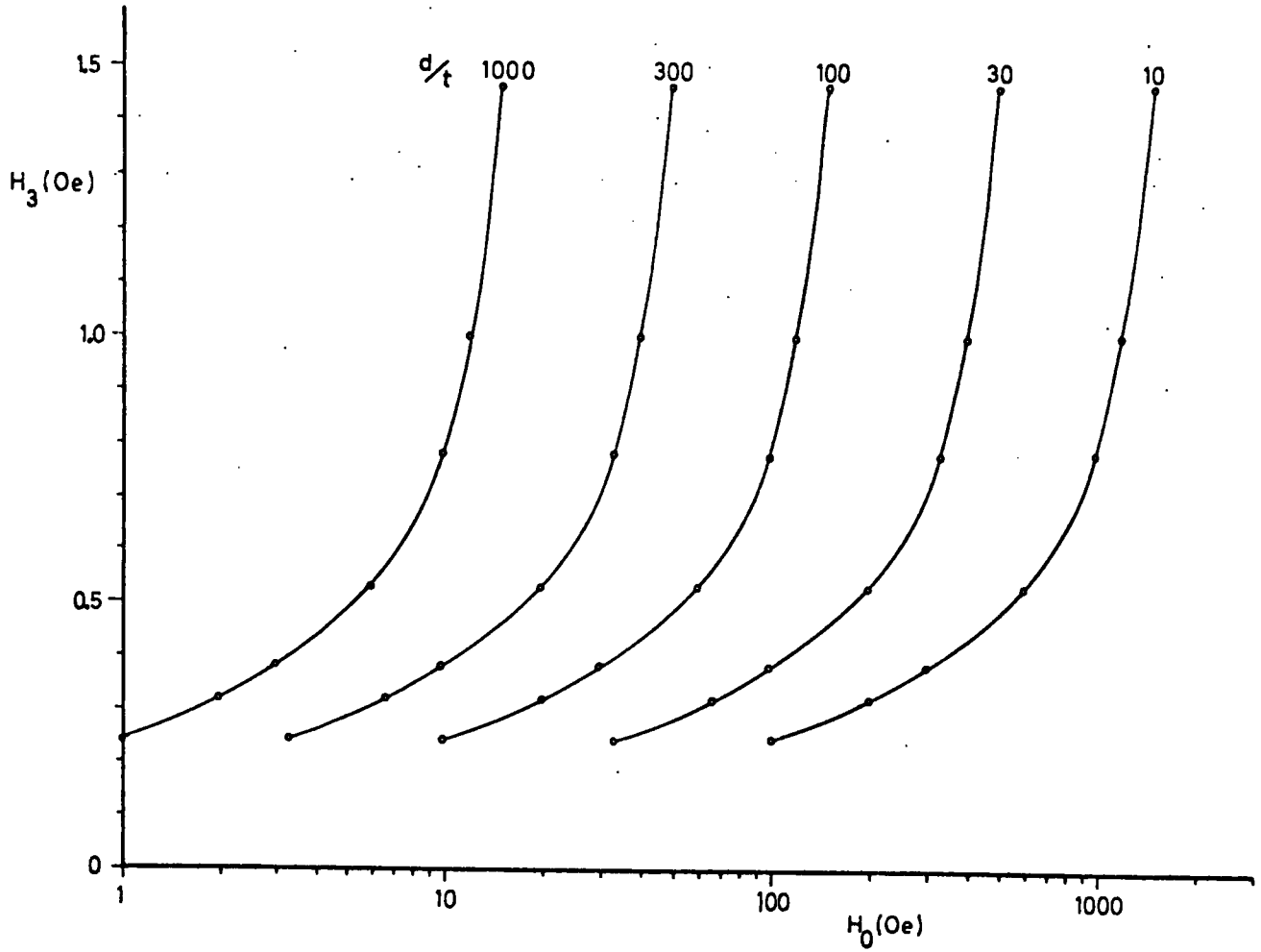

Figure 6.14 Calculated relationships between internal and external fields for annealed iron magnetic shields of various dimensions.

to the iron and silicon iron but as the external field rises the annealed iron becomes competitive with the mumetal. The situation is formalized in figure 6.15 which plots the value of d/t against external field corresponding to the best performance of the mumetal and annealed iron. The best performance is defined here as the situation in which the shield material is operating at its maximum permeability since, from equation 6.17, for a given value of d/t the maximum shielding ratio is achieved when the permeability is a maximum. The third line on the graph corresponds to the induction above which the permeability of the annealed iron exceeds that of the mumetal. Figure 6.15 can be used in two ways: firstly for a given value of d/t the value of external field above which the annealed iron gives a better shielding ratio than the mumetal can be obtained along with the values of external field for which the two materials are giving the best possible shielding ratio; secondly for a given value of external field the values of d/t corresponding to the best performance of the two shielding materials can be read off.

6.5.5 Conclusions

The possibility of using electrodeposited iron foil as a magnetic shielding material has been investigated by comparing its performance experimentally with a commercial mumetal shield and also with technical data for mumetal and silicon-iron. In the as-produced form the foil is of little interest but after a 2 hour anneal at 900°C exhibits shielding properties which could be usefully employed in cases where the external field is fairly large. The mechanical softness of the annealed foil could prove to be a problem in its application since plastic strain due to bending would be expected to have a detrimental

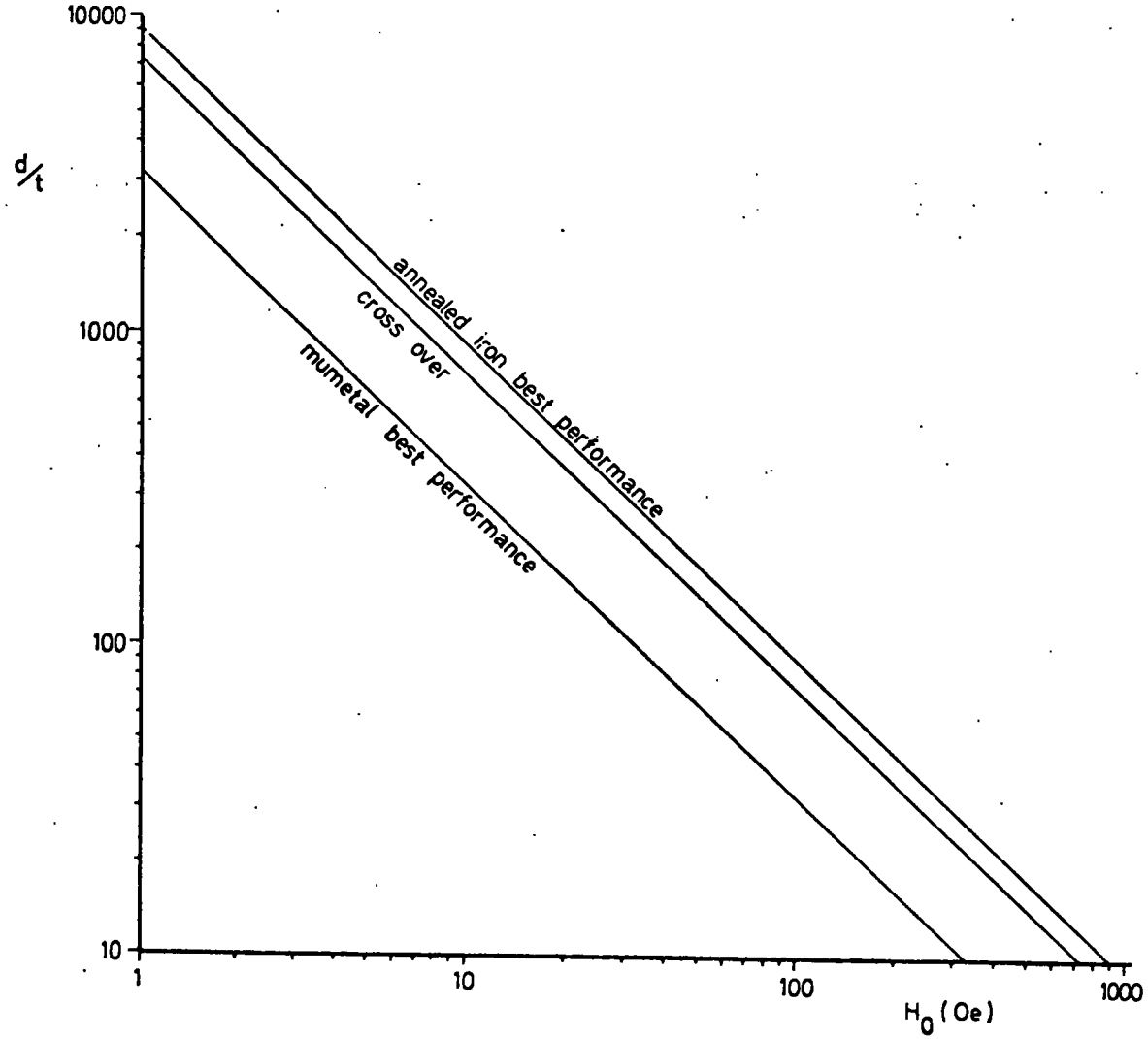

Figure 6.15 Relative merits of annealed iron and Telcon mumetal magnetic shields in terms of shield dimensions against external field.

effect on the magnetic properties. However the foil in its thicker form may have some future in cases where it can be annealed in its final shape, and the thinner foil could be applied as a wrap-around shield where high shielding ratios are not required. In addition the relative simplicity of the production and heat treatment of the foil may prove to be economically advantageous.

CHAPTER SEVEN

CONCLUSIONS

Various physical and magnetic properties of iron foil produced by a process of electrodeposition have been investigated and compared with typical properties of commercial soft magnetic materials. The values obtained show no systematic dependence on foil thickness or the direction of testing. In the as-produced state, the foil compares very poorly with any commercial alternative. An improvement in the soft magnetic characteristics can be brought about by various annealing treatments which have the effect of increasing the average grain diameter by gradual grain growth. It should be possible to incorporate a suitable annealing furnace directly onto the foil production line provided that the foil can be constrained within an inert gas atmosphere whilst at high temperature to prevent oxidation which is a serious problem for such a thin material.

A strain-anneal technique for producing a large grain structure in the foil by secondary recrystallization has been developed, but it is unlikely that this could be readily applied as an on-line process. In any event the magnetic properties resulting from this treatment are no better than those effected by the straightforward annealing treatment.

The improved magnetic properties of even the heat treated foil are still very poor compared with the coercive force of 0.05 Oe and maximum permeability of 180,000 for purified (99.95%) iron quoted in table 1.1.

The only area in which the foil has shown any possible commercial applicability is that of magnetic shielding, and had time permitted it would have been interesting to form, anneal and test iron shields to fit around specific components, such as cathode ray tubes.

In order to further improve the magnetic characteristics of the foil, it would be desirable to induce a degree of preferred orientation into the grain structure. It is envisaged that this could be achieved by a secondary recrystallization process involving inhibition of normal grain growth by dispersed impurity particles such as manganese sulphide. Unfortunately the incidental levels of manganese and sulphur present in the as-produced foil are at least an order of magnitude lower than those deliberately introduced into commercial silicon-iron for this purpose. By adjusting the amounts of these two elements present in the electrolyte it should be possible to deposit iron foil containing suitable impurity levels. However the closedown of the Hall and Pickles foil production unit in October 1977 rendered such experiments impossible. Additional sulphur inhibitors could also be introduced directly into the grain boundaries by diffusion during the recrystallization process in a manner similar to that used by Kohler (1967).

As the static and low frequency measurements did not indicate that the as-produced or heat treated foil had characteristics comparable with other soft magnetic materials it was not felt important that A.C. measurements should be carried out at higher frequencies. If, however, more satisfactory material could be produced as suggested above then such measurements would become of greater importance. The results could be analysed to determine the relative contributions of the various

mechanisms controlling magnetization processes and producing losses.

Whilst high purity iron produced by electrodeposition appears uninteresting compared with commercially available soft magnetic materials, it may be that useful alloy foils could be produced by this process. There would appear to be considerable advantages in this method since the energy requirements for thin foil production are low compared with those of conventional rolling techniques and the alloy composition may be accurately controlled by monitoring the electrolyte composition. It would have been very interesting to prepare foils of mumetal by this technique and to study their properties, but this was precluded by the closure of the foil production unit.

A particularly interesting aspect of the work associated with the project was that involving synchrotron radiation. It has been shown that synchrotron radiation is very useful as a rapid means of assessing the grain size, orientation and perfection of polycrystalline metal sheets. In addition the first in-situ studies of crystal growth under normal growth conditions have been performed on polycrystalline silicon-iron sheet. The apparatus used in this innovatory experiment was unfortunately rather unsophisticated and no reproducible quantitative data were extracted. However the feasibility of the technique has been amply demonstrated and it is envisaged that the remaining experimental deficiencies could readily be overcome. It was particularly regrettable that the closedown of the Synchrotron Radiation Facility at Daresbury Laboratory in April 1977 and the unavailability of beam time at suitable overseas sources, such as DESY at Hamburg, prevented further research on this project.

REFERENCES

Adam J. 1960 "x-Ray Diffraction by Polycrystalline Materials" Chapman and Hall

Anderson W.A., Mehl R.F. 1945 Trans. A.I.M.E. 161, 140

Antonione C., Della Gatta G., Riontino G., Venturello G. 1973 J. Mat. Sci. 8, 1

Antonione C., Marino F., Riontino G., Tabasso M.C. 1977 J. Mat. Sci. 12, 747

Bailey J.E. 1960 Phil. Mag. 5, 833

Bailey J.E., Hirsch P.B. 1962 Proc. Roy. Soc. A 267, 11

Barratt C.S. 1945 Trans. A.I.M.E. 161, 15

Bates K.L. 1965 M.Sc. Thesis Constantine College of Technology, Middlesbrough

Baudelet B., Champier G. 1973 Crystal Lattice Defects 4, 95

Beck P.A. 1954 Adv. Phys. 3, 245

Beck P.A., Kremer J.C., Demer L.J., Holzworth M.L. 1948 Trans. A.I.M.E. 175, 372

Beck P.A., Sperry P.R. 1950 J. Appl. Phys. 21, 150

Berg W.F. 1931 Naturwissenschaften 19, 391

Bitter F. 1931 Phys. Rev. 38, 1903

Bitter F. 1932 Phys. Rev. 41, 507

Bolling G.F., Winegard W.C. 1958 Acta Met. 6, 283

Booker G.R. 1969 "Moddern Diffraction and Imaging Techniques in Materials Science" North-Holland

Bordas J., Glazer A.M., Hauser H. 1975 Phil. Mag. 32, 471

Bowen D.K., Hall C.R. 1975 "Microscopy of Materials" Macmillan

Burke J.E. 1949 Trans. A.I.M.E. 180, 73

Cahn R.W. 1949 J. Inst. Met. 76, 237

Cahn R.W. 1950 Proc. Phys. Soc. A 63, 323

Carey R. 1962 Proc. Phys. Soc. 80, 516

Carey R., Isaac E.D. 1966 "Magnetic Domains and Techniques for their Observation" English Universities Press

Chikazumi S., Suzuki K. 1955 J. Phys. Soc. Japan 10, 523

Christian J.W. 1965 "The Theory of Transformations in Metals and Alloys" Pergamon

Corner W.D., Mason J.J. 1963 Proc. Phys. Soc. 81, 925

Cottrell A.H. 1953 "Dislocations and Plastic Flow in Crystals" Clarendon

Decker B.F., Harker D. 1950 Trans. A.I.M.E. 188, 887

Dunn C.G., Walter J.L. 1960 Trans. A.I.M.E. 221, 413

Feltham P. 1957 Acta Met. 5, 97

Gastaldi J., Jourdan C., Marzo P., Michel R. in Miltat J. 1978 Nuclear Instruments and Methods 152, 323

Goss N.P. 1934 U.S. Patent 1 965 559

Graham C.D. Jr. 1969 "Magnetism and Metallurgy" Van Nostrand

Guinier A., Tennevin J. 1949 Acta Cryst. 2, 133

Hargreaves A. 1960 "X-Ray Diffraction by Polycrystalline Materials" Chapman and Hall

Harker D., Parker E.R. 1945 Trans. A.S.M. 34, 156

Hart M. 1975 J. Appl. Cryst. 8, 436

Hirsch P.B., Horne R.W., Whelan M.J. 1957 "Dislocations and Mechanical Properties of Crystals" Wiley

Hull D. 1975 "Introduction to Dislocations" Pergamon

Kellar J.N., Hirsch P.B., Thorp J.S. 1950 Nature, Lond. 156, 554

Kohler D.M. 1967 J. Appl. Phys. 38, 1176

Koves G., Pesch J. 1963 I.B.M. J. Research and Development 7, 160

Lang A.R. 1958 J. Appl. Phys. 29, 597

Lang A.R. 1959 Acta Cryst. 12, 249

Lea K.R. 1978 Phys. Reports 43, 337

Lee E.W., Lynch A.C. 1959 Adv. Phys. 8, 292

Littmann M.F. 1971 I.E.E.E. Trans. Magn. 7, 48

MacCormack I.B., Tanner B.K. 1978 J. Appl. Cryst. 11, 40

Martin J.W. 1969 "Elementary Science of Metals" Wykeham

May J.E., Turnbull D. 1957 Trans. A.I.M.E. 212, 769

Mond Nickel Company Limited 1950 "The Magnetic Properties of Nickel-Iron Alloys"

Morrish A.H. 1965 "The Physical Principles of Magnetism" Wiley

Mundell P.A. 1976 Ph.D. Thesis University of Durham

Nøst B., Sørensen G. 1966 Phil. Mag. 13, 1075

Oguey H.J. 1969 "Magnetism and Metallurgy" Academic Press

Page L., Adams N.I. 1931 "Principles of Electricity" Van Nostrand

Pugh E.M., Pugh E.W. 1960 "Principles of Electricity and Magnetism" Addison-Wesley

Safa M., Tanner B.K. 1977 Physica 86-88 B, 1347

Safa M., Tanner B.K. 1978 Phil. Mag. B 37, 739

Schulz L.G. 1954 Trans. A.I.M.E. 200, 1082

Seymour W.E., Harker D. 1950 Trans. A.I.M.E. 188, 1001

Smith C.S. 1948 Trans. A.I.M.E. 175, 15

Smith R.L. 1978 Ph.D. Thesis University of Durham

Spychal P. 1977 Private Communication

Stanley J.K., Mehl R.F. 1942 Trans. A.I.M.E. 150, 260

Steinberger I.T., Bordas J., Kalman Z.H. 1977 Phil. Mag. 35, 1257

Taguchi S., Sakakura A., Yasunari T. 1964 U.S. Patent 3 163 564

Tanner B.K. 1976 "x-Ray Diffraction Topography" Pergamon

Tanner B.K. 1977 Prog. Crystal Growth Charact 1, 23

Tanner B.K., Midgley D., Safa M. 1977a J. Appl. Cryst. 10, 281

Tanner B.K., Safa M., Midgley D. 1977b J. Appl. Cryst. 10, 91

Tanner B.K., Safa M., Midgley D., Bordas J. 1976 J Magnetism and Magnetic Materials 1, 337

Tardy P., Iskander S.S. 1969 J. Mat. Sci 4, 353

Telcon Metals Limited, Publication No. 17-369

Thornburg D.R., Foster K., Rauch G.C. 1976 A.I.P. Conf. Proc. (U.S.A.) 29, 554

Titchener A.L., Bever M.B. 1958 Prog. Met. Phys. 7, 247

Tomboulian D.H., Hartman P.L. 1956 Phys. Rev. 102, 1423

Weast R.C. 1975-6 "Handbook of Chemistry and Physics" C.R.C. Press

Weiss P. 1907 J. Phys. 6, 667

Williams H.J., Bozorth R.M., Shockley W. 1949 Phys. Rev. 75, 155

Yamamoto T., Ohya Y. 1974 I.E.E.E. Trans. Magn. 10, 157

Zener in Smith C.S. 1948 Inst. of Metals Lecture, A.I.M.E. Met. Tech.